Cross-shelf overturning in geostrophic-stress-dominant coastal fronts

(地衡流シアー応力が卓越する沿岸フロントにおける陸棚上の鉛直循環)

北海道大学大学院環境科学院

原 楠

(Nan Yuan)

Doctoral Dissertation

Cross-shelf overturning in geostrophic-stress-dominant coastal fronts

(地衡流シアー応力が卓越する沿岸フロントにおける陸棚上の鉛直循環)

YUAN Nan

Graduate School of Environmental Science,
Hokkaido University

December 2022

This dissertation is adapted from:

Yuan, N., & Mitsudera, H. (2022). Cross-shelf overturning in geostrophic-stress-dominant coastal fronts. Journal of Oceanography, 1-22.; DOI:10.1007/s10872-022-00661-6

Abstract

Dynamics of the predominant coastal along-isobath current inside the Sea of Okhotsk, with a magnitude of tens of centimeters per second, has been unveiled via observational measurements and numerical simulations within decades. In the meanwhile, our probe on the smaller-scale cross-isobath current, with a value of a few centimeters per second, is constrained by the observational difficulties. However, the cross-isobath current is a treasure trove to understand the vertical movements and the possible deep mixed layer formation due to its horizontal inhomogeneity and ageostrophic component mainly.

To explain the reason of the vertical motion is one of remaining research tasks, and the researchers have attempted to understand it from different mixing scales and abled to simulate the diapycnal mixing. If we presume a two-dimensional water column, namely a circulation in a cross-isobath profile without along-isobath dependency (it is a reasonable presumption since the non-divergence geostrophic current leads to the along-isobath current), then studying the cross-isobath current is helpful to understand the vertical motions.

In the upstream of the East Sakhalin, backscatter strength data of the Acoustic Doppler Current Profilers (ADCP) indicates the intense upward sediments transport within the whole water column with a depth of 100m, suggesting a deep mixed layer formation. What's more, the observation in the shelf break of the northeast of the Hokkaido Island by the icebreaker Soya in February 1997 detected a mixed layer with a depth around 300m. The mixed layer is considered originating from the East Sakhalin and entrained by

the East Sakhalin Current (ESC). Meanwhile, the relation between the upstream winter mixing and the downstream spring bloom along the ESC was uncovered.

With climate change, the deep mixed layer, as a demarcation of the coast and the open ocean, may get more attentions, since there is an interesting phenomenon that sea ice extends along the East Sakhalin and keeps its state in the whole winter, even though the sea ice in the same latitude of the center of the sea almost disappears because of the higher temperature water intruding from the North Pacific Ocean. Seemingly, the deep mixed layer may perform as a barrier to block the coastal colder and central warmer water exchange, and it would take an important role on the coastal sea ice survival if the global temperature rises continually in the future.

Strong wind events are considered as the reason of the strong mixing according to observations. However, we still lack of understanding on how wind attends to the construction of the deep mixed layer around the shelf break.

In my doctoral study, I mainly conducted numerical simulations using an Ocean General Circulation Model, named IcedCOCO (Iced- CCSR Ocean Component Model), to reproduce the circulation inside the Sea of Okhotsk and attempted to figure out the dynamics of the deep mixed layer formation. The simulation well reconstructed the ESC and a deep mixed layer immediately adjacent to a reversed Ekman Overturning (EOT). A great internal water stress was discovered dominating inside the reversed EOT, which is caused by a large vertical viscosity and geostrophic current vertical shear. The Ekman spiral exists in a layer where the water is driven by the wind stress and the earth rotation, and the water transport within the layer by the spiral turns to the right-hand side of the wind stress in

the northern hemisphere normally, while we found that when the internal water stress is much larger than the wind stress, the spiral would be reversed compared to a normal one. A deep mixed layer can form when this reversed EOT converges with a normal Ekman current, which is considered as the reason of the deep mixed layer formation around the East Sakhalin's shelf break, where a reversed EOT is in the gently sloping shelf and a normal one locates on the neighboring open ocean.

A scaling analysis was used to parameterize the geostrophic stress and the vertical viscosity, and we evaluated the parameterized geostrophic stress in other coastal areas with freshwater discharge where the geostrophic stress might be dominant. The results indicate a larger geostrophic stress than the surface wind stress in these regions which implies that the dynamics could be applied into various coastal frontal regions. Moreover, several sensitivity experiments were conducted to find out about the reason of the coastal front's generation, and we found that the freshwater discharge from the Far East continent accompanying with the wind contribute to a farther offshore front.

The estimated geostrophic stress around the northwest of the Gulf of Alaska (GOA) is very close to the COCO simulation, even though a rather low-resolution simulation. For a further investigation, I studied the upwelling system around the northwestern GOA in winter solely with the high-resolution model data, Ocean General Circulation Model for the Earth Simulator version 2(OFES2), to estimate the application of the above theory to the northwestern GOA. The study indicates that the geostrophic stress dynamics can be used to explain the strong convection in the water mass shallower than 100m in the west end of the Shelikof Trough and the confluence of the Alaska Coastal Current and the Alaska Stream. The thorough discussions are encapsulated in the thesis.

This page intentionally left blank

Contents

Abstract *1*

General introductions: *7*

1.1 Background information of the (modified) Ekman spiral **9**

1.2 Applications of the (modified) Ekman spiral **16**

1.2.1 Application to an open ocean 17

1.2.2 Application to a coastal region 18

1.3 Scope of the present study **19**

Figures and tables **22**

Case1: Sea of Okhotsk *29*

2.1 Introduction **30**

2.2 Model and data description **34**

2.2.1 Modelling configuration 34

2.2.2 Isobath coordinate 37

2.2.3 Data for estimating the geostrophic stress in various coastal areas 38

2.3 Results and discussions **40**

2.3.1 Overview of the modelled ESC 40

2.3.2 Vertical overturning from the flow field in the upstream ESC 45

2.3.3 Vertical overturning based on stress distribution in the upstream ESC 46

2.3.4 Effect of geostrophic stress on the stress distribution 49

2.3.5 Response of internal water stress and vertical overturning to the riverine discharge 52

2.3.6 Scaling analysis of the geostrophic stress and its applicability to various frontal coastal regions 54

2.4 Summary **59**

Appendix **62**

Appendix 1 62

Appendix 2 64

Appendix 3 66

Figures **68**

Case2: Northwestern Gulf of Alaska *87*

3.1 Introduction **88**

3.2 Model and data analyses **92**

3.2.1 North Pacific submesoscale-permitting simulation 92

3.2.2 Following the sea surface height (SSH) coordinate 93

3.2.3 Along-isobath averaged variables 94

3.2.4 Climatological monthly mean wind field 94

3.3 Results **95**

3.3.1 Simulated flow field in the northwestern GOA 95

3.3.2 Wind field in the northwestern GOA 97

3.3.3 Strong upwelling along the ACC and AS 98

3.4 Summary and discussion **106**
Figures **109**
General discussions *125*
4.1 Extension of the Case1 ..... **128**
4.2 Extension of the Case2 ..... **132**
Figures **133**
References *137*
For Chapter 1 ..... **137**
For Chapter 2 ..... **137**
For Chapter 3 ..... **142**
For Chapter 4 ..... **142**
Acknowledgements *147*

Chapter 1

General introductions:

(modified) Ekman theory and its applications

Ekman's theory is one of the fundamental disciplines of the oceanic dynamical theories. The study was encouraged by the oceanographer and explorer *Fridtjof Nansen*, who learnt a lesson from the experience of the '*Jeannette expedition*', by virtue of the ocean current and the ship '*Fram*' went across Arctic area successfully accompanying with other eleven partners (Fleming, Fergus 2002). Even though they did not arrive at the north pole eventually, the expedition is instructive for comprehending the polar oceanic environment and the strenuous polar voyage at that era. One of important discoveries in Nansen's expedition is that he found icebergs did not be drifted along the wind direction but turned to right-hand side of the wind direction around 25°. To get an understanding on the phenomenon, he encouraged *Vagn Walfrid Ekman* to study the wind drift current systematically. Ekman with his analytical model verified the current conforms to the 'force' balance between the wind friction and the inertial force due to the earth rotation. In his thesis, he discussed the contemporarily well-known and broadly adopted 'Ekman spiral'.

Ekman's theory is significant in theoretical and realistic understanding on the water motion in the ocean boundary layer. Here, an additional condition and the alteration of the Ekman dynamics as a result are further discussed. A region where the wind stress is no longer the only one dominant stress is considered. The additional stress stems from the water with horizontal density gradient (i.e., the horizontal stratification), typically in a frontal zone, which is not included in the Ekman's theory. The importance of the horizontal stratification is that it can generate a current shear according to the thermal wind relation. The current shear is conducive to a stress generation inside the surface boundary layer, and regulates the wind stress influence on the water, namely the Ekman

spiral, further. As the stress derived from the vertical shear of the geostrophic current, it is named as the '*geostrophic stress*' (e.g., Cronin and Kessler, 2009).

The structure of the Chapter 1 is organized as follows. The Ekman's analytical solution and the depicted features are introduced briefly first. Then, a modified Ekman's analytical solution by the geostrophic stress is established. After that, the applications of the modified Ekman theory into an open ocean and a coastal frontal region are presented, respectively. Within this section, it is anticipated to be recalled that the classic Ekman theory and to be understood that how the Ekman's theory is adapted with the horizontal stratification. In the meantime, the content is anticipated to fill our understanding gap on the Ekman's theory. We can have a deep thinking on the concept of the 'geostrophic stress' which is derived after introducing the 'stratification' into the boundary layer and how the 'geostrophic stress' takes its part in the regulation of the classic Ekman spiral. Specific questions that are solved in this thesis and originality of this study are described at the end of this chapter.

1.1 Background information of the (modified) Ekman spiral

1.1.1 Classic Ekman spiral

Dating back to 1905, Vagn Walfrid Ekman studied the water layer where the wind provokes flows significantly, and he mainly considered two typical oceanic environments. The first one is to presume the depth of water column is infinite, namely the whole layer's depth extends far deep compared to the depth of the wind-current. The presumption for the second oceanic environment is the depth of the wind-current is comparable with the whole layer depth. A stationary state is depicted with the following equations (1-1) with the consideration of the earth's rotation (noting that in the Ekman's idealized model he

did not consider the water stratification and the solved current is the ageostrophic component only),

$$\begin{cases} fv + A_V \dfrac{\partial^2 u}{\partial z^2} = 0 \\ -fu + A_V \dfrac{\partial^2 v}{\partial z^2} = 0 \end{cases} \quad (1-1)$$

where $f = 2\omega\sin\varphi$ is the vertical component of the Coriolis parameter, ω is the angular velocity of the earth rotation with a value of 0.0000729; φ is the latitude in a geographic coordinate. The other variables' notations are following the convention defined in Table 1.1, and if without a particular declaration the setting is adopted in the following text of the Chapter 1. Considering wind blows along the positive direction of the y axis, the boundary conditions for the first situation with an infinite ocean, are set as,

$$\begin{cases} A_v \rho_0 \left.\dfrac{du}{dz}\right|_{z=0} = 0 \\ -A_v \rho_o \left.\dfrac{dv}{dz}\right|_{z=0} = \tau_s \\ u = v = 0, z \to -\infty \end{cases}$$

We can find the explicit solutions of the equations, which are the ageostrophic current, as,

$$\begin{cases} u = V_0 e^{-az}\cos(45° - az) \\ v = V_0 e^{-az}\sin(45° - az) \end{cases} \quad (1-2)$$

where $a = \sqrt{\frac{f}{2A_v}}$, $V_0 = \frac{\tau_s}{\sqrt{f A_v \rho_0{}^2}}$

The direction of flow rotates with depth z and the rotate angle λ is,

$$\lambda = \arctan\frac{v}{u} = \frac{\sin(45° - az)}{\cos(45° - az)} \quad (1-3)$$

Evidently, the depth D of the level where the water velocity is opposite to the surface velocity is,

$$D = \frac{\pi}{a} = \pi\sqrt{\frac{2A_v}{f}}$$

The general meaning of the depth D is a depth within the frictional influence, and is named as the Ekman layer thickness.

For the second situation, considering a finite ocean, in this case the surface and bottom boundary layer interaction is taken into account, and the Ekman's solution is then converted as,

$$\begin{cases} u = A\sinh a\zeta\cos a\zeta - B\cosh a\zeta\sin a\zeta \\ v = A\cosh a\zeta\sin a\zeta + B\sinh a\zeta\cos a\zeta \end{cases} \qquad (1-4)$$

$$A = \frac{\tau_s D}{A_v \rho_0 \pi}\frac{\cosh ah\,\cos ah + \sinh ah\,\sin ah}{\cosh 2ah + \cos 2ah}$$

$$B = \frac{\tau_s D}{A_v \rho_0 \pi}\frac{\cosh ah\,\cos ah - \sinh ah\,\sin ah}{\cosh 2ah + \cos 2ah}$$

where ζ denotes the distance from the bottom, i.e., $\zeta = z + h$.

The velocity profiles of equation (1-2) and (1-4) are depicted as the Fig. 1.1, which represents the pattern of the Ekman spiral in a deep ocean and a shallow region, respectively, according to the Ekman's solutions. As the sky-blue line in the Fig. 1.1b which owns a water depth $h = 0.1 \times D$, we can obtain an explicit conclusion that when the water depth is far shallower than the Ekman layer thickness, the surface and bottom Ekman layer interact with each other and the flow is mainly along the wind stress direction. In the Table 1.2, a summary of the relation between water depth and the surface current deflection regarding the wind stress direction is provided, and the results are calculated following the Ekman's solution, as the equation (1-3). The results show that when the water depth is not shallower than the Ekman layer thickness, the surface

current rotates 45° to the wind stress direction. While the water depth is smaller than the Ekman layer thickness, the shallower of the water depth, the closer of the current is to the direction of wind stress.

1.1.2 Modified Ekman spiral by the 'geostrophic stress'

In this subsection, the effect of the geostrophic stress $\vec{\tau}_p = A_V \frac{\partial \vec{u}_g}{\partial z}$ on the Ekman dynamics (specifically via the boundary conditions in an analytical model) is discussed, where $\vec{u}_g$ denotes the geostrophic current vector. Recalling that, the Ekman dynamics is related only to the ageostrophic current and the stress generated by the ageostrophic current shear.

Regarding the momentum equation, if the current is separated into the geostrophic and ageostrophic components, i.e., $\vec{u} = \vec{u}_g + \vec{u}_a$, the water stress $\vec{\tau}$ may then be written as the summation of the ageostrophic stress and the geostrophic stress, as follows,

$$\vec{\tau} = \vec{\tau}_a + \vec{\tau}_p = A_V \frac{\partial \vec{u}_a}{\partial z} + A_V \frac{\partial \vec{u}_g}{\partial z},$$

where $\vec{u}_a$ denotes an ageostrophic current vector and $\vec{\tau}_a$ denotes the ageostrophic stress that stems from the vertical shear of $\vec{u}_a$. Assuming that the geostrophic stress $\vec{\tau}_p$ is independent of z, i.e., $\frac{\partial \vec{\tau}_p}{\partial z} = 0$, the momentum equation for ageostrophic current (regarding to the Coriolis force) can be expressed as:

$$\begin{cases} -f v_a = A_v \frac{\partial^2 u_a}{\partial z^2} \\ f u_a \ = A_v \frac{\partial^2 v_a}{\partial z^2} \end{cases}, \qquad (1-5)$$

which is same as the Ekman's equation (1-1).

A vertical independent geostrophic stress, $\vec{\tau}_p = \rho_0 A_v \frac{\partial \vec{u}_g}{\partial z}$, may arise when the geostrophic current shear and A_v are uniform in terms of z. Note that the vertically independent geostrophic shear and A_v are not necessary conditions for producing a modified Ekman overturning, but they are assumptions here that are used to solve the equation and obtain an analytical solution conveniently as described below. A more general solution (Equation (2-1)) was resolved by an Ocean General Circulation Model, model COCO, (details are introduced in the Chapter 2) where the geostrophic current vertical shear and A_v are vertically dependent and a modified Ekman overturning was resolved as well.

Regarding the boundary conditions, considering an along-isobath wind τ_s^y as an imposed dynamical source, the boundary conditions on the along-isobath direction on the water column's surface $z = 0$ and bottom $z = -h$ are written as,

$$\begin{cases} \tau_s^y = \tau_a^y + \tau_p^y = \rho_0 A_v \left.\frac{\partial v_a}{\partial z}\right|_{z=0} + \rho_0 A_v \left.\frac{\partial v_g}{\partial z}\right|_{z=0} \\ \tau_b^y = \tau_a^y + \tau_p^y = \rho_0 A_v \left.\frac{\partial v_a}{\partial z}\right|_{z=-h} + \rho_0 A_v \left.\frac{\partial v_g}{\partial z}\right|_{z=-h} \end{cases},$$

where τ_s^y (τ_b^y) the surface wind (bottom) stress is a given force. y denotes along isobath direction. x denotes the cross-isobath direction. A two-dimensional structure is assumed, namely ignore the variance in the along-isobath direction. $\vec{\tau}_a$ is the stress remaining to be solved. Therefore, it may be convenient to write the surface and bottom boundary conditions in terms of ageostrophic stress such that

$$\begin{cases} \left.\tau_a^y\right|_{z=0} = \tau_s^y - \tau_p^y = \tau_s^y - \rho_0 A_v \left.\frac{\partial v_g}{\partial z}\right|_{z=0} \\ \left.\tau_a^y\right|_{z=-h} = \tau_b^y - \tau_p^y = \tau_b^y - \rho_0 A_v \left.\frac{\partial v_g}{\partial z}\right|_{z=-h} \end{cases}. \qquad (1-6)$$

In the cross-isobath direction, I assume that the ageostrophic flow shear is weak at $z = 0$ and $z = -h$ and does not exert much stress. Then, the boundary condition in the cross-isobath direction is:

$$\left.\frac{\partial u_a}{\partial z}\right|_{z=0,\ z=-h} = 0.$$

Note that τ_p, the '*geostrophic stress*' is not an enforced stress, but rather the one is given by the stratification. So that for a constant τ_p, equations (1-5) and (1-6) can be solved in terms of u_a, such that:

$$W = u_a + iv_a$$

$$= \frac{1+i}{2} D \frac{\tau_s - \tau_p}{\rho_0 A_v} \frac{\cosh\left[(1+i)\frac{z+h}{D}\right]}{\sinh\left[(1+i)\frac{h}{D}\right]} - \frac{1+i}{2} D \frac{\tau_b - \tau_p}{\rho_0 A_v} \frac{\cosh\left[(1+i)\frac{z}{D}\right]}{\sinh\left[(1+i)\frac{h}{D}\right]} \quad , \qquad (1-7)$$

where D denotes the Ekman layer thickness $D = \sqrt{(2A_v)/f}$. The solution was compared to the one obtained using the theoretical analysis reported by Chen and Chen (2017), and they presumed that the bottom stress is the same as the surface stress. In their case, the sign of the ageostrophic flow depended on the relative magnitude between the wind stress and the geostrophic stress. However, over a frontal mid-shelf like the upstream East Sakhalin Current (as we discussed in the Chapter 2), when τ_b is no longer predominant compared to the surface wind stress, the relative magnitude between the surface wind stress and the geostrophic stress as well as the parameters on the latter half of the right-hand-side of equation (1-7), jointing the bottom stress, plays a major role in deciding the sign of the ageostrophic current and the volume of the transport, and the shape of Ekman spiral.

The modified Ekman spirals are presented in the Fig. 1.2. According to the analytical solution (1-7), if there is no horizontal stratification (namely there is no geostrophic

stress) while the surface wind stress and bottom stress have the same magnitude and direction, a surface and bottom Ekman spirals are depicted, with a near-surface (near-bottom) spiral turning to the right (left) with respect to the surface (bottom) stress as in Fig. 1.2a. This is a classical response of the Ekman layer to an imposed stress with a finite depth. After considering the horizontal stratification, the generated geostrophic stress will modify the Ekman spiral.

When the geostrophic stress is larger than the surface wind stress and bottom stress, the Ekman spiral is possibly reversed compared to the classical one, such as those shown in Fig. 1.2b. The difference between the classical Ekman spiral and the reversed Ekman spiral comes from the boundary condition (1-6). If $\tau_s^y < \tau_p^y$, then $\tau_a^y < 0$ at surface according to (1-6). This means that the water at surface is not driven by wind stress but dragged by wind stress, causing an ageostrophic stress divergence $\frac{\partial \tau_a}{\partial z}$, the force, with an opposite sign compared to that in the classic Ekman layer. Therefore, the ageostrophic flow $u_a = \frac{1}{f\rho_0}\frac{\partial \tau_a^y}{\partial z}$ is reversed according to the momentum equation. Further, Fig. 1.2(c) presents how a bottom stress modifies the bottom Ekman transport. A smaller bottom stress coupled with geostrophic stress can induce a greater bottom Ekman transport.

As for a vertical dependent τ_p, it can be confirmed from the momentum equations

$$\begin{cases} f\hat{z} \times \vec{u}_g = -\dfrac{1}{\rho_0}\nabla P \\ \dfrac{1}{\rho_0}\dfrac{\partial P}{\partial z} = b - g \end{cases} \qquad (1-8)$$

where $\hat{z}$ denotes the unit vector in the vertical direction. b is buoyancy and $b = g(\rho_0 - \rho)/\rho_0$. As for the second equation of equation set (1-8), after combining with the vertical hydrostatic relation, we can get a geostrophic current shear as,

$$\frac{\partial \vec{u}_g}{\partial z} = \frac{1}{f}\hat{z} \times \nabla b. \qquad (1-9)$$

Thus, the geostrophic stress can be calculated with the geostrophic current shear as,

$$\vec{\tau}_p = \rho_0 \mathrm{A}_v \frac{\partial \vec{u}_g}{\partial z} = \frac{\rho_0 A_v}{f}\hat{z} \times \nabla b.$$

Practically, the geostrophic stress $\tau_p^y = \rho_0 \mathrm{A}_v \frac{\partial v_g}{\partial z}$ is not constant in terms of depth in the reality. Therefore, the force by geostrophic stress shear inside the boundary layer should be included in the ageostrophic momentum equation (1-5). Namely, for a water parcel inside a stratified boundary layer, it feels the force from the internal water stress to accelerate, and the internal water stress contains both influence of the geostrophic stress and the ageostrophic stress. A crucial point in the later analysis is to calculate the internal water stress, as it is the 'internal water stress' that drives the ageostrophic current which as the study interest.

1.2 Applications of the (modified) Ekman spiral

In this subsection, two applications about the geostrophic stress modified Ekman layer are introduced mainly. One is an observation by Cronin and Kessler (2009) which captured an unusual phenomenon near the equatorial region. I prefer to explain this example is because it is the only observed result that directly derived from the modified Ekman current, although it does not happen around the coast. Another example is a coastal application elucidated by Chen and Chen (2017) who dealt with the geostrophic

stress theoretically and numerically in a coastal upwelling region controlled by a downwelling-favorable wind.

1.2.1 Application to an open ocean

In the region close to but off the equator, the geostrophic current shear may predominate since a small f there according to the thermal wind relation (1-9). A great geostrophic stress is further generated due to the great geostrophic current shear. We may infer that close to the equator the Ekman spiral is possibly modified according to the above discussions.

Cronin and Kessler (2009) analyzed the mooring data from Tropical Atmosphere Ocean (TAO) project in the top 25m depth near the $2°N, 140°W$ during May~Oct. 2004. As shown in Fig. 1.3a, the observed mean current (black arrow) is mainly westward and turns to left regarding the wind stress direction (marked by 'wind'). When subtracting the mean geostrophic current from the observed current, they obtained the ageostrophic current (brown arrow) that flows northward and exhibits an angle turning to the right with respected to the wind direction, which looks qualitatively consistent with the classical Ekman theory. Quantitatively, however, they further argued that an unrealistically large vertical viscosity was needed to reproduce the turning angle; the current generated by the wind stress according to the classic Ekman theory should be like the pattern in Fig. 1.3b, Then, they wondered how to understand the observed current which does not follow the classical Ekman theory. Finally, they found that, after subtracting the geostrophic stress from the wind stress at surface as in (1-6), they obtained the surface water stress $\vec{\tau}_a|_{z=0}$ (they denoted it as $\vec{\tau}_{eff}$; see also the arrow marked by $\boldsymbol{\tau}_a$ in Fig. 1.3a) which generates an ageostrophic current inside the water closely following the Ekman's theory. In other words, the combination of the

ageostrophic current driven by $\vec{\tau}_{eff} = \vec{\tau}_a|_{z=0}$ and geostrophic current approximates the observed current.

In this observed example, the current in the mixed layer is still driven by the wind stress, although it has been dramatically modified by the geostrophic stress. The Ekman's theory is useful to explain the ageostrophic motion. However, we need to be very careful to deal with the ageostrophic stress at surface, which is no longer the wind stress itself after inviting the stratification into the system.

1.2.2 Application to a coastal region

The Ekman spiral adjustment around coastal regions may also not be overlooked, as the strong horizontal buoyancy gradient may be generated there by the river discharge, ice melting water along the coast or the heavy water intruding from the deep ocean. A downwelling-favorable wind may be dynamically important for the frontogenesis (Thomas and Lee 2005). Then again, the geostrophic current shear may predominate in a coastal region according to the thermal wind relation (1-9).

The observation related to a geostrophic stress modified Ekman transport around the coastal region is difficult. One of reasons may be that along the coast, the geostrophic along-shore current is far stronger than the ageostrophic current which dominates observed values, then it would be a difficult work to separate the ageostrophic component from the observation. While, there are several suggestive idealized simulations (e.g., Moffat and Lentz, 2012; Spall and Leif, 2016; Chen and Chen, 2017).

In the Figure 2 by Chen and Chen (2017), they reproduced a reversed Ekman overturning within a depth 15m, namely reproduced a coastal upwelling under a downwelling-

favorable wind, when the horizontal stratification is intensified (see also Fig. 1.4). As explained above, if the surface wind stress is weaker than the geostrophic stress, then ageostrophic stress at surface, $\vec{\tau}_{eff} = \vec{\tau}_a|_{z=0}$, has an opposite sign to that of the wind stress according to (1-6). This means that the water at surface is not driven by wind stress but dragged by wind stress. Specifically, the water parcel responds to the force balance between the ageostrophic stress divergence $\frac{\partial \tau_a}{\partial z}$ and the Coriolis force. As a result, a negative $\frac{\partial \tau_a}{\partial z}$ contributes to a reverse Ekman transport. Likewise, the ageostrophic flow $u_a = \frac{1}{f\rho_0}\frac{\partial \tau_a^y}{\partial z}$ is reversed according to the momentum equation (the application of this solution is discussed in the Chapter 2. Indeed, it was found that Chen and Chen's explanation in their Fig. 6 would not be very relevant for the reverse overturning mechanism itself). Overall, the key point is when the geostrophic current shear is larger than the 'wind-support' current shear, a reversed Ekman overturning may be generated.

When I studied the mixed layer formation around the shelfbreak of the Sea of Okhotsk, I found a similar dynamic question, which is studied from the viewpoint of the Ekman transport and is considered to be different from and maybe simpler than the previous studies.

1.3 Scope of the present study

In this study, an important application of the modified Ekman theory around the coast is considered as to facilitate the deep mixed layer formation. More specifically, a mixed layer sometimes deepens offshore of a shelf break, where a gently sloping shelf connects to the deep open ocean, with a downwelling-favorable wind. The depth of the deep mixed layer is deeper than the thickness of the mixed layer in the open ocean. This suggests that

there would be a downwelling generation under a downwelling-favorable wind at the shelf break where there is not a wall. It is an unresolved question till now that how the downwelling occurs at the shelf break without a lateral boundary.

This study proposes that the modified Ekman overturning over a shelf is a key point to understand this downwelling and formation of the deep mixed layer. On the other hand, upwelling occurs on the onshore side of the front once the Ekman overturning is reversed. This implies that the front may work as a 'virtual wall'. That is, a freshwater front may form over a gently sloping shelf by freshwater discharges from rivers and/or ice melting. Thermal wind shear would then be generated and cause geostrophic stress over the gently sloping shelf, resulting in producing a modified (or even reversed) Ekman overturning there. If the reverse overturning encounters a normal onshore Ekman transport from the open ocean, as a schematic pattern in Fig. 1.5, it causes downwelling and forming a deep mixed layer at the shelf break. The mixed-layer formation process will be studied in the later chapters. Related applications have been realized with Ocean General Circulation Model off the Sakhalin coast in the Sea of Okhotsk and the northwest of the Gulf of Alaska. We can find more discussions about these two cases in the Chapter 2 and Chapter 3, respectively.

Concurrently, based on the above background information, another study interest is whether the analytical model with a constant geostrophic stress is applicable to real coastal regions without the simplification, since the theoretical model assumes two simplified conditions, which are:

(1) a vertical independent vertical turbulent viscosity

(2) a vertical independent geostrophic current shear.

With these simplified conditions, the geostrophic stress can greatly modify the Ekman spiral, or even reverse it, in a shallow coastal region. However, we still do not have ideas on:

(1) What will happen in a complicated realized model with a vertical dependent parameter? Is the analytical solution (a significant geostrophic stress and a modified Ekman spiral) still applicable in a complicated realized model?

(2) What is the connection and how to connect the reversed Ekman overturning and the deep mixed layer?

In the later chapters, a viewpoint of the Ekman transport is used to understand the modified overturning. Compared to figuring out dynamics of the modified Ekman spiral, the study interests are applying the process onto a deep mixed layer and upwelling formation away from coastal boundaries. The linkage between the overturning and the deep mixed layer formation has not been discussed previously; via the model simulation the study reveals that they would have connections and can explain the deep mixed layer formation around the shelfbreak of the Sea of Okhotsk. It is one of creativities of this study. Moreover, the geostrophic stress dynamics is used to explain the upper layer upwelling in the northwestern Gulf of Alaska.

Figures and tables

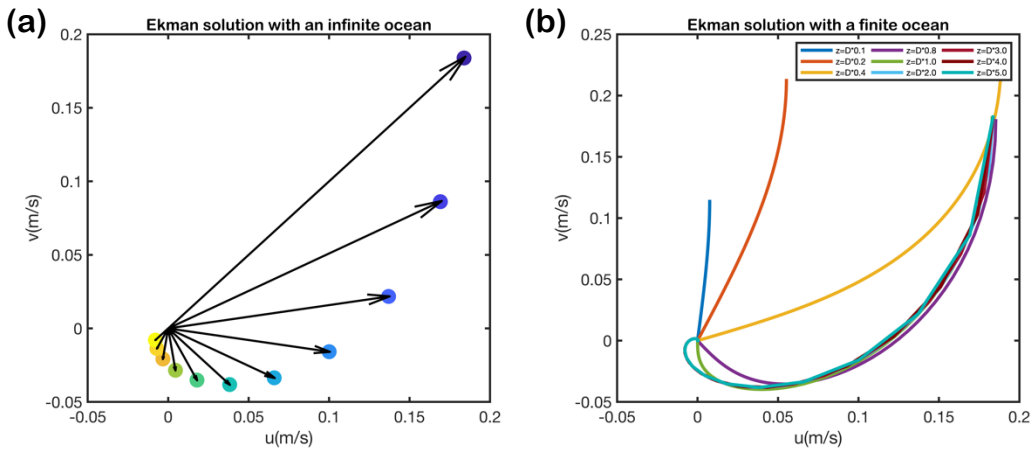

Figure 1.1 Ekman's solution in an infinite (finite) ocean

a. Ekman's solution in an infinite ocean, which corresponds to the equation (1-1). The arrow pointing to the dark blue dot denotes the surface current. The sequential color shading from blue to yellow corresponds to water layer $z = \frac{i}{10} \times D, i = 0{:}\,1{:}\,10$, where D is the Ekman layer thickness. **b.** Ekman's solution in a finite ocean, which corresponds to the equation (2). Each line with different color as the legend denoted represents the solution with ocean depth d equal to

$0.1D, 0.2D, 0.4D, 0.8D, 1.0D, 2.0D, 3.0D, 4.0D, 5.0D$, respectively.

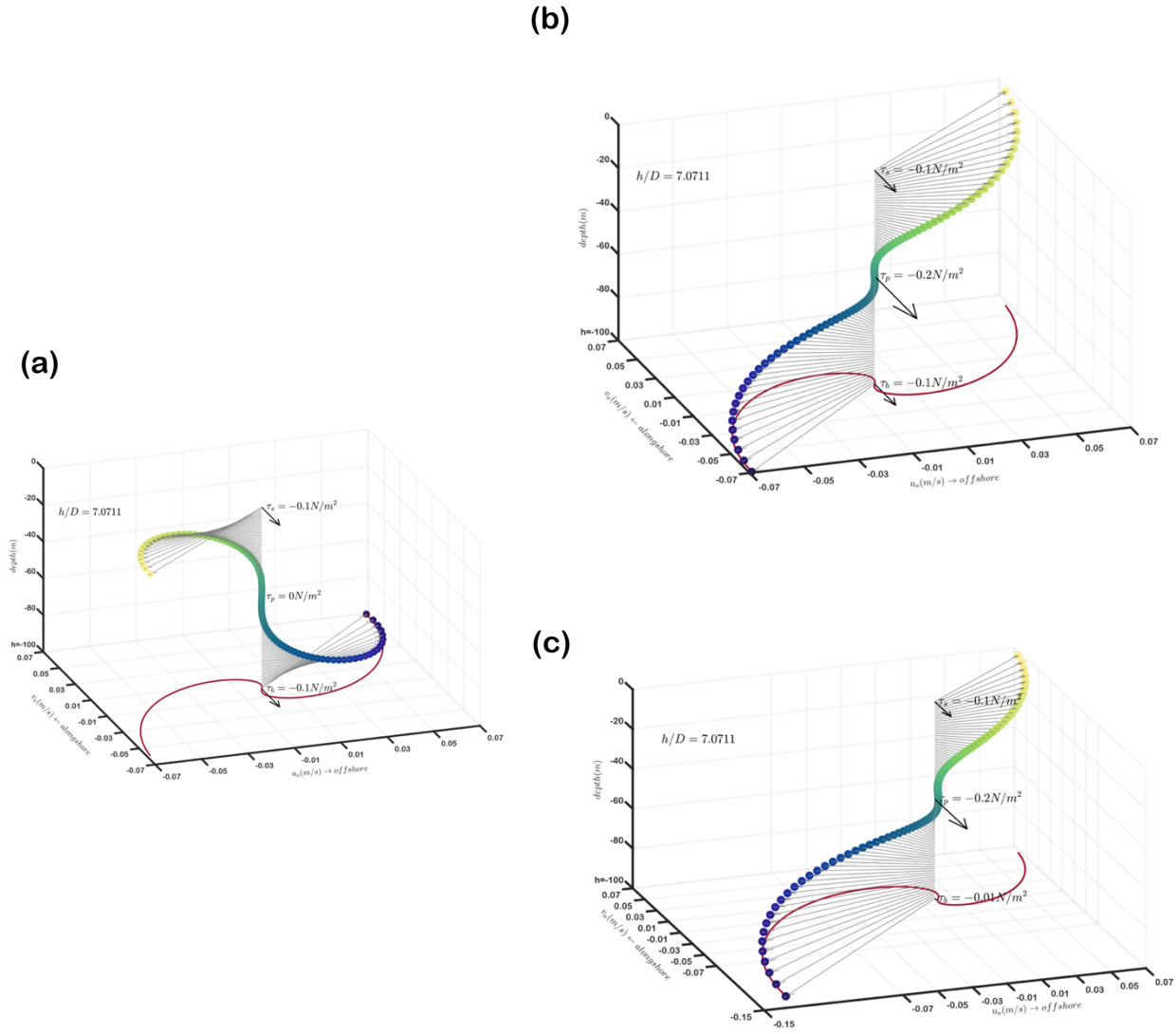

Figure 1.2 (modified) Ekman spiral

The (modified) Ekman spiral from the solution (1-3), where $h = 100m$ is the whole layer depth, D is the Ekman layer thickness. The ratio $\frac{h}{D} = 7.0711$. **a.** an Ekman spiral with $\tau_s = \tau_b = -0.1N/m^2$ along shelf, $\tau_p = 0N/m^2$. **b.** a reversed Ekman spiral with $\tau_s = \tau_b = -0.1N/m^2$, $\tau_p = -0.2N/m^2$ along shelf. **c.** an Ekman spiral with $\tau_s = -0.1N/m^2$, $\tau_b = -0.01N/m^2$, $\tau_p = -0.2N/m^2$ along shelf.

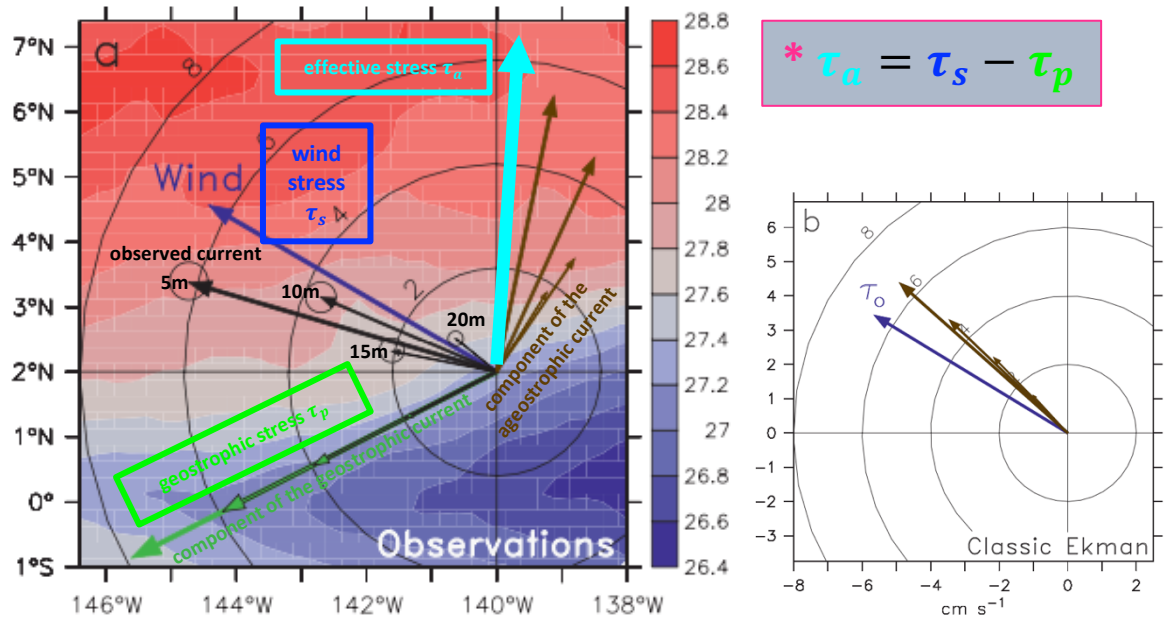

Figure 1.3 (figure source: Cronin and Kessler 2009, Fig 2; modified)

Geostrophic stress modified Ekman spiral in the equatorial area, at $2°N, 140°W$. **a.** the black arrows are the observed current, and the arrow length denotes different water depth (5m, 10m, 15m, 20m), the shorter the deeper. The blue arrow marked by 'wind' denotes the wind stress direction. The blue arrow marked by the 'τ_a' denotes the ageostrophic stress, which is not the wind stress, but wind stress minus the geostrophic stress. The green arrows denote the geostrophic current, with the same direction of the geostrophic stress. The brown arrows denote the ageostrophic current which is the observed current minus the geostrophic current. Shading denotes the sea surface temperature. **b.** The blue arrow is the wind stress, whose direction is same as the one in Fig 1.3(a) marked by the 'wind'. Brown arrows denote the current by the wind stress according to the Ekman's solution.

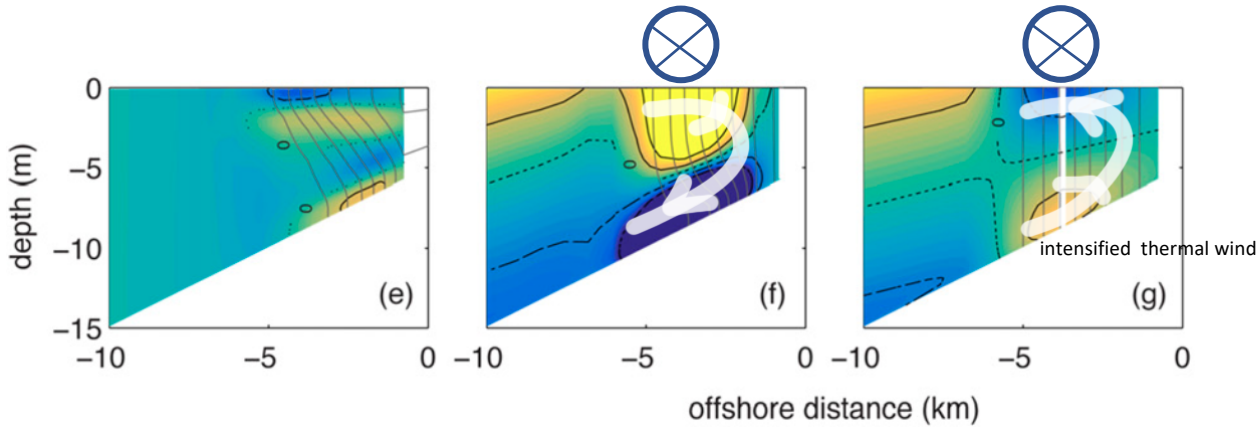

Figure 1.4 (figure source: Chen and Chen 2017, Fig 2; modified)

They tested a coastal overturning where there is a freshwater bulge at the upstream initially and a downwelling-favorable wind is imposed after ten days. The color shading denotes the cross-shelf velocity with the yellow denotes the onshore current and the blue denotes the offshore current. In figure (e), it denotes the initial current and stratification states. The current pattern is converted to as the figure (f) after adding a downwelling-favorable wind. With the freshwater bulge transports to the downstream, the thermal wind is enhanced as the figure (g). In the meantime, the cross-shelf overturning is reversed compared to the figure (f).

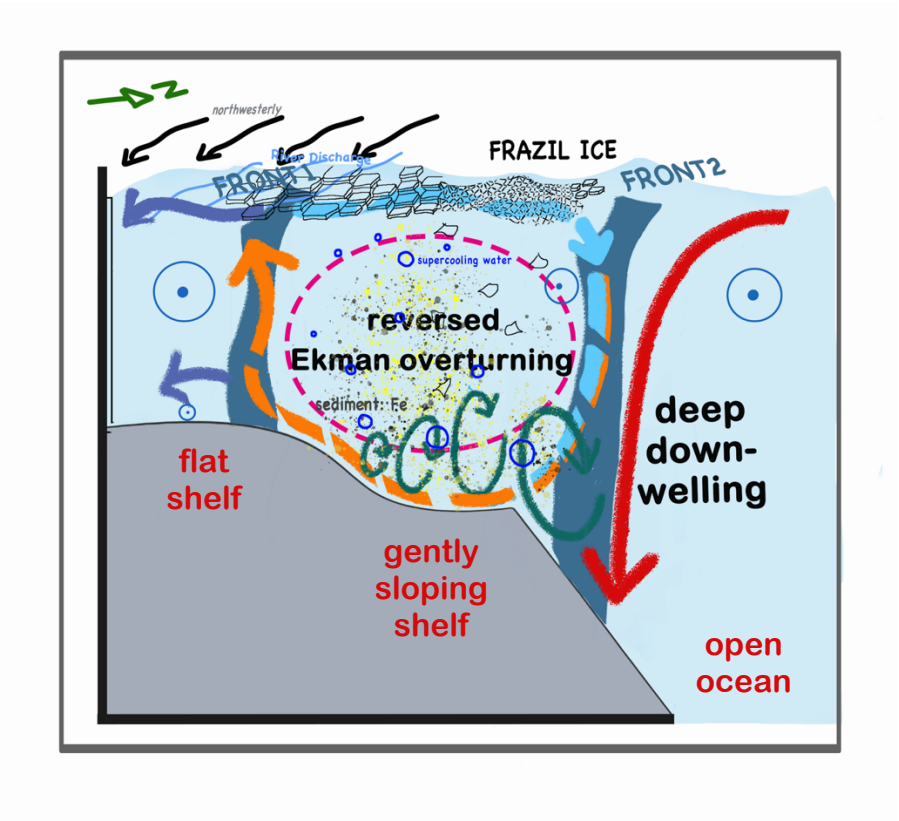

Figure 1.5 Schematic of a shelf break deep mixed layer formation

Based on the previous study, this study extends the application of the reversed Ekman overturning to explain a shelf break deep mixed layer, which is explained as the convergence between a reversed Ekman overturning in the gently sloping shelf and a normal Ekman transport in the open ocean with analyzing the model simulation.

Table 1.1

Common symbols: symbols used in the analytical Ekman model configuration are listed inside the table

symbol of variable	long name
f	Coriolis parameter
A_v	vertical turbulent viscosity
u	cross-shelf (in the x direction) current
v	along-shelf (in the y direction) current
ρ_0	a reference density of the ocean
$\vec{\tau}_p = \rho_0 A_v \frac{\partial \vec{u}_g}{\partial z}$	geostrophic stress
$\vec{\tau}_a = \rho_0 A_v \frac{\partial \vec{u}_a}{\partial z}$	water stress
$\vec{\tau}_s(\tau_s^y)$	wind stress (in an along-shelf direction)
$\vec{\tau}_b(\tau_b^y)$	bottom stress (in an along-shelf direction)
$b = \frac{g(\rho_0 - \rho)}{\rho_0}$	buoyancy
g	gravity
$subscript_g$	geostrophic component of the current/stress
$subscript_a$	ageostrophic component of the current

Table 1.2

The relation between the water depth and the surface current deflection according to the Ekman's solution.

	water depth	surface current deflection °
$D = \pi \times \sqrt{\frac{\mu}{q\omega sin\varphi}}$ $= 1.6171$ (Ekman layer thickness)	0.1D	3.7603
	0.2D	14.4987
	0.4D	39.5247
	0.8D	45.7151
	1.0D	45
	2.0D	45
	3.0D	45
	4.0D	45
	5.0D	45

Chapter 2

Case1: Sea of Okhotsk

2.1 Introduction

The East Sakhalin Current (ESC) is located off the western coast of the Sea of Okhotsk, the southernmost marginal sea with sea ice production in the Northern Hemisphere. This current collects riverine discharges from the far-eastern Eurasian Continent, including the Amur River, which is the tenth largest river in the world. This river contains abundant nutrients such as iron, which is an essential micronutrient for phytoplankton growth in the subarctic North Pacific (Nishioka et al. 2014). Although the riverine iron is primarily deposited and sedimented on the ESC upstream shelf, the deposited iron is likely to be resuspended by strong wintertime mixing and therefore mingle with the surrounding water as well as become frozen into the sea ice (Ito et al. 2017) and then transported to the south. The transported mixed water and ice, which contain considerable iron (Kanna et al. 2014; Kanna et al. 2018), facilitate the next spring blooms not only in the southern Sea of Okhotsk (Mustapha et al. 2008) but also in the Oyashio and western North Pacific Ocean (Kuroda et al. 2019).

The ESC has two cores (Ohshima et al. 2002) (see also the arrows in Fig. 2.1a). The coastal core is a wind stress driven current characterized by the arrested topographic waves (ATWs); the ATWs accompanies the coastal current are constrained to the nearshore (Csanady 1978), which extend to Hokkaido Island (Ohshima et al.2002; Nakanowatari and Ohshima, 2014). The other core on the slope is considered the western boundary current (WBC) of the central cyclonic gyre (Ohshima et al. 2002; Ohshima et al. 2004; Ohshima et al. 2005). Although the along-shore dynamics of this current have been studied intensively, little information related to the relatively small cross-isobath component of the ESC and its coupled vertical circulation and mixing is available. The

ageostrophic cross-isobath current is subtle compared to the along-isobath current, but it is substantial for water mass exchange and for modulating the biogeochemical budgets (Brink 2016) in coastal areas (Federiuk and Allen, 1995; Pickart et al. 2000).

It is particularly difficult to observe the temperature and salinity as well as the nutrients in the ESC upstream during the winter because of the presence of sea ice (Mamontova, 2021; see also Fig. 2.1b for the model simulation's January mean sea ice concentration). Nevertheless, profiling float measurements detected mixed layer formation off the east coast of Sakhalin, which is as deep as 140 m along the shelf break in early winter (Ohshima et al. 2005). This mixed layer is significantly deep, as the mixed layer depth (MLD) in the Sea of Okhotsk is typically suppressed to less than 100 m (Uehara et al. 2012) because of the substantial freshwater input from the rivers around the Sea of Okhotsk, including the Amur River. Further, Ito et al. (2017) observed the resuspension of sediments via high-resolution backscatter measurements using an acoustic Doppler current profiler and found that vertical mixing occurs throughout the water column (> 100 m) near the shelf break in the ESC upstream. They conjectured that the resuspended materials, which contain iron, are entrained to the surface layer, frozen into the sea ice, and finally transported southward by the ESC.

Considering the difficulty of wintertime hydrographic observations off the Sakhalin, observations of the ESC by an ice breaker off Hokkaido in the south of the Sea of Okhotsk were suggestive, and similar well-mixed water masses were observed at the shelf break (Ohshima et al. 2005; Mizuta et al. 2004; Ohshima et al. 2001). The mixed water mass has a thickness larger than 200 m and contains sea-ice melting water as well as riverine discharge water from the far-eastern Eurasian Continent (Kanna et al. 2018), while the

water over the shallower shelf was stratified. This deep mixed water is characterized by high nutrient and iron concentrations, and it flows out from the Sea of Okhotsk as the Coastal Oyashio and fertilizes the western North Pacific (Kuroda et al. 2019). To obtain a better understanding of these structures, which are adjacent to the shelf break along the ESC, further study of the vertical circulation and mixed-layer formation is required.

The primary dynamical constituents characterizing the cross-shelf flow of the ESC in winter are a downwelling-favourable northwesterly wind from Siberia, the buoyancy flux from riverine discharge, and bottom friction. The air-sea heat exchange is insulated because sea ice covers the entire ESC coastal region (Fig. 2.1b). Idealized simulations indicate that when a downwelling-favourable wind drives an along-shelf current that is initially stratified, a well-mixed and relatively stagnant layer is formed inshore adjacent to the downwelling front (Allen and Newberger, 1996; Austin and Lentz, 2002). Additionally, the surface Ekman transport from the open ocean is blocked because of the coupling between the surface- and the bottom-boundary layers of the nearshore region (Mitchum and Clarke, 1986). However, once inshore stratification is derived from the riverine freshwater plumes, the cross-shelf overturning structure can be significantly modified via the internal water stress due to a thermal wind shear—the 'geostrophic stress'. In particular, when the geostrophic stress is higher than the wind stress, the Ekman overturning (EOT) adjacent to the coast is likely to be reversed. Previous coastal studies performed a reversed EOT with idealized simulations, and the geostrophic stress is noticeable inside riverine plumes that are ~15 m in depth (Chen and Chen, 2017; Moffat and Lentz, 2012; Lv et al. 2020), which is where the surface and bottom stresses are balanced. In this study, we focus on the shelf break fronts in the ESC that have deeper structures with a depth of ~100 m. Although a few studies have investigated the cross-

shelf overturning in a density front of this depth scale (e.g., Shcherbina and Gawarkiewicz, 2008), since the surface and bottom boundary layers are typically decoupled, its dynamics have not been effectively explored.

The effects of geostrophic stress on the surface mixed layer across a front were discussed separately in terms of the open ocean, including those associated with the tropical cold tongue as well as the Kuroshio Extension (Cronin and Kessler, 2009; Cronin and Tozuka, 2016). It was pointed out that the geostrophic stress significantly modifies the Ekman transport and results in upwelling and downwelling structures across the front. This dynamic consequently deepens the MLD on the downwelling side, which suggests that the upwelling/downwelling associated with the cross-shelf overturning impacts the deep mixed layer formation over the shelf break. Note that in the case of the ESC, the surface heat fluxes are insulated by sea ice (Fig. 2.1b), so the turbulent kinetic energy comes solely from the work of sea ice stress on the sea surface. Further, we disregard the residual overturning due to baroclinic instability (e.g., Spall and Thomas, 2016) because baroclinic eddies were not observed in the ESC shelf break front in the simulation.

In this paper, we elucidated that a reverse EOT dominates the cross-shelf transport in the ESC upstream by using an ocean general circulation model developed by the Atmosphere and Ocean Research Institute at the University of Tokyo (CCSR Ocean Component Model; hereafter referred to as COCO) (Hasumi 2000). The EOT deepens the mixed layer off the shelf break by blocking the onshore surface Ekman transport under the downwelling-favourable wind that occurs during winter. The reverse EOT, in addition to the accompanied upwelling and downwelling, occurs in the shelf break density front created by the riverine discharges from the far-eastern Eurasian Continent. This shelf break EOT

has a depth scale of 100 m. A scaling consideration implies the applicability of this EOT mechanism to various shelf break fronts of an O(100) m depth scale and suggests that the EOT and geostrophic stress significantly impact the water mass formation and material transport between the continental shelves and the open ocean.

2.2 Model and data description

2.2.1 Modelling configuration

The COCO model uses the hydrostatic and Boussinesq approximations, incorporates curvilinear horizontal coordinates (referred to as COCO's Mercator grids) and couples the sea ice model for diverse applications (Hasumi 2000; Matsuda et al. 2015; Shu et al. 2021). The brine rejection process is included in the sea ice module. In the model settings, sea ice contains 5 psu salinity, and during sea ice formation, the remainder of the salt is released to the ocean. In Matsuda et al.'s (2015) application, the dense shelf water along the middle layer of the west coast of the Sea of Okhotsk was simulated successfully with the COCO model.

In this study, we used COCO V3.4, which adopts the turbulence closure scheme (Noh and Kim 1999) to simulate the evolution of the oceanic surface and bottom boundary layers; however, the COCO model includes a slight modification of the turbulent Prandtl number, following the formulation by Kondo et al. (1978), As for the horizontal viscosity and diffusivity, COCO adopts a biharmonic version of the Smagorinsky viscosity (Smagorinsky, 1963) and diffusivity following the formulation by Griffies and Hallberg (2000), which are expressed as follows:

$$B_H = \frac{1}{8}\left(\frac{C\Delta^2}{\pi}\right)^2 D$$

where B_H denotes the biharmonic viscosity coefficient as well as the coefficient for the horizontal biharmonic diffusion. C is a nondimensional parameter, and the value we used in our simulation was 2.5. Δ is the spatial variable, and the chosen value is the smaller of Δx and Δy. D has a dimension of 1/s and denotes the deformation rate or strain (Griffies and Hallberg, 2000, for a specific form of D).

The simulated area encompasses the entire North Pacific Ocean (Fig. 2.1c) and extends to a southern boundary of 30°S, which was modelled as an open boundary with a sponge layer. Since the open boundary is considerable distance from our study area, its impact is negligible. For the solid boundaries, we used the non-slip boundary condition without normal flow.

In our simulation, we used the same grid setting as that of Matsuda et al. (2015). The horizontal resolution was finer than 3 km when modelling the Sea of Okhotsk's north-western continental shelf (Fig. 2.1a). Since the horizontal scale of the frontal eddies is O(10 km) (e.g., Spall and Thompson, 2016), the 3 km resolution is considered eddy-permitting. In the vertical direction, 7 surface σ layers were arranged at depths of less than 34 m to represent the surface elevations due to surface gravity waves, whereas 77 levels deeper than 34 m were assigned with z coordinates. The σ coordinate transformation is as follows:

$$z_s = \sigma_s \times (\eta - z_B) + z_B,$$

where z_B is the prescribed fixed depth. In this study, it was set as the depth of the seventh layer, which was 34 m. That is, the bottom was considered flat where the bathymetry was

shallower than z_B, i.e., the minimum depth was z_B =34 m. η is the surface water level, and $\sigma_s \in [0,1]$ from the seventh layer to the surface.

We used the six-hourly mean, ERA-Interim, from the European Centre for Medium-Range Weather Forecasts, and the period was June 1980–June 2018 (Dee et al. 2011). Climatological monthly mean for this period was calculated to represent the meteorological forcing. The wind stress $\vec{\tau}_s$ was calculated as:

$$\vec{\tau}_s = \rho_a C_D \sqrt{(u_{10}^2 + v_{10}^2)} \vec{u}_{10},$$

where u_{10} and v_{10} denote the zonal and meridional winds at a height of 10 m, respectively, and ρ_a denotes the air density. C_D is the air-ice, or air-water, drag coefficient, which has a value of 1.3×10^{-3} (i.e., the above stress definition with $C_D = 1.3 \times 10^{-3}$ is used for either case in which the sea surface is covered by ice or not). The above wind stress formula does not consider the impact of the sea surface current and ice velocity, as the 10 m wind of the winter monsoon is O(10 m/s), which is much larger than the surface current speed, which is ≤0.3 m/s. The air-ice stress drives the sea ice motion by balancing it with the ice-ocean stress, which in turn drives the ocean current. The definition of the ice-ocean stress $\vec{\tau}_{IO}$ in COCO is as follows:

$$\tau_{IOx} = \rho_0 C_W \sqrt{(u_I - u_O)^2 + (v_I - v_O)^2}[(u_I - u_O)cos\theta - (v_I - v_O)sin\theta]$$
$$\tau_{IOy} = \rho_0 C_W \sqrt{(u_I - u_O)^2 + (v_I - v_O)^2}[(v_I - v_O)cos\theta - (u_I - u_O)sin\theta]$$

where ρ_0 is a reference density, and C_W is a nondimensional water drag coefficient. u_I and v_I are the x_c and y_c components of the ice horizontal velocity, and u_O and v_O are the x_c and y_c components of the ocean horizontal velocity. (x_c, y_c) denotes the Cartesian coordinate system. θ is the rotation angle of the effective ocean flow direction when interacting with sea ice. In terms of the bottom stress, the model adopts a quadratic bottom drag parameterization (Hasumi 2000), and the bottom drag coefficient was set as

1.3×10^{-3} . We included the monthly mean freshwater flux, which included the precipitation minus the evaporation and riverine runoff data (Fig. 2.8a) reported by Dai and Trenberth (2002). The 2-meter air temperature, 10-meter wind stress, specific humidity, and long-wave and short-wave radiation provide the sea surface boundary conditions to calculate the heat flux, and these data are sourced from the ERA-Interim. Note that we did not restore the sea surface temperature and sea surface salinity to the observed values; without restoration, COCO simulated these values reasonably (e.g., Matsuda et al., 2015). The bathymetry model was obtained from the Japan Oceanographic Data Centre and included a modification reported by Ono et al. (2006).

The simulation included all the external forces as a control case (CTRL case), and additional experiments were conducted to delineate the role of the riverine discharges as follows: the simulation excluding all the riverine discharges is referred to as the 'no-River' case; the simulation including only the Amur River discharge is referred to as the 'Amur-only' case; and the simulation excluding only the Amur River discharge is referred to as the 'no-Amur' case. We executed the model for a 10-year period using data with a CTRL case configuration. Then, we adopted the tenth-year results as the initial conditions in each case for the simulation of another 10-year period to retain the same initial conditions and duration. The averaged January mean for the last five years was analysed, and the results were interpolated to the standard grids at a resolution of $1/30° \times 1/30°$.

2.2.2 Isobath coordinate

According to the approximately homogeneous w and surface divergence in the along-isobath direction, we calculated the average along the isobath to obtain a representative vertical structure of the ESC, following the definition by Stewart et al. (2019) as follows:

$$[\bullet]_h = \iint_{h_1<h<h_2} \bullet \, dA, \text{and}$$

$$\bar{\bullet}_A = \frac{[\bullet]_h}{A}.$$

Here, A is an area where the grids have a similar depth h. In this study, the depth h was selected in the COCO model from between the two closest vertical levels $[h_1, h_2]$. Thus, $\bar{\bullet}_A$ is an area averaged value inside area A between the two levels $[h_1, h_2]$. The flat shelf, which is shallower than 34 m, was considered a single isobath. The along-isobath averaged offshore distance $\bar{x}_A$ was calculated by averaging the offshore distance of each point that belongs to the same isobath within area A. We used the Haversine formula to calculate the distances between the two grids. Note that throughout the paper, we use (x, y, z) to denote the isobath coordinate.

2.2.3 Data for estimating the geostrophic stress in various coastal areas

The geostrophic stress was globally estimated as summarized in Section 2.3.6 (see equation (2-9)). The data set, which has the CMEMS (the Copernicus Marine Environment Monitoring Service) product identifier GLOBAL_MULTIYEAR_PHY_001_030, was used to estimate the global surface geostrophic current $\vec{u}_{g,s}$. The sea surface height (SSH) is obtained from a CMEMS global reanalysis product assimilating the satellite altimetry measurements. This product is defined on a standard regular grid with the horizontal resolution is $1/12° \times 1/12°$, and on 50 standard levels in the vertical direction. As a reanalyzed dataset, the NEMO (Nucleus for European Modeling of the Ocean) platform drives the model component assimilating the sea ice concentration from CERSAT (the Satellite Data Processing and Distribution Center of Ifremer, the French Research Institute for Exploitation of the Sea.). About the runoff, it includes the climatological

runoff reported by Dai et al (2009) plus the freshwater fluxes from icebergs for Greenland and Antarctica. The surface mass budget among the evaporation, precipitation and runoff is considered. One of data sets of the product named cmems_mod_glo_phy_my_0.083-climatology_P1M-m, a climatological monthly mean data within a period Jan. 1993-Dec. 2016, was used in this study. The climatological January-mean SSH above the geoid was used to obtain the surface geostrophic current for the Northern Hemisphere, whereas the August-mean SSH above the geoid was used to obtain the surface geostrophic current for the Southern Hemisphere as follows:

$$\vec{f} \times \vec{u}_{g,s} = -g\nabla\eta.$$

The SSH above the geoid was also used to define the unit direction vector for the global geostrophic stress estimation.

The ERA-Interim was used to calculate the monthly mean wind stress $\langle \tau_s^y \rangle$ and frictional velocity $u_* = \sqrt{\langle |\overrightarrow{\tau_s}| \rangle / \rho_0}$, where $\langle \bullet \rangle$ denotes the monthly mean of the six-hourly data.

The General Bathymetric Chart of the Oceans (GEBCO) _2021 grid, i.e., GEBCO's current bathymetric data set, was used to estimate the depth *h* of the coastal fronts in the regions chosen for the geostrophic stress estimation. The most recently released data set was gridded on a 15 arc-s interval grid, and furthermore, the under-ice bathymetry value obtained in Greenland was also used.

2.3 Results and discussions

2.3.1 Overview of the modelled ESC

In the winter in the Sea of Okhotsk, the northwesterly wind caused by the East Asian Monsoon (dark blue arrows in Fig. 2.1a) is primarily responsible for driving the ocean circulation, including the boundary currents and the ESC (Ohshima et al., 2002, Mizuta et al., 2003 and Nakanowatari and Ohshima 2014). Governed by a climatological January-mean wind velocity, the COCO model reproduced the two ESC cores (Fig. 2.2a); the coastal branch's depth is shallower than 50 m, whereas the WBC branch has a depth of approximately 200–500 m. The WBC branch has a density of approximately 1026 kg/m^3, and the coastal branch entrains the Amur River discharge with a density of approximately 1021 kg/m^3, covering the northern tip of the Sakhalin (Fig. 2.2a).

2.3.1.1 Two ESC cores

The near-shore core of the ESC is interpreted to be arrested trapped waves (ATWs) (Csanady, 1978; Simuzu and Ohshima, 2002; Nakanowatari and Ohshima, 2014), which mingles with a density current via the coastal river discharge. Its transport is calculated via the Ekman transport as follows:

$$V_{ATW} = \int_{l_1}^{l_2} \frac{\vec{\tau}}{\rho f} \cdot d\vec{l}$$

where $d\vec{l}$ is an integrated path, l_1 and l_2 are the start and end points of an integral path, $\vec{\tau}$ is the wind stress over the integral path, $\rho \sim 1025 \mathrm{kg/m^3}$ is the water density, and $f \sim 1.12 \times 10^{-4}\ rad/s$ is the Coriolis parameter at $50°N$.

We calculated V_{ATW} via integration of the Ekman transport $\frac{\vec{\tau}}{\rho f}$ along the integral path denoted by the dash-dotted green line in Fig. 2.3a (cf. Nakanowatari and Ohshima, 2014).

V_{ATW} was then compared with the model's simulated transport streamfunction ϕ_1 (as the coastal streamfunction was set to zero):

$$\phi_1 = \int_E^{x_c'} \int_{z=0}^{z=H} v dz dx_c$$

where v is the meridional velocity of COCO's output, E is the eastern boundary of the model domain, x_c' is any zonal position, and H is the water depth. We recall that the (x_c, y_c) denotes the Cartesian coordinate, and this notation is used throughout the paper. The streamfunction ϕ_1 is denoted by the shading and the black contour in Fig. 2.3a.

Fig. 2.3b presents a comparison between V_{ATW} and ϕ_1 at the grid points closest to the 200 m bathymetry along the Sakhalin coast. Since V_{ATW} and ϕ_1 match well along the East Sakhalin (Fig. 2.3b), the near-shore transport simulated by COCO can be explained as the integral of the Ekman flux along the northern and western coasts of the Sea of Okhotsk. It corresponds well with previous studies, e.g., Simizu and Ohshima (2002, Fig.10). An observed transport at the shallow shelf along Sakhalin Island, shallower than 200m of depth, was estimated to be 0.8~1.4 Sv by drifter measurements (Ohshima et al., 2002). V_{ATW} estimated by wind and the transport ϕ_1 simulated as in Fig. 2.3b are smaller than the estimation by the drifters. We note, however, that the surface current speed (~0.3 m/s) is similar between the simulation and the drifter measurement, and hence, the larger transport estimation by the drifters could be derived from its assumption that the velocity is uniform vertically.

The streamfunction ϕ_1 also depicts the offshore core of the ESC over the slope as the WBC of the cyclonic gyre in the central basin (Fig. 2.3a). For comparison, we calculated

streamfunction ϕ_2 based on the Sverdrup relation (Ohshima et al., 2004) with the data used by COCO as follows:

$$\phi_2 = -\frac{1}{\beta\rho}\int_{x_e}^{x_c'} \nabla \times \vec{\tau}\, dx_c$$

where $\beta \sim 1.47 \times 10^{-11}$ is the y_c derivative of the Coriolis parameter f, $x_e \rightarrow x_c'$ is the zonal integral path from the eastern boundary (deeper than 500m) to position x_c', and $\vec{\tau}$ is the January-mean wind stress of the ERA-interim (see subsection 2.2.1 for details regarding the data).

The Sverdrup transport ϕ_2 depicts the cyclonic gyre accompanying the WBC (the figure is not shown). The transport of WBC by ϕ_2 is estimated to be ~5 Sv. The value is similar to that calculated by Ohshima et al. (2004) and is comparable with the maximum transport value by ϕ_1 calculated from COCO's output (Fig. 2.3a), which implies that the WBC core of the ESC in the model is consistent with the linear Sverdrup relation. A mooring observation over the slope in the ESC upstream (Mizuta et al., 2003) evaluated the transport to be ~10 Sv in January, which is larger than the transport of WBC by ϕ_2. The difference could be related to the WBC's nonlinearity or the interannual variations discussed in Ohshima et al. (2004).

These results imply that the along-shore dynamics of the ESC in COCO's simulation are consistent with the dynamics in previous studies, and the model results are valuable for the further study of the cross-shelf dynamics.

2.3.1.2 Along-isobath averaged section of the ESC

To obtain insights into the vertical structure of the upstream ESC, we averaged the variables along the isobaths (range: 34–314 m) from 53.0°N to 53.5°N inside the area marked with yellow–green dots in Fig. 2.2a. Hereafter, 'along-isobath averaged' represents the notation:

$$\bar{\bullet}_A.$$

As defined in Section 2.2.2 (ref. Stewart et al. 2019); for example, a profile of the 'along-isobath averaged' density is denoted by $\bar{\rho}_A$.

The variables $\bar{\rho}_A$ and $\bar{v}_A$ are described in Fig. 2.2b, where v is the along-isobath current. The cross- and along-isobath components (u, v) of the velocity vector $\vec{u}$ are denoted by:

$$u = \vec{u} \cdot \hat{x},\ v = \vec{u} \cdot \hat{y}$$

and

$$\hat{y} = \hat{z} \times \hat{x},$$

Where $\hat{x}$, $\hat{y}$ and $\hat{z}$ are the normal (positive in the offshore direction), tangential and vertical unit vectors of the isobath coordinate (x, y, z), obeying the right-hand rule. The southward along-isobath current v (direction: toward the reader, Fig. 2.2b), which is predominantly geostrophic, indicates two cores of the ESC, which is similar to the real system. These cores are separated by a front with a horizontal density gradient, and the frontal isopycnal range is from 1025.2 kg/m^3 at $\bar{x}_A = 20$ km to 1025.9 kg/m^3 at $\bar{x}_A = 40$ km, where $\bar{x}_A$ denotes the along-isobath averaged offshore distance.

The front originates from the northern shelf of the Sea of Okhotsk and separates the coast into three portions, i.e., a flat shelf ($\bar{x}_A \leq 20$ km), a gently sloping shelf (20 km $\leq \bar{x}_A \leq 40$

km) and the open ocean ($\bar{x}_A \geq 40$ km). The shelf break located at $\bar{x}_A \sim 40$ km is our focus in the subsequent analysis. Inside the front between the two ESC cores (20 km $\leq \bar{x}_A \leq$ 40 km), we observed a slow $\bar{v}_A$ with a minimum current at the bottom ($\bar{x}_A \sim 30$ km). Although this frontal current is slow, the current has a surface intensified structure and exhibits baroclinicity with a typical value of $\partial v/\partial z \sim -1.0 \times 10^{-3} \mathrm{s}^{-1}$. Note that the flat shelf topography ($\bar{x}_A \leq 20$ km) was constructed according to the requirement dictated by COCO's settings. Therefore, in the subsequent analysis and discussion, we primarily focus on the formation of overturning over the gently sloping shelf and the deep mixed layer at the shelf break.

On the front's offshore boundary, there is a region with an MLD >120 m between the isobaths at 100 and 200 m (Fig. 2.2c); the MLD is obtained from the water depth where the density increases by 0.125 kg/m^3 (Kanna et al. 2018; Suga et al. 2004; Levitus 1982) compared to that of the surface density. The MLD value at the shelf break ($\bar{x}_A \sim 40$ km) is larger than that in the open ocean by approximately 50 m; in the open ocean, the mixed-layer base is characterized by an isopycnal surface of 1026.0 kg/m^3. The horizontal stratification of the mixed-layer base in the open ocean is broken at the shelf break, where a deep mixed layer is formed, and the isopycnal surface tilts to the bottom. On the inshore boundary of the gently sloping shelf at $\bar{x}_A \sim 20$ km, the stratified water is dominant again due to the Amur River discharge.

2.3.2 Vertical overturning from the flow field in the upstream ESC

To study cross-shelf overturning over the gently sloping shelf, we first examined the divergence in the surface current field at a depth of 7 m in the upstream ESC (Fig. 2.4a). Despite an almost uniform wind stress (Fig. 2.1a), we identified a surface region of divergence over the gently sloping shelf in an isobath range of approximately 50–100 m as well as a convergence region located farther offshore in an isobath range of approximately 100–200 m. The divergence coincides with an upwelling, whereas the convergence indicates a downwelling (Fig. 2.4b, simulated vertical velocity at the depth of 18m). The surface divergence/convergence and mid-depth vertical motions are nearly homogeneous in the along-isobath direction. Overall, these patterns produce a vertical overturning that entirely occupies the gently sloping shelf on the northern coast of the East Sakhalin. We also noted that there is narrow downwelling adjacent to the coast, which is shown in Fig. 2.4b and associated with the downwelling-favourable wind.

The vertical overturning over the gently sloping shelf can also be delineated using a combination of the cross-isobath current, $\bar{u}_A$, and vertical velocity, $\bar{w}_A$ (Fig. 2.5a). The upward $\bar{w}_A$ at $\bar{x}_A$~25 km and downward $\bar{w}_A$ at $\bar{x}_A$~40 km correspond to the inshore and offshore boundaries of the front over the gently sloping shelf, respectively. The inshore upward $\bar{w}_A$ at $\bar{x}_A$ ~25 km is unexpected since in the classical EOT, downwelling is generally generated under a downwelling-favourable wind condition, indicating that a reverse EOT is occurring over the gently sloping shelf. Note that the overturning over the flat shelf is not described by the analysis of the along-isobath average because one single value is obtained for each variable, e.g., $\bar{w}_A$, over the flat shelf.

The $\bar{u}_A$ pattern is consistent with the divergence information provided in Fig. 2.4a. The surface onshore flow at the flat shelf is approximately -0.07 m/s, which corresponds to a wind-induced onshore Ekman flow; in this case, as the wind stress and MLD are ~ 0.05 N/m^2 and ~ 10 m, respectively, we evaluated an onshore Ekman velocity of ~ -0.05 m/s over the flat shelf. Conversely, the surface cross-shelf flow is weak over the gently sloping shelf, which has a velocity of ~ -0.01 m/s, causing surface divergence and corresponding upwelling at $\bar{x}_A \sim 25$ km between the isobaths of 50 and 100 m. The inshore shallow mixed layer is produced by this upwelling. In contrast, the downwelling occurs farther offshore ($\bar{x}_A \gtrsim 40$ km), corresponding to the surface convergence (Fig. 2.5a). The deep mixed layer forms at a depth of 140 m, corresponding with the downwelling at the shelf break at $\bar{x}_A \sim 42$ km (Fig. 2.5b). Fig. 2.5b also shows that a small Richardson number (R_i) and a large vertical diffusivity coefficient (K_v) are obtained over the gently sloping shelf between the inshore upwelling and offshore downwelling. The mixed layer boundary envelopes K_v, which is larger than the background diffusivity (= 10^{-4} m^2/s). These characteristics over the gently sloping shelf are in contrast to the horizontally-stratified layer over the flat shelf and open ocean.

2.3.3 Vertical overturning based on stress distribution in the upstream ESC

To provide a dynamical understanding of the vertical overturning, we analysed the stress since it is a dynamical source of the ageostrophic current. The velocity can be calculated separately by:

$$\vec{u} = \vec{u}_g + \vec{u}_a,$$

where $\vec{u}_g$ and $\vec{u}_a$ denote the geostrophic and ageostrophic currents, respectively. According to the momentum equation, the ageostrophic current is described by (Chen and Chen, 2017; Cronin and Kessler, 2009; Cronin and Tozuka, 2016):

$$f\hat{z} \times \vec{u}_a = \frac{1}{\rho_0}\frac{\partial \vec{\tau}}{\partial z}, \qquad (2-1)$$

where $\vec{\tau}$ denotes the internal stress in the sea water, and f and ρ_0 denote the Coriolis parameter and a reference density, respectively. The boundary conditions are:

$$\vec{\tau} = \vec{\tau}_s, \text{ at } z = 0, \qquad (2-2a)$$

and

$$\vec{\tau} = \vec{\tau}_b, \text{ at } z = -h, \qquad (2-2b)$$

where $z = 0$ and z = $-h$ represent the sea surface and bottom, respectively, and $\vec{\tau}_s$ and $\vec{\tau}_b$ denote the wind stress and bottom stress, respectively. The internal water stress $\vec{\tau}$ is estimated as:

$$\vec{\tau} = \rho_0 A_v \frac{\partial \vec{u}}{\partial z}, \qquad (2-3a)$$

where A_v is the vertical viscosity. The along-isobath component of $\vec{\tau}$ is denoted by:

$$\tau^y(x, y, z) = \rho_0 A_v \frac{\partial v}{\partial z}. \qquad (2-3b)$$

The internal water stress $\overline{\tau^y(x,z)}_A$, derived from equation (2-3b) is depicted in Fig. 2.6a. The parameter A_v is essential for evaluating the frictional force that represents the impact of turbulence, and it reaches a magnitude of 0.04 m^2/s at the middle of the gently sloping shelf (Fig. 2.6b).

The distribution of $\tau^y(x, y, z)$ leads to an ageostrophic cross-shelf transport, as evidenced by equations (2-1) and (2-2a), such that:

$$M_e^x(x, y, z) = \int_z^0 \frac{1}{f\rho_0}\frac{\partial \tau^y}{\partial z'} dz'$$

$$= \frac{1}{f\rho_0}\left[\tau_s^y(x, y) - \tau^y(x, y, z)\right]. \qquad (2-4)$$

Therefore, the cross-shelf ageostrophic velocity u_a can be rewritten as:

$$u_a = \frac{\partial}{\partial z}\frac{\tau^y}{f\rho_0} = -\frac{\partial M_e^x}{\partial z}. \qquad (2-5a)$$

Furthermore, due to the near homogeneity of the surface divergence in the along-isobath direction (Fig. 2.4a), we may presume that the Ekman transport is independent of y. This assumption implies that M_e^x can be viewed as a streamfunction by considering $\frac{\partial u_a}{\partial x} + \frac{\partial w_a}{\partial z} = 0$ because of continuity; here, w_a is the vertical velocity derived from the ageostrophic flow. These considerations yield:

$$w_a = \frac{\partial}{\partial x}\frac{\tau^y(z)}{f\rho_0} = \frac{\partial M_e^x}{\partial x}. \qquad (2-5b)$$

The ageostrophic transport M_e^x, which is represented by equation (2-4) and derived from the surface wind stress $\overline{\tau_s^y(x)}_A$ as well as the model's generated internal water stress $\overline{\tau^y(x,z)}_A$, is depicted in Fig. 6c. The ageostrophic velocity fields u_a and w_a, which are derived from M_e^x using equations (2-5a) and (2-5b), represent a clockwise overturning structure centred at $\bar{x}_A$~30 km (Fig. 2.6d), with an upwelling nearshore side and a downwelling offshore side. This w_a (Fig. 2.6d) corresponds well with the $\overline{w}_A$ obtained from the COCO-modelled flow field (Fig. 2.5a). A reverse EOT is thus represented by M_e^x in the ESC upstream, because in a classical EOT a downwelling should be expected to occur on the nearshore side of the shelf. The maximum of $\left|\overline{\tau^y(x,z)}_A\right|$ is approximately 0.06 N/m^2 at the middle layer of the gently sloping shelf (Fig. 6a), which is larger than $\overline{\tau_s^y(x)}_A$~0.05 N/m^2. According to the aforementioned theoretical understanding, we can conclude that this maximum internal water stress, which is higher than the wind stress, primarily produces a reverse overturning (compared to the classical EOT).

Due to this clockwise (reverse) EOT, the surface flow converges at the shelf break at $\bar{x}_A$~40 km since there is a usual onshore Ekman transport in the open ocean under the downwelling-favourable wind (Fig. 2.6c); consequently, a downwelling occurs at $\bar{x}_A$~40 km (Fig. 2.6d). The deepest mixed layer is produced on the right-hand side of the

strong downwelling (see Fig. 2.6c, an MLD with a dodger line). The divergence/convergence field in COCO's simulation, which is depicted in Fig. 2.4a, corresponds well with this EOT's surface flow, which is represented by M_e^x.

In the modelled $\bar{u}_A$ (Fig. 2.5a), the surface flow tends to be directed onshore over the gently sloping shelf, although its divergence and convergence structures are robustly represented (Fig. 2.4a). This observation suggests that three-dimensional effects such as the pressure gradient could play a significant role in the simulated onshore flow. We attempted to retrieve the cross-shelf flow associated with the along-isobath pressure gradient that results in an onshore geostrophic flow, including the effects due to sea ice (see Appendix 1). However, it is known that cross-shelf geostrophic flow is one of the most difficult variables to retrieve from modelled flow fields (Stewart et al. 2019), and thus, further careful examinations are necessary. As a result, we focused on the divergent and convergent ageostrophic cross-shelf overturning retrieved from the stress distribution as well as on the vertical motion, which corresponds well with the COCO-modelled overturning.

2.3.4 Effect of geostrophic stress on the stress distribution

The cross-isobath transport from the surface to the bottom at a well-mixed layer, which is represented by M_e^x, can be divided into two parts, i.e., the surface transport and bottom transport, such that:

$$M_e^x = M_{e,s}^x + M_{e,b}^x,$$

where

$$M_{e,s}^x = \frac{1}{f\rho_0}\left[\tau_s^y - \tau^y(z)\right] \text{ and } M_{e,b}^x = \frac{1}{f\rho_0}\left[\tau^y(z) - \tau_b^y\right].$$

Here, the independent variables x and y are omitted for neatness. The expression above indicates that the maximum internal water stress, max $(\tau^y(z))$, determines the sign of $M^x_{e,s}$ and $M^x_{e,b}$. The max $(\tau^y(z))$ is depicted in Fig. 2.7a (orange line) in addition to τ^y_s and τ^y_b (the solid purple and dotted purple lines, respectively).

Defining:

$$\delta\tau = \left|\max\left(\tau^y(z)\right)\right| - \left|\tau^y_s\right|,$$

we can see that $\delta\tau$ separates the coast into three portions. For $\delta\tau < 0$, a classical Ekman frictional region is obtained in which the onshore transport occurs under the downwelling-favourable wind; this situation is similar to that on the flat shelf and in the open ocean (comparison between Fig. 2.6c and Fig. 2.7a). The surface wind stress τ^y_s is dominant over $\tau^y(z)$ because of the large Ri and small A_v over the flat shelf or because A_v approaches a background value of 1.0×10^{-4} m^2/s in the open ocean as the depth increases. In contrast, for $\delta\tau > 0$, $|\max(\tau^y(z))|$ exceeds $\left|\tau^y_s\right|$~0.05 N/m^2 across the entire layer and produces a surface offshore Ekman transport; specifically, a reverse EOT is produced over the gently sloping shelf between the offshore distances of approximately 25 and 35 km (Fig. 2.6a and c). Fig. 2.7a indicates that the locations where $\delta\tau$ changes its sign are close to the inshore and offshore boundaries of the reverse EOT. Furthermore, the bottom onshore flow over the gently sloping shelf (Fig. 2.6c and d) is considered a bottom Ekman transport because the bottom stress is much smaller than the internal water stress $\tau^y(z)$.

To understand the max($|\tau^y(z)|$) in the middle layer of the gently sloping shelf, which decides the location of the reverse EOT, we separate the along-isobath stress $\tau^y(z)$ into two parts as follows:

$$\tau^y(z) = \tau_p^y + \tau_a^y, \qquad (2-6)$$

where τ_p^y and τ_a^y denote the geostrophic and ageostrophic stresses, respectively. The former, as implied by its name, derives from the vertical shear of the geostrophic current, which is ignored in a classical Ekman solution. Cronin and Tozuka (2016) argued that the stress $\vec{\tau}(z)$ in the frontal region in a mixed layer, such as those in the Kuroshio Extension, is significantly influenced by the geostrophic stress $\vec{\tau}_p$ because of the large horizontal density gradient there.

The geostrophic stress can be evaluated using the thermal wind relation such that:

$$\tau_p^y = -A_v \frac{g}{f}\frac{\partial \rho}{\partial x}, \qquad (2-7)$$

where g is the acceleration due to gravity, and τ_p^y is depicted in Fig. 2.7b. COCO's simulation of the upstream ESC shows the importance of the geostrophic stress over the gently sloping shelf, since it is responsible for the formation of the density fronts caused by the riverine discharges around the Sea of Okhotsk. By substituting Equation (2-6) into Equation (2-1) and presuming a vertically independent τ_p^y and A_v, we obtained an analytical solution for the ageostrophic current that produces the Ekman transports under the influence of τ_p^y (see subsection 1.1.2.2). This derivation indicates that a max ($\tau^y(z)$) may arise when τ_p^y exceeds τ_s^y as schematically shown in Fig. 2.7c (right panel). In this case, the surface stress is dragged by the internal geostrophic current, resulting in the surface Ekman transport $M_{e,s}^x$ in the offshore direction.

The locations of $\left|\max\left(\tau_p^y\right)\right|$ and $|\max\left(\tau^y(z)\right)|$ are indicated in Fig. 2.7b by the dashed green and orange lines, respectively. The maximum geostrophic stress, $\max\left(\tau_p^y\right)$, is represented by a green line in Fig. 2.7a. We find that the distribution of τ_p^y is similar to that of $\tau^y(z)$, and the same is true of the relationship between $\max\left(\tau_p^y\right)$ and $\max\left(\tau^y(z)\right)$. A $\left|\max\left(\tau_p^y\right)\right|$ occurs at the middle layer of the gently sloping shelf because of the large $A_v(\geq 0.04\ \mathrm{m}^2/\mathrm{s})$, which is caused by strong mixing (see Fig. 2.5b) in conjunction with the vertical thermal wind shear $\partial v/\partial z \sim \mathrm{O}(-10^{-3})\mathrm{s}^{-1}$ shown in Fig. 2.2b over the gently sloping shelf. The results shown in Fig. 2.7a and 2.7c imply that $\left|\max\left(\tau_p^y\right)\right| > \left|\tau_s^y\right|$ is a necessary condition for $\delta\tau > 0$, which causes a reverse EOT.

2.3.5 Response of internal water stress and vertical overturning to the riverine discharge

Thermal-wind shear due to baroclinicity is conducive to the production of a substantial geostrophic stress, which results in an internal water stress that is higher than the wind stress. Additionally, the riverine freshwater flux causes the formation of a coastal front in the upstream ESC (Fig. 2.2a). Since the internal water stress plays a decisive role in the formation of the EOT structure, we performed experiments to test the sensitivity of the internal water stress and the EOT to the riverine freshwater flux.

The rivers included in COCO's simulation are marked in Fig. 2.8a. We highlighted the Amur River with a purple dot, since it causes a large flux compared to other rivers. However, its wintertime flux is small. The sensitivity experiments are also listed in Fig. 2.8a. We conducted numerical experiments using the 'no-River', 'Amur-only' and 'no-Amur' cases to contrast with the 'CTRL' case.

The vertical overturning based on the flow fields of these three sensitivity experiments (Fig. 2.8b–d) are well matched to the EOT represented by M_e^x (Fig. 2.8e–g), which was retrieved from the stress (Fig. 2.8h–j). The density structures and along-isobath currents are depicted in Fig. 2.8k–m. Interestingly, only the 'no-Amur' case could represent the deep mixed layer of ~150 m (Fig. 2.8m), which is located the farthest offshore among these three cases. This MLD and its location are similar to those in the CTRL case, indicating that the riverine discharge that originates from the eastern coast of the Sea of Okhotsk facilitates the formation of the salinity front over the gently sloping shelf as well as the deep MLD at the shelf break.

On the other hand, the Amur River discharge is not capable of featuring the deep MLD, because the Amur River discharge only contributes to an inshore front (Fig. 2.8l), which causes a considerable internal water stress adjacent to the flat shelf (Fig. 2.8i). As a result, the reverse EOT in this case is produced in a shallower layer (Fig. 2.8c and 2.8f).

The 'no-River' case exhibits a dissimilar pattern in its density structure, since no coastal front is formed (Fig. 2.8k); instead, a well-mixed layer is formed over the flat shelf. Therefore, in contrast to the other two sensitivity tests as well as the CTRL case, neither an internal water stress higher than the surface wind stress (Fig. 2.8h) nor a reverse EOT (Fig. 2.8b, e) can occur in this case. The inshore upwelling almost disappears because of the absence of the surface divergence. The downwelling found at $\bar{x}_A$~32 km is induced by blocking of the onshore Ekman transport due to the well-mixed coastal water mass over the flat shelf. The well-mixed layer and the resulting surface and bottom stress compensation (Mitchum and Clarke, 1986) concur with an intense A_v (a figure depicting

this scenario is not included in the paper). These structures are comparable to a simulated structure in the idealized model reported by Allen and Newberger (1996).

In conclusion, the reverse EOT in the CTRL case is driven by the geostrophic stress associated with the density front caused by the freshwater discharge from the far-eastern Eurasian Continent. The Amur River discharge alone cannot produce a density frontal structure that can induce a reverse EOT over the gently sloping shelf or a deep mixed layer at the shelf break in the ESC upstream, but the other riverine discharges support this process.

2.3.6 Scaling analysis of the geostrophic stress and its applicability to various frontal coastal regions

Thus far, we have demonstrated the importance of geostrophic stress in the cross-shelf flow structure in the ESC upstream. The geostrophic stress has been overlooked in the dynamics of shelf break fronts, which have a depth of O(100 m) or deeper. In related research, Moffat and Lentz (2012) discussed a similar but shallower overturning adjacent to the coast with a depth of approximately 15 m. In their estimation, τ_p is scaled roughly by $\tau_p = \rho_0 C_b {v_g}^2$, where v_g is the geostrophic velocity, and C_b is a drag coefficient with a value of 1.3×10^{-3}. Applying the same scaling to the well-mixed ESC layer, where v_g is approximately equal to 0.1m/s (Fig. 2.2a), we obtained τ_p~0.013 N/m^2, which is much smaller than τ_s^y~0.05 N/m^2. In other words, a reverse EOT is not expected in the ESC upstream by this estimation.

Here, we adopted a cubic profile for the vertical viscosity A_v (Lentz 1995; Signell et al. 1990; see Appendix 3) while scaling τ_p, where $\tau_p = \rho_0 A_v \frac{\partial v_g}{\partial z}$. Chen and Chen (2017) considered this profile and characterised A_v by its vertical average, although in their case, A_v exhibited a parabolic shape for a shallow shelf, where the surface frictional velocity was the same as the bottom frictional velocity. However, for a shelf break such as that in the upstream ESC, the bottom stress is negligible compared to the surface wind stress, because the bottom current is retarded via the thermal–wind relation. Thus, A_v exhibits a cubic profile and is characterised by its vertically averaged value as follows:

$$A_v{}^{\#} = \frac{\kappa u_* h_{mix}}{12}, \qquad (2-8)$$

where $\kappa \approx 0.4$ is the von Kármán constant, h_{mix} is the thickness of the vertical well-mixed water, and $u_* = \sqrt{\langle|\overrightarrow{\tau_s}|\rangle/\rho_0}$ is the frictional velocity. $\langle\bullet\rangle$ denotes the monthly mean of the hourly data. The superscript # denotes scaled variables and parameters.

We applied this estimation of A_v to scale $\tau_p^{y\#}$ such that:

$$\tau_p^{y\#} \sim \rho_0 \frac{\kappa u_* h_{mix}}{12} \frac{\langle v_{g,s}^y \rangle}{h}, \qquad (2-9)$$

where h is the local whole-layer depth, and $v_{g,s}^y$ denotes the surface along-isobath geostrophic velocity. A reverse overturning may occur when:

$$\left|\tau_p^{y\#}\right| \geq \left|\langle\tau_s^y\rangle\right|.$$

Notably, we used ${u_*}^2 = \langle|\overrightarrow{\tau_s}|\rangle/\rho_0 \geq \left|\langle\tau_s^y\rangle\right|/\rho_0$ when estimating $\tau_p^{y\#}$, since $\langle|\overrightarrow{\tau_s}|\rangle$ is based on the monthly mean absolute wind stress $|\overrightarrow{\tau_s}|$ ($\left|\langle\tau_s^y\rangle\right|$ is the absolute value of the monthly mean of τ_s^y that includes both positive and negative values). If we rewrite $\langle|\overrightarrow{\tau_s}|\rangle/\rho_0 = \alpha\left|\langle\tau_s^y\rangle\right|/\rho_0$, then the factor α represents the stability of the wind direction; this factor becomes $\alpha \sim 1$ when the wind blows stably in the along-isobath direction as it does in the

ESC upstream, where the northwesterly wind along the coast blows most of the time during the winter. In contrast, if the wind has a large variability but a small monthly mean, it corresponds to a large α; the Gulf of Alaska is one example of this case.

Considering the well-mixed ESC layer, where $\langle \tau_s^y \rangle \sim -0.05$ N/m^2, $\alpha \sim 1.484$, and using $u_* \sim 0.0085$ m/s, we obtain:

$$A_v{}^{\#} = \frac{\kappa u_* h_{mix}}{12} \sim 0.028 \text{m}^2/\text{s},$$

if the mixed layer depth h_{mix} is scaled to 100 m. The magnitude of the estimated $A_v{}^{\#}$ is consistent with the simulated A_v after performing a vertical average, which means that $v_{g,s}^y \sim 0.18$m/s is a typical velocity in conditions under which τ_p^y is significant compared to the surface wind stress. Since the surface geostrophic current $v_{g,s}^y$ in COCO's simulation is approximately 0.19 m/s (Fig. 2.2b), the estimation obtained using Equation (2-9) implies that the reverse EOT may occur over the ESC shelf break, where $h \sim 100$ m. This estimation is consistent with that obtained by COCO's simulation.

A buoyancy-driven geostrophic flow with a vertical shear of $O(-10^{-3})$ s^{-1} in addition to a downwelling-favourable wind is not peculiar to the ESC; it is common to the various shelf break fronts such as those in the Gulf of Alaska (Stabeno et al. 2004). The estimation of τ_p^y obtained using Equation (2-9) is further considered so that it may be applied to various coastal frontal regions under controlled downwelling-favourable wind and a strong coastal current.

The COCO-simulated geostrophic stress τ_p^y in areas A3, A4 and A5 as shown in Fig. 9a is compared with the estimated $\tau_p^{y\#}$ (Fig. 2.9b). To estimate $\tau_p^{y\#}$, we used data from the

CMEMS to evaluate the geostrophic surface current from the SSH above the geoid (see Section 2.2.3). Here, the along-isobath direction is determined by the SSH instead of the isobaths, since in a coastal region with a complex terrain and multiple extremes, the along-isobath unit vectors exhibit a complicated and unstable direction. The MLD is scaled by $h_{mix} = 100$ m, because the shelf break fronts were considered at depths of ~100 m. The positions for the scaling estimation, which we chose randomly along the front, are represented as numbered dots in Fig. 9a. In Fig. 9b, we observe that the coloured dots are gathered around the line $\tau_p^y = \tau_p^{y\#}$, indicating that τ_p^y scales well with $\tau_p^{y\#}$, with their root mean square difference being 0.0226 N/m^2.

We used the SSH of the CMEMS reanalysis to estimate $v_{g,s}^y$ because there are almost no observations available in high latitude coastal regions in winter. We should note that there are some potential defects included in the SSH. The first is the sea ice coverage near the ESC in winter, which makes SSH measurement by satellite impossible. Therefore, the estimated SSH by the CMEMS reanalysis product may also include errors for the area near the ESC in January because of the absence of satellite SSH data. However, the results are still considered as a reasonable estimation in the reanalysis because it includes appropriate physical processes such as riverine discharge and sea ice (see subsection 2.2.2.3), and has an enough resolution ($1/12° \times 1/12°$) for the generation of the ATW (e.g., Simizu and Ohshima, 2002). The second potential defect is that the input satellite SSH data from the coastal areas might be contaminated by the land. The first factor may explain why the estimated $\tau_p^{y\#}$ does not correspond well to the simulated values in the A3 area around the ESC. On the other hand, $\tau_p^{y\#}$ is close to the simulated values τ_p^y in the A4 (East Kamchatka) and A5 (Gulf of Alaska) areas, as there is no sea ice coverage.

This analysis motivated us to evaluate the geostrophic stress in other coastal regions, since it may elucidate the potential dynamical importance of the geostrophic stress. We selected six representative coastal regions (A1–A6 in Fig. 2.9a). Figure 2.9a depicts $\tau_p^{y\#}$ and implies that the geostrophic stress has significant values in various coastal regions. Figure 2.9c compares $\tau_p^{y\#}$ in terms of the surface wind stress $\langle \tau_s^y \rangle$ to all of the selected coastal positions. In Fig. 2.9c, the coloured dots tend to concentrate in the shaded quadrants, implying that $\tau_p^{y\#}$ and $\langle \tau_s^y \rangle$ have the same direction. In the yellow-shaded region, where $\left|\tau_p^{y\#}\right| > \left|\langle \tau_s^y \rangle\right|$, the EOT may be reversed by a higher internal water stress. In the pink-shaded region, where $\left|\tau_p^{y\#}\right| \leq \left|\langle \tau_s^y \rangle\right|$, a usual EOT is generated while also being retarded by the internal water stress.

This scaling implies that the geostrophic stress may be significant for various coastal areas, although detailed studies should be conducted in each region due to the errors that may have influenced the observed SSH values. Areas such as the upstream ESC, East Kamchatka Current, Labrador Current, Gulf of Alaska and Falkland Current are candidate areas where the reverse EOT could be generated (Fig. 2.9c). For areas with sea ice coverage that are not as dense as the coast of ESC (e.g., the Labrador Current), the air-sea heat flux cannot be neglected when discussing the mixed layer's formation. For the area around the East Greenland Current, a very deep frontal structure at the shelf break exists, and as a result, the small ratio between the MLD and the whole layer depth largely makes the estimated geostrophic stress smaller. The estimation represented by Equation (2-9) suggests that the geostrophic stress should not be overlooked when evaluating the EOT structures in coastal fronts with depth scales of O(100)m, where cross-shelf overturning

is responsible for nutrient entrainment and water exchange between the open ocean and the coastal region.

2.4 Summary

In this study, we used an Ocean General Circulation Model, IcedCOCO, to establish a realistic regional simulation to determine the formation of the winter deep mixed layer around the shelf break in the Sea of Okhotsk. During the winter, sea ice makes observation difficult. The model results, which simulated the two cores of the East Sakhalin Current and the density fronts over the gently sloping shelf, are instructive in terms of understanding the cross-shelf overturning circulation over the Sakhalin shelf. The density fronts are produced by riverine discharges around the Sea of Okhotsk. The vertical shear due to the thermal wind in the fronts, combined with a significantly large vertical viscosity, generates a large stress in the water column; this stress is known as "geostrophic stress". A reverse overturning is induced by the larger geostrophic stress than the surface stress, with respect to the classical Ekman overturning, and the reverse overturning incorporates a nearshore upwelling and an offshore downwelling. A deep mixed layer forms with a depth of ~120m in the downwelling region, where a reverse Ekman transport converges with an onshore Ekman transport from the open ocean; this mixed layer is deeper than the open ocean mixed layer, which has a depth of ~50m. Scaling analyses indicate that this mechanism might be applicable to various other shelf break fronts in the world's oceans.

The overturning over the gently sloping shelf, which we examined in this study, is located between a shallow area, where the water straightforwardly responds to the applied stress with a comparable surface and bottom stress, and a deep area where the depth of

the surface boundary layer is far smaller than the whole layer's depth. Lentz (1995) defined such a coastal transition region as the inner shelf. He examined the inner-shelf circulation in a homogeneous ocean and found that the overturning on the inner shelf is sensitive to vertical viscosity forms. In this paper, we found that stratification further modifies cross-shelf overturning via the geostrophic stress, which directly depends on the vertical viscosity. Although a study by Lentz (1995) provided us with insight into how barotropic water responds to various vertical viscosity profiles in the inner shelf, the effects in conjunction with stratification are still an open question. Spall and Thomas (2016) studied restratification/destratification processes in the presence of baroclinic instability from the perspective of potential vorticity and buoyancy budgets with balances among wind stress, geostrophic stress and vertical mixing. They primarily examined cases with strong wind and strong stratification in which baroclinic eddies are dominant. However, density fronts over inner shelf regions are often much weaker, including those in the ESC, where the baroclinic instability may not be dominant or is at most comparable to the effects of geostrophic stress.

Some interesting research targets remain. One target involves the coastal Ekman layer responses to high-frequency variations caused by short-term strong wind events or tidal forcing; in this research, we primarily studied a coastal Ekman layer in a steady state. These effects are likely to cause larger geostrophic stress as well as larger surface and bottom stresses by generating viscosities larger than those of the monthly-mean forcing. For example, diurnal tides are strong in the ESC region (e.g., Ohshima et al., 2002; Mizuta et al., 2003), and they likely cause intensive bottom currents and increase the bottom stress and vertical viscosity in the bottom boundary layer. These events may significantly influence the cross-shelf overturning and transport. Another related issue involves

determining why a large viscosity occurs at the inner shelf; the answer to this question is important in terms of generating large geostrophic stresses. Furthermore, comparing the simulated cross-shelf and vertical velocity with the observations would be insightful, although obtaining the related data from observations is difficult considering that these variables only have small values. In the case of the East Sakhalin, it is even harder to obtain data during the winter because of the sea ice coverage. Additionally, the effects of sea ice on cross-shelf overturning have not been well examined either.

Appendix

Appendix 1

Retrieved cross-isobath geostrophic flow from the modelled flow field

The ageostrophic overturning (Fig. 2.6d) is not able to completely reproduce the onshore cross-isobath current (Fig.2.5a) with a comparison of these results. Subsequently, we further calculated the geostrophic component of the cross-isobath current, u_g, which is derived from:

$$f u_g = -\frac{1}{\rho_0}\frac{\partial p}{\partial y},$$

where y denotes the along-isobath coordinate, p denotes the pressure, ρ_0 ~1023.6 kg/ m^3 is the reference density of the sea water, and f is the Coriolis parameter.

The hydrostatic approximation is as follows:

$$\frac{\partial p}{\partial z} = -\bar{\rho} g$$

where $\bar{\rho}$ denotes the density, including both the water density $\rho(z)$ and the constant sea ice density ρ_I. g is the acceleration due to gravity. Vertical integration of the hydrostatic approximation in a unit area yields:

$$p(z) = -\int_{\eta_I}^{\eta} A_I \rho_I g \, dz' - \int_{\eta}^{z} \rho \, g dz',$$

where η_I is the ice-surface elevation, η is the sea surface elevation, and A_I is the ice concentration. After taking the derivative of p in terms of y and combining it with the geostrophic relation, we obtain:

$$u_g = \underbrace{-A_I \frac{g}{f}\frac{\rho_I}{\rho_0}\frac{\partial h_I}{\partial y}}_{u_g^1} \underbrace{-\frac{g}{f}\frac{\rho(\eta)}{\rho_0}\frac{\partial \eta}{\partial y}}_{u_g^2} \underbrace{-\frac{g}{f}\int_z^{\eta}\frac{\partial}{\partial y}\left(\frac{\rho-\rho_0}{\rho_0}\right) dz}_{u_g^3}',$$

where $h_I$is the ice thickness, and $\rho(\eta)$ is the density of the surface water, which is $\sim\rho_0$. The geostrophic cross-isobath current includes a total of three components with a contribution from the sea ice thickness (u_g^1), sea surface height (u_g^2), and baroclinicity (u_g^3) (Fig. A2.1). The contribution from the sea ice provides a significant onshore current, which is considered the reason for the onshore cross-isobath current in Fig. 5a. The cross-isobath current due to baroclinicity is dominant on the flat shelf with an offshore direction and vertical gradient deriving from the thermal wind relation. u_g^3 is a partial offset to the onshore cross-isobath current.

Appendix 2

Vertical averaged cubic eddy viscosity

The cubic profile of A_v creates an asymptote to a linear profile near the surface and bottom boundaries. The eddy viscosity profile of the form $A_v = \kappa u_* z$ can effectively simulate a logarithmic velocity profile adjacent to the sea surface and bottom boundaries; then, a constant stress flux forms in the simulation, which corresponds to observations. Lentz (1995) tested coastal region responses to various eddy viscosity profiles, including constant, bilinear-cutoff, bilinear, and cubic profiles. All of them (except for the constant A_v) performed well at the boundary layers because of the linear A_v there, and slight differences occurred in the cubic profile's interior water, since that profile performed better on the cross-shelf current. Cubic-like vertical eddy viscosities were also simulated with the turbulence closure model in COCO as denoted in Figure A2.2.

To conduct the estimation, a cubic profile was adopted to delineate A_v such that (modified from Signell et al. 1990):

$$A_v(z) = -\kappa u_{*,s} z + \frac{\kappa(u_{*,b} - 2u_{*,s})}{h_{mix}} z^2 + \frac{\kappa(u_{*,b} - u_{*,s})}{{h_{mix}}^2} z^3 ,$$

where $\kappa \approx 0.4$ is the von Kármán constant, and h_{mix} is the thickness of the vertical well-mixed water. Further, $u_{*,s}$ and $u_{*,b}$ are the surface and bottom frictional velocities, respectively. When $u_{*,b} \sim u_{*,s}$ for a shallow shelf, A_v exhibits a parabolic shape, which is parameterized as:

$$A_v(z) = -\kappa u_{*,s} z - \frac{\kappa u_{*,s}}{h_{mix}} z^2.$$

This expression reproduces the vertical average of $A_v(z)$, i.e., ${A_v}^{\#} = \frac{\kappa u_{*,s} h_{mix}}{6}$, which was reported by Chen and Chen (2017).

In our case, assuming $u_{*,b} \sim 0$ for a deep shelf break, we obtain:

$$A_v(z) = -\kappa u_{*,s} z - 2\frac{\kappa u_{*,s}}{h_{mix}} z^2 - \frac{\kappa u_{*,s}}{{h_{mix}}^2} z^3,$$

and thus, ${A_v}^{\#} = \frac{\kappa u_{*,s} h_{mix}}{12}$ (Equation (2-8) in the text) is its vertical average.

Appendix 3

IcedCOCO boundary conditions configuration

A.IcedCOCO boundary file with ERA-Interim data

Original data:

ERA-Interim netCDF data

Grid:0.75*0.75

Area: default global data

Data_period (typical year): 2014.1.1.-2015.12.31

Data_period (long years): 1979.06.01-2019.05.31

一 · monthly mean:

1. analysis data

TAUX 10 metre U wind stress component (Pa)

TAUY 10 metre V wind stress component (Pa)

$$taux = \rho_{air} C_D \sqrt{u^2 + v^2} u$$

$$tauy = \rho_{air} C_D \sqrt{u^2 + v^2} v$$

$$\rho_{air} = \frac{1.23kg}{m^3} \quad C_D = 1.2e-3$$

USFC scalar wind speed, which should be calculated from 10 meter wind speed (m/s)

sqrt(U10m*U10m+V10m*V10m)

TSFC 2 metre temperature (K)

QSFC specific humidity (nondimensional)

0.62197*(6.1121*exp((18.729-(d2m-273.15)/227.3)*(d2m-273.15)/((d2m-273.15)+257.87)))/(msl.2/100-0.378*(6.1121*exp((18.729-(d2m-273.15)/227.3)*(d2m-273.15)/((d2m-273.15)+257.87))))

PSFC Mean sea level pressure (Pa)

6-hourly data: (00:00+06:00+12:00+18:00)/4

2. forecast data

DWLW surface thermal radiation downwards (W/m^2)

SWNT surface net solar radiation data (W/m^2)

12-hourly data>> per second (00:00+12:00)/2

unit transfer: please insure that the integrated unit J/m^2*12hr must be changed to temporal averaged unit (W/m^2) by dividing it in 12*60*60

3.

I write these daily-mean data with binary format and text format., and interpolated into the COCO's grid.

Figures

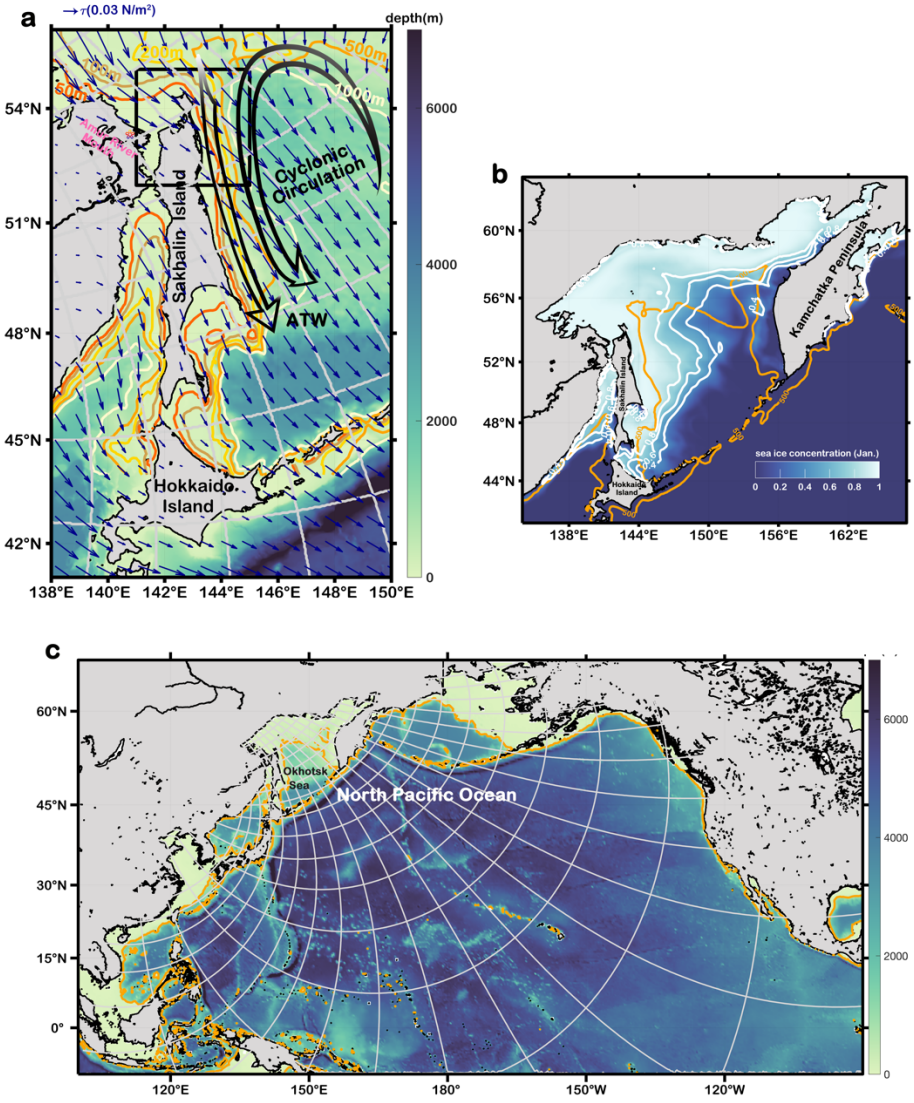

Figure 2.1: Outline of the model setting and an unprocessed model output

a Schematic diagram of the research domain—the Sea of Okhotsk. The black arrows indicate the two ESC cores. The Amur River mouth, which is marked by a petal-like sign, belongs to the river with the largest discharge in the research domain. The area inside the black frame represents the ESC upstream, and we present the horizontal information for this area in the subsequent analysis. The shading and orange contours denote the topography. The blue arrows denote the climatological January-mean wind stress. **b** The January mean sea ice concentration for the CTRL case. The coloured shading and white

contour denote the sea ice concentration. The coloured contour is the isobath with a depth of 500m. **c** Model domain northern than 10°S**.** The shading denotes the topography**.** The orange contour is the 500-meter isobath. The light grey contours represent COCO's Mercator grid at every 50 and 30 grid intervals in approximately the N-S and W-E directions, respectively, which is the same as in **a**.

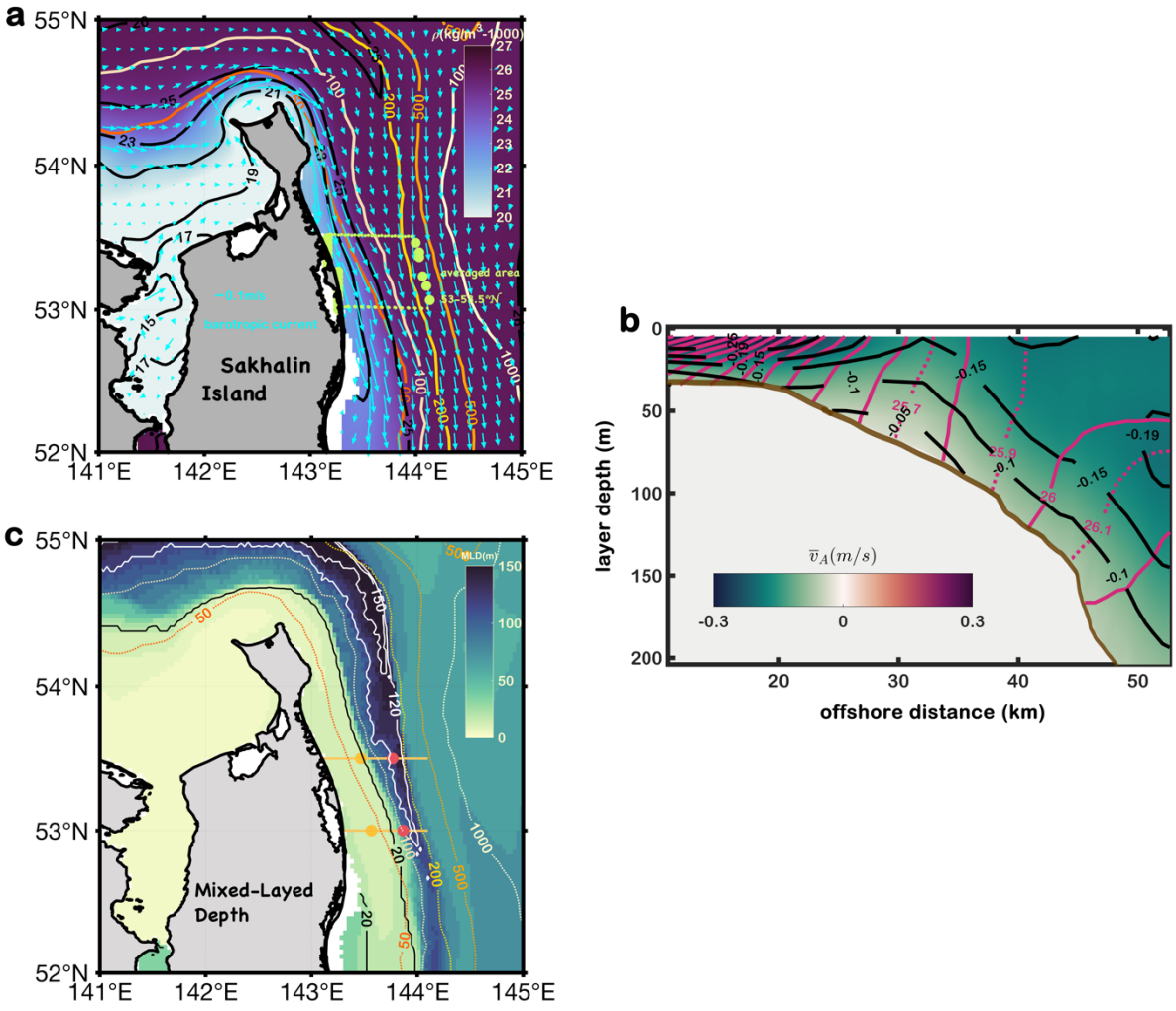

Figure 2.2: Overview of the upstream ESC

a The light-blue arrows denote the climatological January-mean depth-averaged velocity (as the barotropic current). The black contours denote the climatological January-mean surface density, and the orange contours denote the topography. The yellow-green dotted box indicates the area for which the along-isobath average was processed (see Section 2.2; along-isobath averaged: as $\overline{\bullet}_A$). **b** The shading and black contours denote the along-isobath currents. The negative values indicate the southward currents, which are directed towards the reader. The solid and dashed magenta contours denote densities; the former has values from 1023.2 to 1026.2 kg/m^3 at 0.2 kg/m^3 intervals without labels except for the contour at 1026.0 kg/m^3. The x-axis represents the offshore distance (see

Section 2.2). **c** The shading and solid contours denote the MLD, and the dotted orange contours denote the topography. The orange and red dots denote offshore distances of approximately 20km and 40km, respectively, along the 53°N and 53.5°N latitudes.

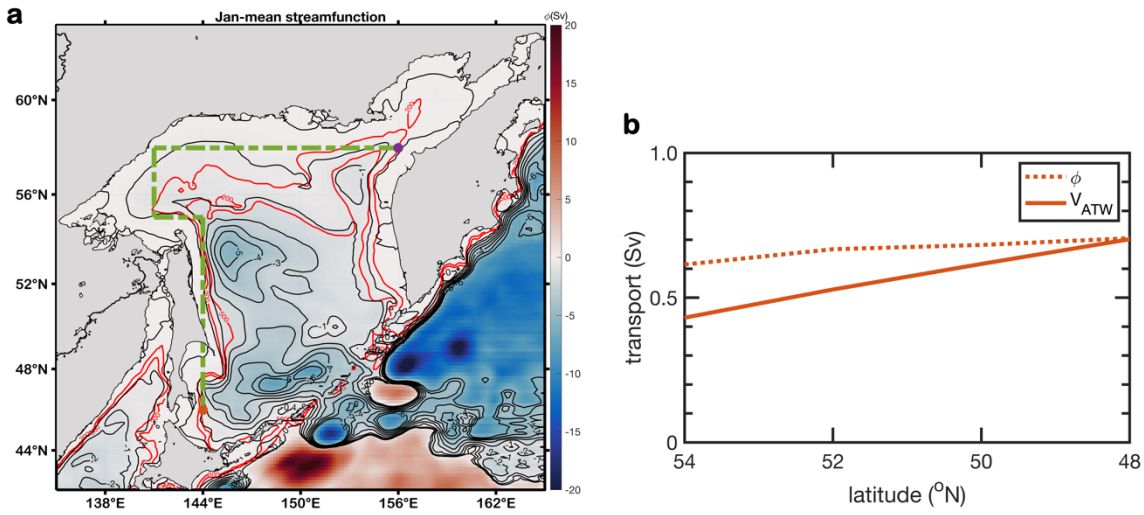

Figure 2.3: Two cores of the ESC

a The shading and the black contour denote the streamfunction ϕ_1, which was calculated via meridional velocity integration. The red contour denotes the isobath at 200m and 500m. The dash-dotted green line is the integral path used to calculate the transport according to arrested topographic waves. The purple/red dots are the start/end of the integrated points. **b** Transport comparison between V_{ATW} and ϕ_1 at the latitudes 48°N, 50°N, 52°N and 54°N. For ϕ_1, we chose the points with depths of 255 m, 228m, 212 m, and 197 m for each latitude.

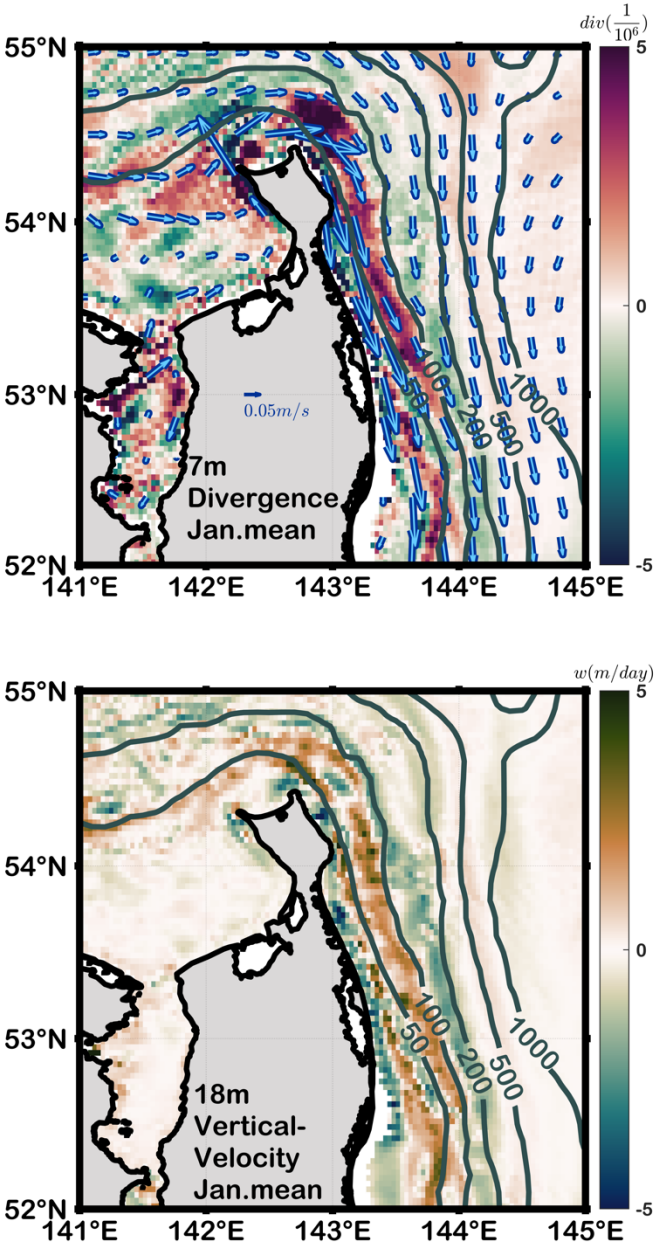

Figure 2.4: Surface divergence/convergence field and vertical motion in the upstream ESC

a The shading denotes the climatological January-mean horizontal velocity divergence at a depth of 7 m. The positive values with red shading represent the horizontal velocity divergence., and the negative values with green shading represent the horizontal velocity convergence. The vectors denote the horizontal velocity at the same depth, and the dark

green contours denote the topography. **b** The shading denotes the vertical velocity at a depth of 18 m, where the positive values represent the upward vertical velocity using the reddish-brown shading. The dark green contours denote the topography.

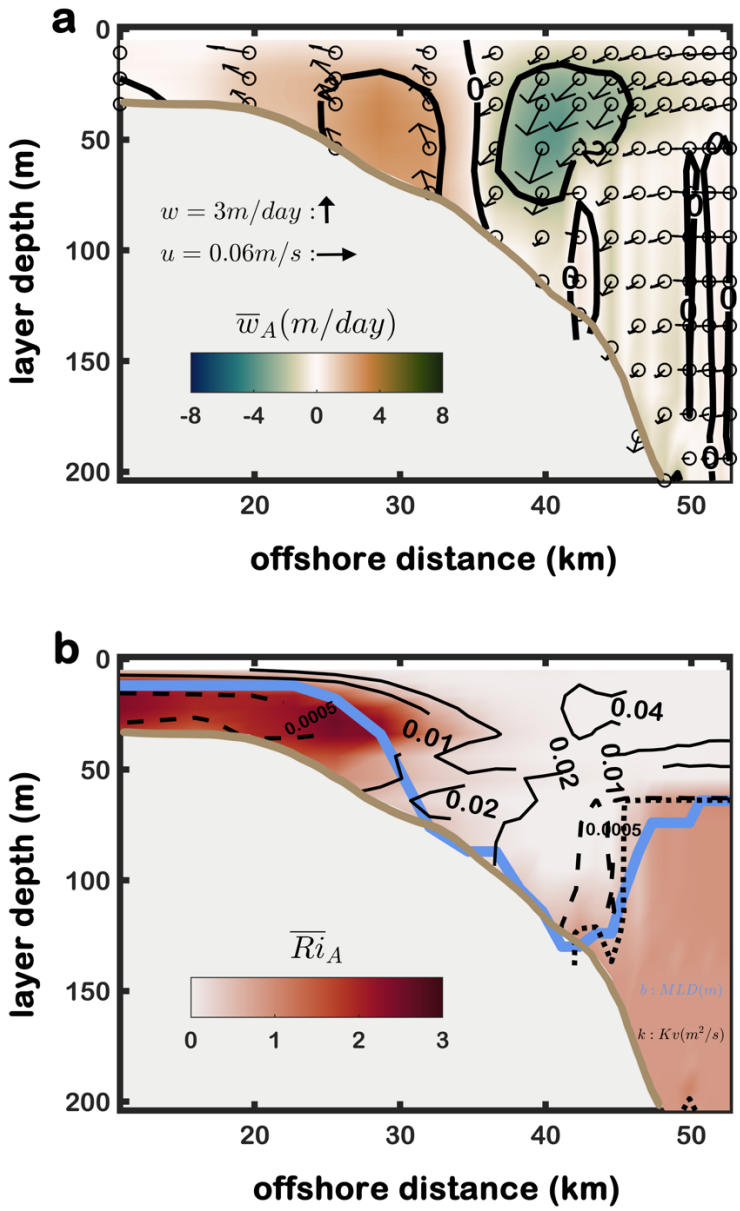

Figure 2.5: Coherence of the vertical overturning and mixed layer deepening

a The shading and black contours denote the vertical velocity. The arrows are the combination of the cross-isobath current and vertical velocity, and the circles denote the start point of each arrow. **b** The shading denotes the January-mean Richardson Number, $Ri = \frac{N^2}{(\frac{\partial u}{\partial z})^2+(\frac{\partial v}{\partial z})^2}$, where N is the Brunt–Vaisala frequency. The black contours denote the vertical diffusivity K_v, and the dotted line denotes K_v = 0.0001 m^2/s, which is close to the

background vertical diffusivity. the dashed line denotes K_v = 0.0005 m^2/s, which is dominant on the flat shelf. The dodger blue line denotes the MLD.

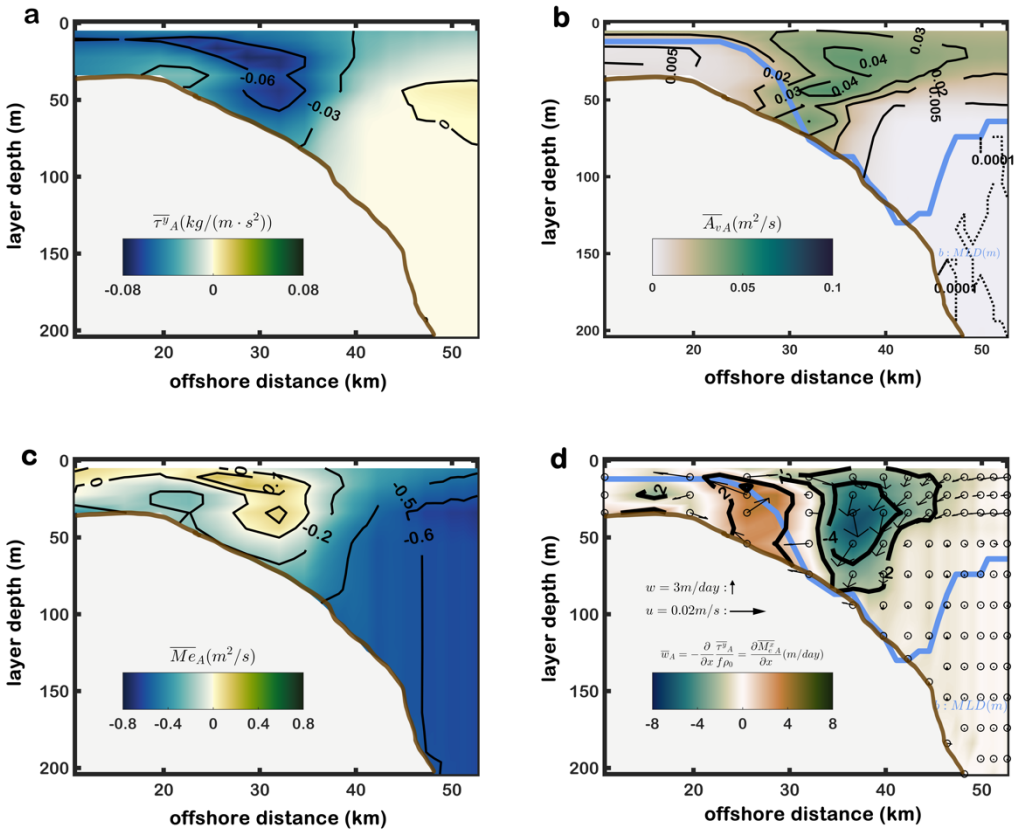

Figure 2.6: Ageostrophic vertical overturning derived from the stress distribution

a The shading and black contours denote the along-isobath internal water stress. The negative values indicate the southward internal water stress and are directed toward the reader. **b** The shading and black contours denote the vertical turbulent viscosity *Av*. The dodger blue line denotes the MLD, and the dotted line represents A_v = 0.0001 m^2/s. **c** The shading and black contours denote the cross-isobath Ekman transport M_e^x, which is derived from the stress distribution. **d** The shading and black contours denote the derived vertical velocity. The arrows represent the information of the coupled vertical velocity and the ageostrophic cross-isobath current, both of which are retrieved from the cross-shelf Ekman transport M_e^x. The dodger blue line denotes the MLD, and Fig. 6d is a theoretical analogue to Fig. 5a.

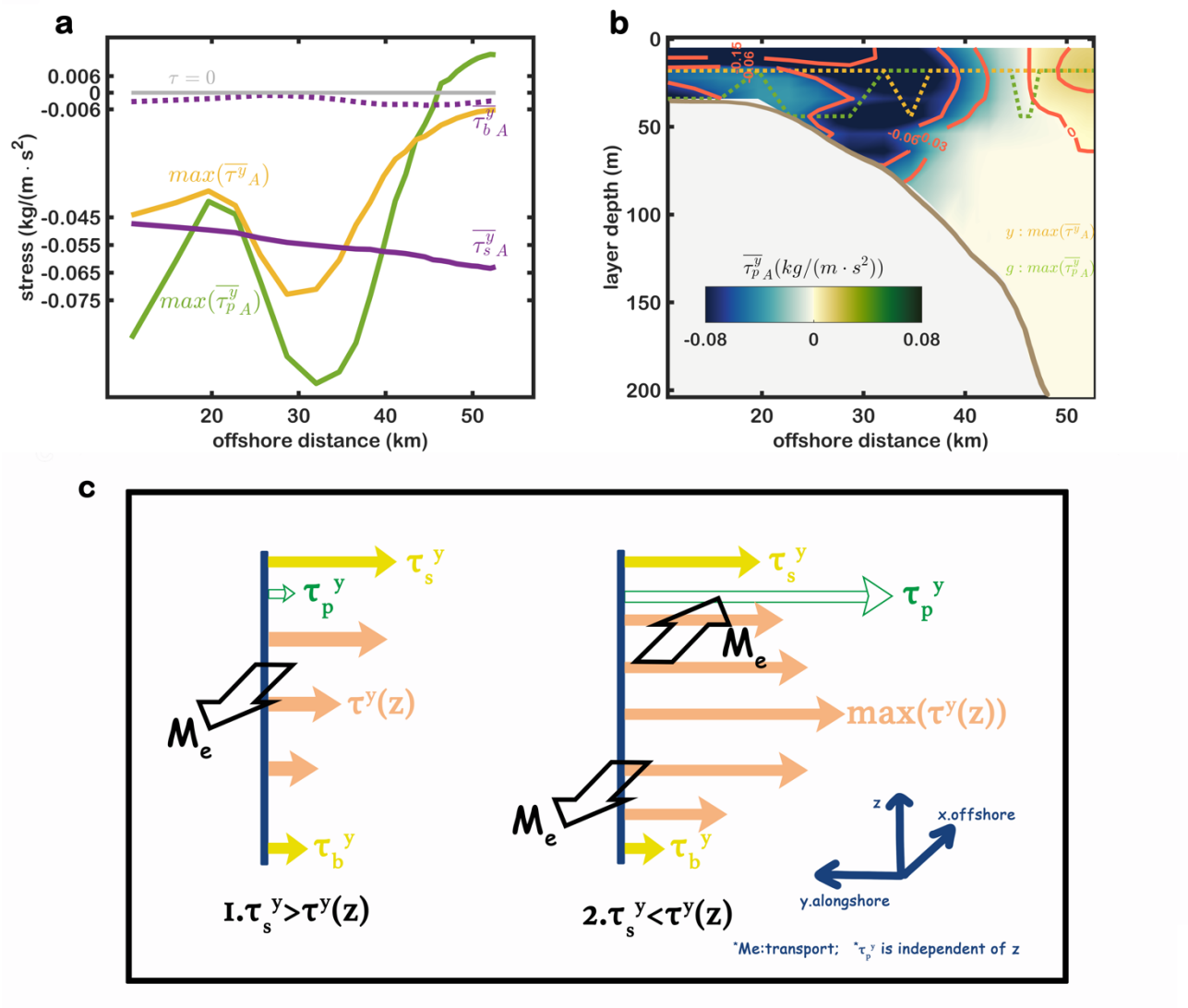

Figure 2.7: Role of geostrophic stress on the vertical overturning

a Various along-isobath stresses are depicted. The surface wind stress is marked by the solid purple line, and the bottom stress is depicted by the dashed purple line. The orange line denotes the maximum internal stress below a depth of 14 m, while the green line denotes the maximum geostrophic stress. The grey line denotes zero stress. The negative sign denotes the southward direction, and the s-axis denotes the offshore distance. **b** The shading and red contours denote the geostrophic stress. The dotted yellow line indicates the depths of the maximum internal stress in terms of distance, and the dotted green line indicates the depths of the maximum geostrophic stress. **c** The schematic patterns

represent the relativity among the surface, bottom, and internal stresses in the Ekman transport. The role of geostrophic stress in modifying the internal stress is discussed in the text. The reference coordinate system is shown in the right-bottom corner.

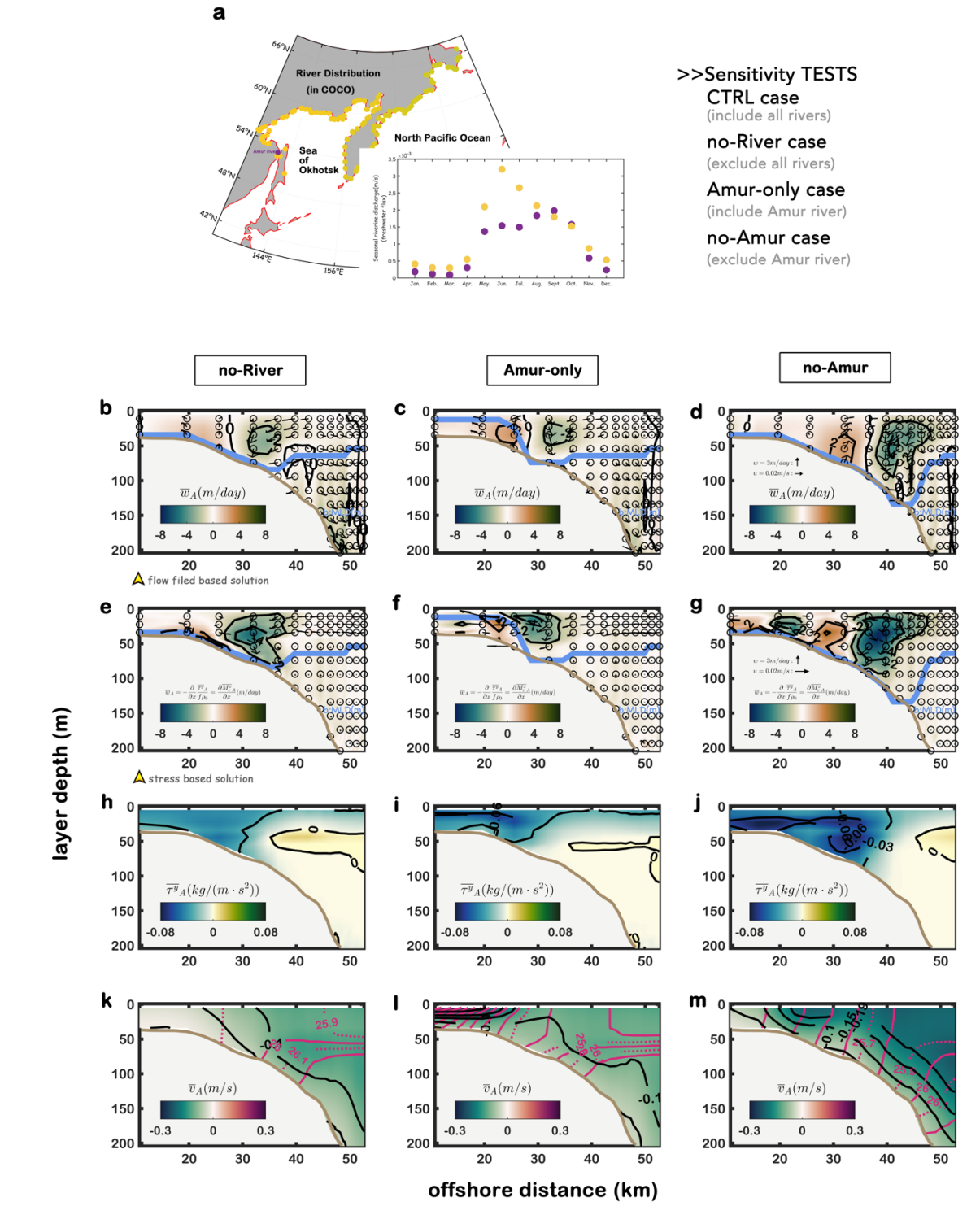

Figure 2.8: Sensitivity tests: Impact of the freshwater discharge from the Eurasian Continents on the vertical overturning

a The purple and yellowish dots on the map denote the river's distribution as defined in the COCO simulation. The purple and yellowish dots in the panel in the right-bottom

corner denote the seasonal Amur river and the other river discharges, respectively. **b–d** Vertical overturning from the modelled flow field. Each column from left to right represents the results for the no-River case, Amur-only case, and no-Amur case. The shading and black contours denote the vertical velocity, and the arrows denote the combination of the vertical and ageostrophic velocity. The bold dodger line represents the MLD. **e–g** The same colours and symbols as **b–d** but for the vertical overturning retrieved from the stress distribution. **h–j** The internal stress of each sensitivity test (shading and contours). The internal stress values of [0, -0.03, -0.06] are labelled. **k–m** The density sections (shading and purple contours) and along-isobath currents (solid black contours) of the sensitivity tests. Negative along-isobath current values denote southward toward the reader. The purple contours represent isopycnals at intervals of 0.2 and 0.1 kg/m^2 (the solid and dashed lines, respectively).

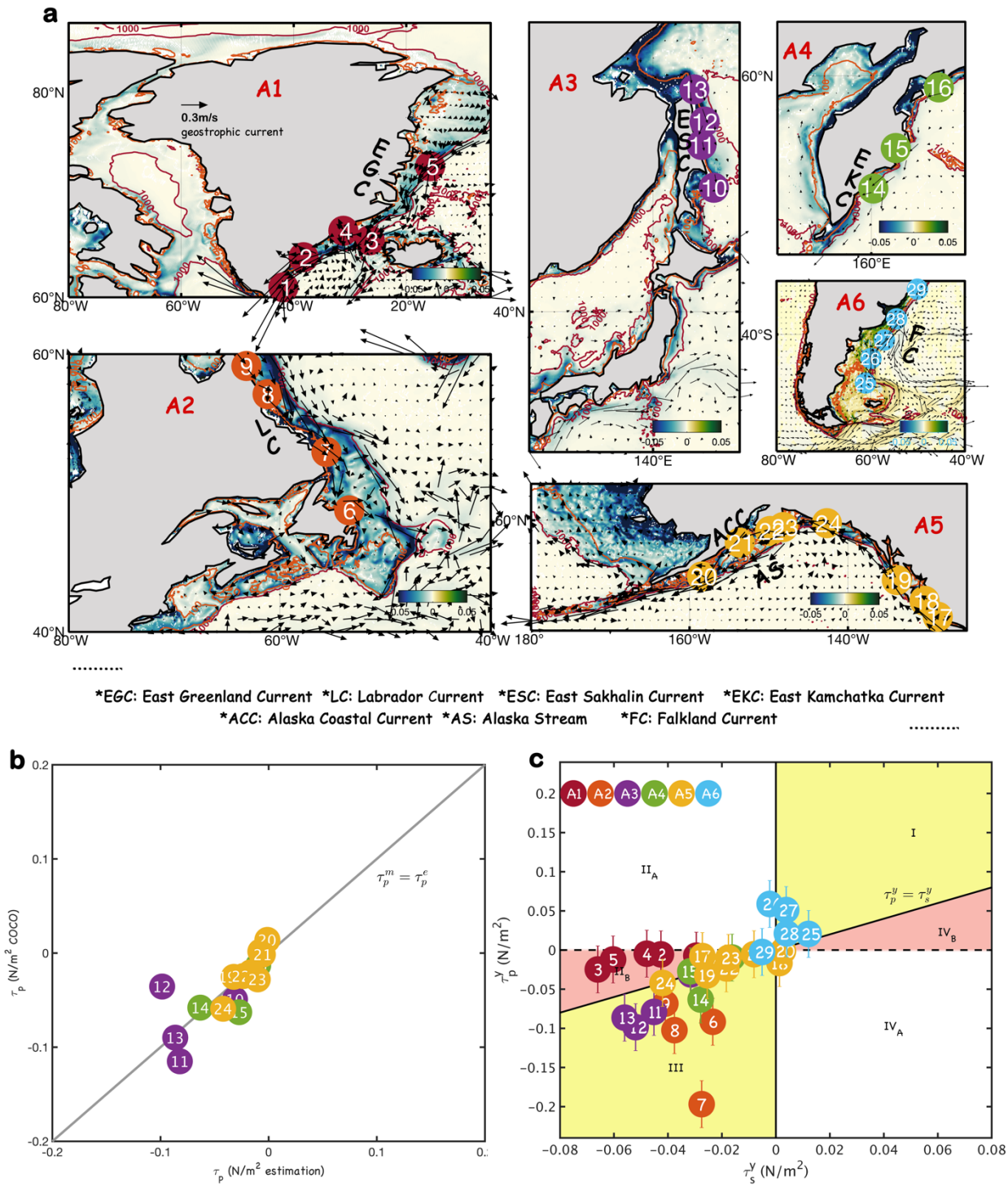

Figure 2.9: Scaling analysis: Implications of the significance of geostrophic stress in various frontal coastal regions

a The shading denotes the climatological wintertime mean (the January mean in the Northern Hemisphere and the August mean in the Southern Hemisphere) estimated geostrophic stress along the SSH direction in each region. The vectors are the geostrophic

current calculated via the sea surface height above the geoid (see Section 2.3). The numbered dots are the selected points located around the coastal front in each region. We chose six representative coastal regions where downwelling favourable winds are dominant. The contours denote the isobaths at 100 and 1000 m. **b** Geostrophic stress comparison. The x-axis denotes the geostrophic stress value estimated by equation (9), and the y-axis denotes the value modelled by the COCO simulation. The numbered dots correspond to those at the positions in **a**. The COCO simulation includes areas A3–A5. **c** The y-axis denotes the estimated geostrophic stress in the selected six areas, and the x-axis denotes the surface along-SSH wind stress accordingly. The error bar denotes the root mean square difference between the estimated and modelled geostrophic stresses (= 0.03 N/m^2) in **b**.

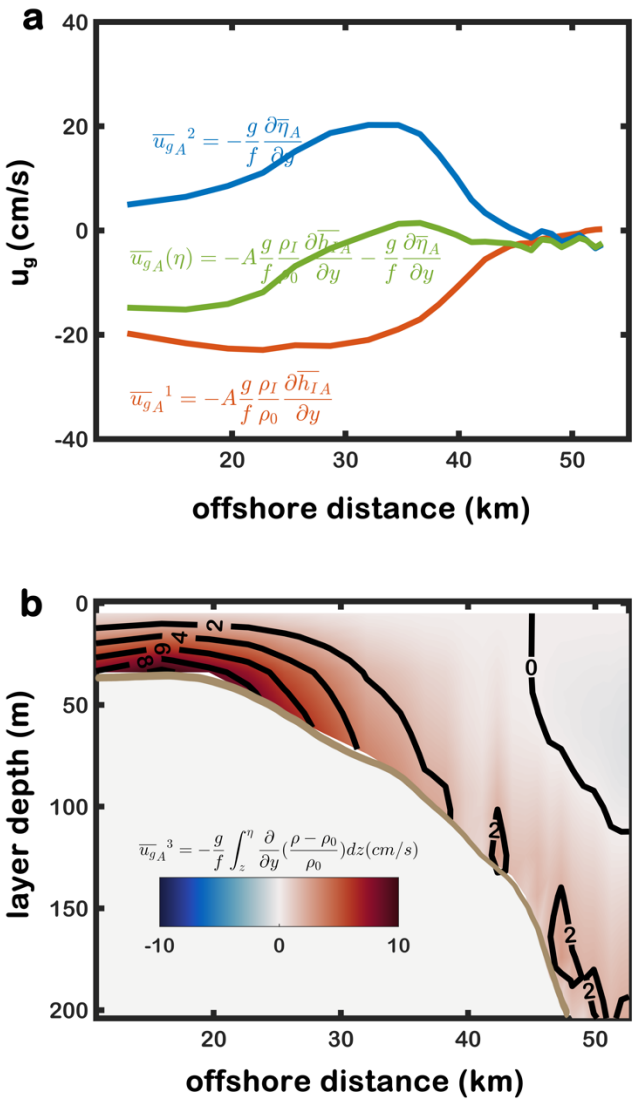

Figure A2.1 a The red line represents the sea ice volume contribution to the barotropic geostrophic cross-isobath current, which is denoted by u_g^1; the blue line represents the sea surface height contribution to the barotropic geostrophic cross-isobath current, which is denoted by u_g^2. The green line is the sum of these two contributions, namely, $u_g(\eta) = u_g^1 + u_g^2$. We smoothed u_g^1 and u_g^2 with the moving average to remove the high-frequency oscillation noises in the open ocean. **b** The shading and black contours denote the baroclinic geostrophic cross-isobath current derived from the along-isobath density gradient, which is denoted by u_g^3.

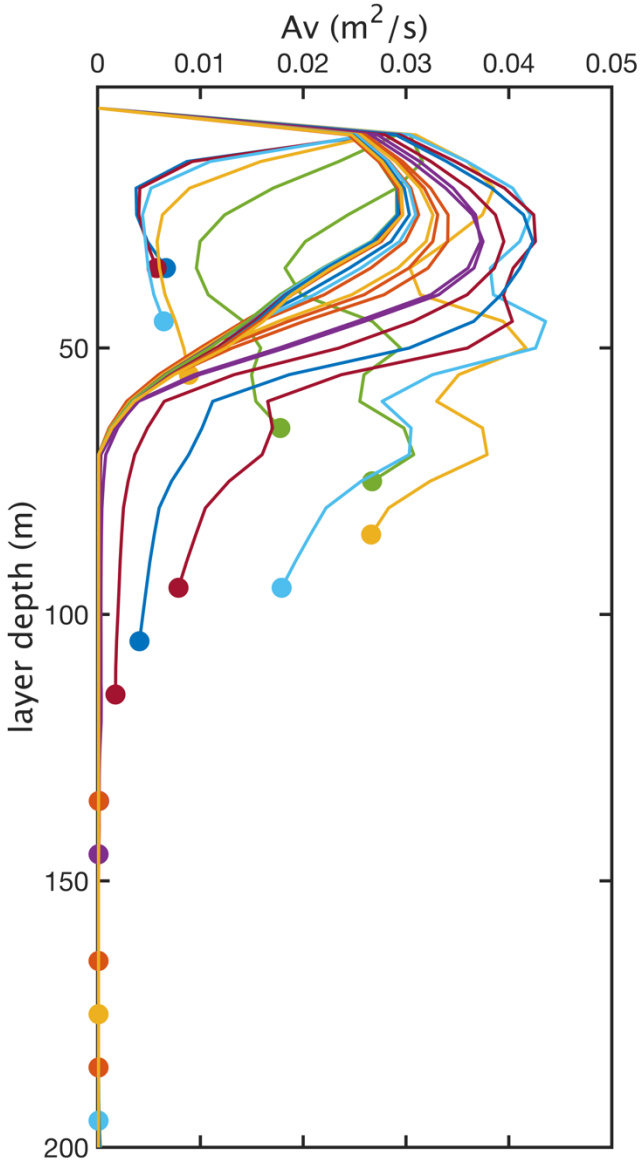

Figure A2.2 Vertical eddy viscosity $\overline{A_{v_A}}$ in different depth denoted by the colorful end points, which presents the cubic profile from the coast to the open ocean in the along-isobath averaged area.

This page intentionally left blank

Chapter 3

Case2: Northwestern Gulf of Alaska

3.1 Introduction

Upwelling provides a primary biological production system. Its formation is generally explained by the Ekman theory (1905) due to the combination of an upwelling-favorable wind and a unilateral boundary. Cold and nutrient-rich water entrained by coastal upwelling fertilizes the euphotic zone and facilitates fisheries via a food web (Kämpf & Chapman, 2016). Uncommonly, the northwestern Gulf of Alaska (GOA), even though it is an important fish catch field, is a predominantly downwelling regime. Ware and Thomson (2005) revealed that the Kodiak region is one of the areas where the annual mean chlorophyll-a concentration and the long-term annual yield of resident fish exhibit a high covariation, which implies a rich primary production in this domain. However, the mechanism by which necessary nutrients for primary production, e.g., iron and nitrogen, are 'advected' onto the shelf and upwelled to support the spring bloom remains an unresolved question (posed by Stabeno et al., 2004 and Ladd et al., 2005), and an upwelling is anticipated.

There have been several studies regarding the reason for nutrient enrichment near the eastern coast of the GOA and south of Kodiak Island (see the locations in Fig. 3.1). They found that the possibilities for nutrient enrichment in these regions are not only due to local upwelling caused by wind stress curl but that they are also induced by phenomena such as coastal water trapped in eddies. (Ladd et al., 2005; Stabeno et al., 2004). The gradient of the cross-shelf transport due to the eddies' movement is one of the reasons for the local upwelling that was detected by the satellite and hydrographic observations (Okkonen et al., 2003). Tide-induced convection inside the troughs found southeast of Kodiak Island was also observed (Ladd et al., 2005). In terms of a wind effect, Stabeno et al. (2004) proposed that the wind stress curl associated with a coastal barrier jet (Parish,

1982; Loescher et al., 2006) may explain the seaward upwelling near the eastern and northern GOA because of the intensifying wind stress near the coast. In that case, an Ekman pumping approximately 10m/day on average could be generated under conditions comprising a nearshore wind speed of 14m/s and an offshore wind speed of 10m/s across a width of 20km.

The above studies are helpful in terms of understanding the primary production to the east and south of Kodiak Island, while a high chlorophyll-a concentration was also observed west of Kodiak Island, where the Alaska Coastal Current (ACC) flows and in the region where the ACC and Alaskan Stream (AS) are confluent (see the chlorophyll-a concentration in, for example, Fig. A3.1 from the Aqua Moderate Resolution Imaging Spectrodiometer (MODIS), which was observed in April; also see Figure 4 from Fiechter & Moore, 2009, which was observed in May; Figure 9 from Ladd et al., 2005, which was observed in July-August). Observations in winter are difficult to collect in this region due to the dense cloud coverage. Nevertheless, the high covariance between the annual mean chlorophyll-a concentration and the long-term annual yield of resident fish suggests the high primary productivity and nutrient-rich environment to the west of Kodiak Island.

In this study, two regions located in the western GOA where the wind is weaker than that off the northeastern coast of the GOA were investigated. One is located southwest of Kodiak Island where the ACC flows out from the Shelikof Strait, and the other is the confluence of the ACC and AS (marked with A1 and A2, respectively, in Fig. 3.1).

In the vicinity of the A1 study region, abundant zooplankton (Ware & McFarlance, 1989) and pollock aged two and older (Incze et al., 1989, in March; the pollock distribution figure is attached in the Appendix as Fig. A3.4) were observed. Upwelling is anticipated to supply the nutrients essential for life. The barrier jet proposed by Stabeno et al. (2004)

may not be adequate to explain the possible upwelling in this region due to the weaker wind stress there in winter, which is approximately $0.05\mathrm{N/m^2}$, and there is not a significant near-coast amplified wind speed signal (Fig. A3.2). Furthermore, the classic Ekman theory is insufficient in terms of explaining the potential upwelling in the region as the absence of a lateral boundary. At the west end of the Shelikof Strait (Fig. 3.1), the ACC was confined to the northern coast with a surface current of ~0.3 m/s and a vertical current shear $\frac{\partial u}{\partial z} \sim 0.0012\ \mathrm{s^{-1}}$ from April to September in 1991 (Stabeno et al., 1995). The value of the velocity vertical shear is similar to an observed climatological mean in both the winter and summer seasons (Stabeno et al., 2016), and the magnitude is slightly stronger in winter. Rather than continually flowing westward, the primary volume of the strong geostrophic current, which entrains plentiful fresh water from precipitation, ice/snow melting, and runoff (Royer, 1979; Weingartner et al., 2005), shifts to the southwest of Kodiak Island (see the satellite-tracked drifting buoys in Figure 10 in Spitz & Nof, 1991 which is also attached in the Appendix as Fig. A3.5, and Stabeno & Hermann, 1996).

Schumacher and Reed (1980) first revealed the inner shelf current of the ACC and explained it as a buoyancy-driven current due to the cross-shelf pressure gradient with a wind enhancement signal in winter, which is distinct from the AS. The second study region includes the current with freshwater discharge outflowing from the Shelikof Trough (Fig. 3.1) that merges with the AS. Across the AS, the observed surface salinity in Feb.-Mar. 1980 (Figure 6a of Reed, 1984; the figure is attached in the Appendix as the Fig. A3.6) presented a range from 32.0 to 32.6 psu, which is larger than that south of Kodiak Island (upstream of the AS), where the surface salinity across the AS ranges from 32.4 to 32.6 psu.

The AS is the western boundary current of the Alaskan Gyre, and it responds to the wind stress curl. The current velocity can be as strong and exceptional as 1 m/s (Reed, 1984). To study pollock recruitment in the Shelikof Strait, Stabeno and Reed (1991) deployed satellite-tracking drifting buoys between the Alaska Peninsula and Kodiak Island in 1986 and 1987. Only one buoy drifted out of the AS and joined the central gyre in February, and this phenomenon is considered to be due to a local wind. The study uncovered the ACC trajectory after it flowed out of the Shelikof Strait, which corresponded to the observed pollock distribution. However, the reason for the enrichment of nutrients in the region still remains a question.

In this study, we explored the impact of the stress due to the geostrophic current shear, which we call the geostrophic stress, on the local upwelling in the freshwater fronts near the west of Kodiak Island and the confluence of the ACC and AS. Previous research (Cronin & Kessler, 2009; Chen & Chen, 2017; Yuan & Mitsudera, 2022) has studied a modified Ekman transport using geostrophic stress. In these studies, a geostrophic current shear due to the thermal wind relation inside the Ekman layer modifies the Ekman transport, which reshapes the vertical motion as well. In this research, we consider the study region one of the candidates to adopt this process. To verify this hypothesis and study the upwelling system in the northwestern GOA, we conducted the analyses detailed in this paper.

The contents of this study are organized as follows: In Section 3.2, we introduce the data source and methodology. In Section 3.3, we depict the climatological January mean and the physical properties of the ACC and AS and reveal the cross-shelf transport, including the vertical motion, in these regions. A dynamical interpretation and analysis are also

provided in this section. In Section 3.4, we summarize the results and discuss the limitations of the data analysis and possible future advancements.

3.2 Model and data analyses

3.2.1 North Pacific submesoscale-permitting simulation

The OFES2 (Sasaki et al., 2020) is an upgrade quasi-global Ocean General Circulation Model (OGCM) of the OGCM for the Earth Simulator (OFES) based on the Modular Ocean Model (MOM3). The OFES has been broadly used and has effectively elucidated the basin-scale eddy phenomena and the 'eddy'/'large circulation' interaction (Masumoto et al., 2004; Masumoto, 2010). The OFES2 permits submesoscale circulations in the North Pacific (Sasaki et al., 2022) and has a finer regular horizontal grid with a resolution $1/30^{\circ} \times 1/30^{\circ}$ in a domain of $100°\mathrm{E} - 70°\mathrm{W}$ and $20°\mathrm{S} - 68°\mathrm{N}$, which starts from the temperature and salinity fields in 1991 of the quasi-global OFES2 with a resolution $1/10^{\circ} \times 1/10^{\circ}$. The model has105 vertical z-levels. The vertical grid size in a shallow layer, down to ~140m, is 5 meters, and that down to ~250m is 10 meters; the grid's vertical size gradually increases with depth (Sasaki et al., 2020). A turbulence closure scheme proposed by Noh and Kim (1999) is adopted to simulate the eddy viscosity and diffusivity in the mixed layer. The model includes the tidal adjustment mixing parameters, which modify the diffusion over the rough topography (St. Laurent et al., 2002). According to the simulation, the tidal motion amplifies the vertical diffusivities over a rough bottom topography (Sasaki et al., 2020). ETOPO1 data is adopted as the model bathymetry. The model also incorporates the monthly climatological river runoff from the Coordinated Ocean-ice Reference Experiments Phase 2 (CORE2, Large and Yeager, 2009) and a sea ice module. The three-hourly Japanese 55-year Atmospheric Reanalysis of the driving ocean-sea-ice model (JRA55-do, Tsujino et al., 2018) from 1990 to 2019 is

adopted as the atmospheric forcing. The relative wind speed responding to the surface oceanic current is considered the surface momentum flux.

We processed the OFES2 output to a climatological January mean over a period from Jan. 1996- Jan. 2019 for further analysis.

3.2.2 Following the sea surface height (SSH) coordinate

Considering the intricate topography of the GOA, which featured several banks, troughs, valleys, and glaciers during the Last Glacial Maximum (Zimmermann et al., 2019), the SSH is adopted instead of the isobath as an indicator for establishing an SSH coordinate to identify the geostrophic and ageostrophic currents. Specifically, the along- and cross-SSH components of a vector variable (we use the velocity $\vec{u}$ as an example) are defined as follows:

$$u = \vec{u} \cdot \hat{x}_s,\ v = \vec{u} \cdot \hat{y}_s$$

and

$$\hat{y}_s = \hat{z}_s \times \hat{x}_s,$$

where $(\hat{x}_s, \hat{y}_s, \hat{z}_s)$ denotes the SSH coordinate obeying the right-hand rule, and $\hat{x}_s(\hat{y}_s)$ denotes the cross (along)-SSH direction. $u(v)$ is the cross (along)-SSH component of the velocity $\vec{u}$ (Fig. A3.3).

The similarity between the barotropic current (Fig. 3.2) and the along-SSH current on the 10m layer (Fig. A3.3b) indicates that the along-SSH current mostly represents the barotropic current, although it is slightly stronger on the upper layer; the along-SSH current is considered to respond primarily to the geostrophic effect. As we can see in the later analysis, the vertical shear depicted by the along-SSH current also represents the

geostrophic thermal wind, which is analogous to the observations. The cross-SSH current is then considered the ageostrophic component (Fig. A3.3a).

3.2.3 Along-isobath averaged variables

To remove the local calculation ambiguity, the along-isobath averaged values inside the study regions are calculated. The detailed calculation, referencing Stewart et al. (2009), is as follows:

$$[\bullet]_{isobath} = \iint_{isobath_1<isobath<isobath_2} \bullet \, dA, \text{and}$$

$$\overline{\bullet} = \frac{[\bullet]_{isobath}}{A}.$$

where A is an area selected for conducting the along-isobath average within an isobath range $[isobath_1\ isobath_2]$. The two isobath boundaries are selected as the two adjacent model-separated vertical z layers. $[\bullet]_{isobath}$ denotes the integrated variable. After dividing by A, we obtained $\overline{\bullet}$, which is an along-isobath averaged variable inside the selected region A. In the following content, the subscript A denotes a variable incorporated into the above along-isobath average. Note that without special explanation, in this context, the variables presented in a profile are along-isobath averaged variables.

3.2.4 Climatological monthly mean wind field

The horizontal grid spacing of the atmospheric forcing JRA55-do is approximately 55km. We processed the 3-hourly mean 10m height wind speed data over a period from Jan. 1st, 1958 ~ Dec. 31st, 2019, into the climatological monthly mean. The wind stress $\vec{\tau}_s$ is calculated based on the bulk formula (Large & Yeager, 2004), which is expressed as follows:

$$\vec{\tau}_s = \rho_a C_D \sqrt{(u_{10}^2 + v_{10}^2)}\vec{u}_{10}$$

where $\rho_a \approx 1.22\text{kg/m}^3$ is the near-surface air density, $\vec{u}_{10}$ is the 10m height wind vector, and $C_D \approx 1.3 \times 10^{-3}$ is the air-sea drag coefficient. While the OFES2 model adopted the relative wind stress $\vec{\tau}_{s-ofes}$ (we inherited the terminology from Munday & Zhai, 2015), the surface momentum flux is then calculated as follows:

$$\vec{\tau}_{s-ofes} = \rho_a C_D |\vec{u}_{10} - \vec{u}_s|(\vec{u}_{10} - \vec{u}_s)$$

where $\vec{u}_s$ is the surface oceanic current vector.

The Ekman pumping $\vec{w}_{p\_a}(\vec{w}_{p\_r})$ by the curl of $\vec{\tau}_s$ $(\vec{\tau}_{s-ofes})$ is calculated as follows:

$$\vec{w}_{p\_a} = \frac{1}{\rho_0 f}\nabla \times \vec{\tau}_s, \text{ or } \vec{w}_{p\_r} = \frac{1}{\rho_0 f}\nabla \times \vec{\tau}_{s-ofes} \qquad (3-1)$$

where $\rho_0 = 1023.6\text{kg/m}^3$ is a reference oceanic density, and $f = 2\Omega sin\varphi \sim 1.2091$ rad/s is the vertical component of the Coriolis parameter at approximately 56°N.

3.3 Results

3.3.1 Simulated flow field in the northwestern GOA

We present the simulated climatological January mean surface density and barotropic current $\bar{u}=\int_{-H}^{0} \vec{u}\, dz \Big/ H$, where H is the entire water column depth, in Fig. 3.2. The stronger currents along the coast and the open ocean shelf break are identified as the ACC and the AS, respectively. In the A1 study region, the freshwater-enriched ACC is constrained inside the Shelikof Trough, where the velocity of the barotropic current is ~0.1 m/s, and the surface density range is 1025.2~1025.4 kg/m^3. The simulation also reproduces the abrupt shift of the ACC axis, which turns to the left-hand side and moves along the southward 200m isobath. The result is consistent with the observations introduced in Section 3.1. The shift of the current's axis renavigates the strong- and freshwater-enriched ACC and constrains it to the southern bank. The outflow of the ACC, which mingles with the AS, desalinates the water in the A2 region, where the surface density

ranges from 1025.4 to 1025.8 kg/m^3, while in the upstream of the AS, its range is approximately 1025.6~1025.8 kg/m^3. The strongest barotropic current there is constrained to a narrow strip with a velocity of ~0.2 m/s.

The topography inside the channel of the A1 region monotonously descends from the coast to a depth of ~250m, while the isobath is circled in the middle area, which is deeper than 250m (Fig. 3.3a). Due to this topography distribution, the along-isobath averaged variables in the area deeper than 250m are removed to present a near-uniform along (cross)-isobath direction, and then, the region is separated into a southern and northern half. In the A2 region, there is a broad shoal shallower than 100m with slight submarine bumps. A steep shelf break is located at approximately the 150m isobath. In between the shoal and the shelf break is a gently sloping topography (Fig. 3.3b).

Furthermore, we calculated the along-isobath averaged variables following the method described in Section 3.2.3. The profile of the along-isobath averaged density and along-SSH current in the A1 region are presented in Fig. 3.4a. On the southern half's bank, there is a density front and a strong baroclinicity with a depth of 150m, where the vertical shear of the along-SSH current $\frac{\partial|\vec{u}|}{\partial z}$ is ~0.0007s^{-1}. The surface along-SSH current is ~0.15m/s. The strong baroclinicity at the west end of the Shelikof Strait was also observed year-round (Stabeno et al., 2016). On the northern half's bank, the water is barotropic with a near-constant current and density.

The profile of the along-isobath averaged density and along-SSH current in the A2 region are presented in Fig. 3.4b. There is strong baroclinicity and a surface current of ~0.55 m/s at an approximate depth of ~200m, where the vertical shear of the along-SSH current $\frac{\partial|\vec{u}|}{\partial z}$ is ~0.0013s^{-1}, and a density front dominates. These features are distinguished from

the shoal and the deep ocean. In the shoal, the current is weak, and the density is near-uniform. In the deep ocean, a mixed layer is simulated up to ~80m. The front ends at the shelf break.

3.3.2 Wind field in the northwestern GOA

As wind stress curl is considered important for local upwelling, we further analyzed the climatological January mean wind field in the study regions. A uniform along-shelf wind is usually adopted in coastal simulations, as the scale associated with the wind stress curl is considered far larger than the shelf scale itself (e.g., this presumption is accepted in the continental shelf waves study from Gill & Schumann, 1974), while the results described in this section may emphasize that the local sea surface current in winter may generally create and reshape a wind stress gradient in the study regions.

We present the climatological January mean relative wind stress $\vec{\tau}_{s-ofes}$ in Fig. 3.5a. The shading denotes the curl of $\vec{\tau}_{s-ofes}$. The northeasterly wind, which is a downwelling-favorable wind, dominates the domain, including the study regions. $\vec{\tau}_{s-ofes}$ is $\sim +0.04\mathrm{N/m^2}$ in the A1 region and is $\sim +0.02\mathrm{N/m^2}$ in the A2 region. There is a strip of enhanced positive relative wind stress curl between the 100-250m isobaths in A1 associated with the negative sea surface current vorticity, while the negative relative wind stress curl is presented in areas deeper than the 250m isobath and shallower than the 100m isobath and is associated with the positive sea surface current vorticity. The positive relative wind stress curl is enhanced in the A2 study region for the same reason. For comparison, the climatological January mean absolute wind stress $\vec{\tau}_s$ is presented in Fig. A3.2 with black arrows, and the shading denotes the curl of $\vec{\tau}_s$. We find that the absolute wind stress curl is one order smaller than the relative wind stress curl in both study regions (Fig. A3.2).

Near the coast of the GOA's northeast top, the absolute wind stress is extraordinarily strong (Fig. A3.2), which may be explained by the barrier jet since it acts as an intensified coastal wind stress due to the inland mountainous topography. Under this condition, the seaward upwelling may generate due to the cross-shelf wind stress gradient, which was also proposed by Stabeno et al. (2004). However, there is no similar barrier jet phenomenon along the other coastal regions in the northwestern GOA to account for the local seaward upwelling.

The Ekman pumping due to the relative wind stress curl is presented in Fig. 3.5b, where we reiterate that the OFES2 is driven by the relative wind stress. Compared to the absolute wind stress, the relative wind stress and its Ekman pumping exhibit small structures associated with the oceanic surface current field. Notably, the positive wind stress curl and the Ekman upwelling are evident along the ACC and AS.

3.3.3 Strong upwelling along the ACC and AS

The model-simulated vertical velocity on the 10m layer is presented in Fig. 3.6a. Strong upwelling is found along the ACC and AS. Comparing Figure 6a with Fig. 3.5b, even though the Ekman pumping by the relative wind stress is consistent with the model-simulated upper layer vertical motion, the latter has much larger values than the former. Around the southern bank of the A1 region and on the slope of the A2 region, the simulated vertical velocity on the 10m layer corresponds to the horizontal current divergence and the convergence on the same depth (Fig. 3.6b). That is, a pair of upwelling and downwelling on the southern bank in A1 corresponds well with the divergence and convergence pattern of the flow on the same depth. A correspondence between the upwelling (downwelling) and the divergence (convergence) in the surface flow is also found in A2. As described in Sections 3.3.4 and 3.3.5, the horizontal divergence is caused

by southward surface transport, which is not expected under the downwelling-favorable wind condition.

Moreover, compared to Ekman pumping (Fig. 3.5b), the model-simulated downwelling is enhanced along the northern coast due to the blocked onshore Ekman transport by the lateral coastline under a northeasterly wind.

3.3.4 Upwelling in the A1 study region

To understand the reason for the vertical motion in these regions and obtain more insights, we drew the along-isobath averaged vertical velocity and cross-SSH velocity profiles in the A1 region (Fig. 3.7c, d). For comparison, the along-isobath averaged Ekman pumping by the relative wind stress is presented in Fig. 3.7a; the along-isobath averaged wind stress and bottom stress are presented in Fig. 3.7b. To draw the isobath-averaged values, the trough is separated into the southern and northern halves due to the closed bottom bathymetric contours below a depth of 250 m. The explanation and operation are provided in Section 3.3.1.

Fig. 3.7c indicates that in the southern half, upwelling predominates in the middle trough and gradually grows stronger with depth. The maximum value is ~+9m/day on the ~200m slope. The downwelling dominates the shallow bank on both sides with a magnitude of approximately -0.5m/day in the northern half and ~-2m/day in the southern half. As for the cross-SSH current (Fig. 3.7d), there is a bank-ward current of ~-0.005m/s in the area where the bottom depth is deeper than 100m in the southern half. In the lower layer from 150-250m with a width of ~10km, where the cross-SSH current difference is ~0.01m/s (Fig. 3.7b), the estimated vertical velocity is ~+8.64m/day (Fig. 3.7a), which corresponds to the model-simulated strongest upslope motion at a depth of

approximately 200m. On the slope with a depth of ~200m in the southern half, the cross-SSH current is ~-0.01m/s, which is the absolute maximum.

It should be noted that the cross-SSH flow in the southern half is southward even near the surface, which is opposite to the Ekman transport by a downwelling-favorable wind, whereas in the northern half, the cross-SSH flow is in the same direction as the Ekman transport. This southward flow corresponds to the surface divergence that is found along the southern bank as seen in Figure 6b. Furthermore, the southern half's upwelling near the surface corresponds to this cross-SSH current divergence. For a rough estimation, in the upper layer from 50-150m with a width of ~10km, the cross-SSH current difference is ~0.005m/s. Then, the estimated vertical velocity with a two-dimensional presumption is ~+4.32m/day, which is comparable with the model-simulated vertical velocity of ~+3~6m/day. To understand the reason for this vertical motion, learning about the cross-SSH current divergence is the key point. Another feature in these regions is that there is a substantial vertical diffusivity (Fig. 3.7e) and viscosity (Fig. 3.7f) coefficient in the upper layer, which is the layer above 100m. In this study, we focus on the processes that cause surface divergence and the associated upwelling.

3.3.4.1 Contribution from the relative wind stress vorticity

Comparing the along-isobath averaged Ekman pumping (Fig. 3.7a) to the vertical velocity (Fig. 3.7c), we can find that the Ekman suction and pumping distribution are consistent with the model-simulated upwelling and downwelling, respectively, although the magnitude of the former is far smaller.

In the southern half of the trough, the Ekman pumping by wind is ~-0.25m/day, which is not comparable to the simulated vertical velocity of ~-2m/day. Similarly, the Ekman suction in the middle trough is ~+0.25m/day, while the simulated vertical velocity is

~+4m/day around the 100m isobath, indicating that Ekman suction is unable to explain the simulated upwelling there. In the northern half, the Ekman pumping of ~-0.1m/day is consistent with the small vertical motion in the middle trough, and there is an intensified downwelling along the coast due to the onshore transport blocked by the Alaskan coast.

Regarding the surface relative wind stress (Fig. 3.7b), its value is ~+0.04N/m^2 in the A1 region. Based on the classic Ekman theory, a northward cross-SSH current (regarded as an ageostrophic current) with a velocity of ~+0.008m/s would be generated if the vertical scale of the Ekman layer is ~50m. This value is close to the simulated cross-SSH current in the northern half trough. On the other hand, the surface current is southward in the southern half (Fig. 3.7d), which is opposite to the classic Ekman theory.

3.3.4.2 Adjustment by the geostrophic stress

The geostrophic stress (e.g., Yuan and Mitsudera, 2022) is considered the dynamical adjustment of the cross-SSH current divergence around the southern half trough, especially in the area where the cross-SSH current is ~-0.005m/s, which cannot be explained by the classic Ekman theory. The geostrophic stress is expressed as $\tau_p^y = -\frac{gA_v}{f}\frac{\partial \rho}{\partial x}$, where g is the acceleration due to gravity, A_v denotes the vertical viscosity coefficient, and ρ is the density. In this area, there is a large geostrophic current shear due to the thermal wind relation (Fig. 3.4a) in addition to a large vertical viscosity coefficient (Fig. 3.7f), resulting in significant geostrophic stress. Since the internal water stress $\vec{\tau}$ is a combination of the wind-induced ageostrophic stress $\vec{\tau}_a$ and the geostrophic stress $\vec{\tau}_p$, i.e., $\vec{\tau} = \vec{\tau}_a + \vec{\tau}_p$, a large internal water stress can be generated by a large geostrophic stress.

To verify whether a reversed Ekman overturning occurs in the southern half of the A1 region, the along-SSH internal water stress τ^y is calculated as follows:

$$\tau^y(x,y,z) = \rho_0 A_v \frac{\partial v}{\partial z}, \qquad (3-2)$$

where v is the along-SSH current, and the superscript 'y' denotes the along-SSH direction. The along-isobath averaged τ^y is presented in Figure 8a. The cross-SSH transport M_e^x from the surface to a typical layer z is correspondingly obtained after making the vertical integration of the cross-SSH current $u_a = \frac{1}{f\rho_0}\frac{\partial \tau^y}{\partial z}$ as follows:

$$M_e^x(x,y,z) = \int_z^0 \frac{1}{f\rho_0}\frac{\partial \tau^y}{\partial z} dz$$

$$= \frac{1}{f\rho_0}[\tau_s(x,y) - \tau^y(x,y,z)]. \qquad (3-3)$$

where the superscript 'x' denotes the cross-SSH direction. The along-isobath averaged M_e^x is presented in Fig. 3.8b.

If we presume that the along-isobath averaged M_e^x is two-dimensional in the (x, z) plane, we can consider M_e^x to be a streamfunction. This presumption is not stringent in the study region, but it is still a heuristic for retrieving the ageostrophic overturning according to the following relations:

$$\begin{cases} u_a = -\dfrac{\partial M_e^x}{\partial z} \\ w_a = \dfrac{\partial M_e^x}{\partial x} \end{cases}, \qquad (3-4)$$

where u_a is the retrieved cross-shelf current, and w_a is the retrieved vertical velocity. Their along-isobath averaged results are presented in Fig. 3.8c and d.

Near the southern half trough at approximately 155.2°W, where the depth is ~100m, there is a maximum $\tau^y \sim +0.2\text{N/m}^2$ that is larger than the surface wind stress $\tau_s \sim +$

$0.04\mathrm{N/m^2}$, and both the surface wind stress and internal water stress are oriented towards the west. Consequently, the transport here is southward according to the modified Ekman overturning, which is in the opposite direction of a normal Ekman transport (Fig. 3.8c). This result is consistent with the simulated southward surface flow (Fig. 3.7d). In the northern half, the calculated τ^y is smaller than the surface wind stress. Therefore, water transport corresponds to the classical Ekman theory. As a result, there is an upwelling with a depth range of ~100m in the southern half's trough driven by the transport divergence (Fig. 3.8d), which is consistent with the simulated upwelling as well (Fig. 3.7c).

The overturning retrieved from the M_e^x reproduces a reversed surface Ekman current on the southern bank and an anticlockwise vertical circulation. It is noted, however, that the retrieved $w_a > +9$ m/day, which is larger than the model output of ~+3~6m/day. We consider that this result occurs because the simulated vertical viscosity coefficient A_v ~0.5m²/s is a considerably large value. The geostrophic stress $\tau_p^y = -\frac{gA_v}{f}\frac{\partial \rho}{\partial x}$ thus may have an overestimated impact on the internal water stress τ^y via the relation $\tau^y = \tau_p^y + \tau_a^y$.

3.3.5 Upwelling in the A2 study region

Analogous to the A1 study region, we present the along-isobath averaged vertical velocity and cross-SSH current in the A2 region in Fig. 3.9c and d. The Ekman pumping is presented in Fig. 3.9a, and the surface wind stress and the bottom stress are presented in Fig. 3.9b.

The Ekman suction by the positive relative wind stress curl is predominant in the entire A2 region. Similar to the A1 region, however, from 55.05°N to 55.15°N, the Ekman

suction of ~+0.75m/day cannot explain the model-simulated vertical velocity of ~+3m/day there. Combining the cross-SSH current and the vertical velocity, two regions of overturning are found in this area, and they are schematically depicted by the purple arrows. The first is an anticlockwise overturning in the upper layer, and the other is a clockwise overturning in the lower layer with a strong bottom downslope current.

From the open ocean to 55.2°N, the surface wind stress (Fig. 3.9a) is ~+0.02N/m^2, which generates an ageostrophic cross-shelf current of ~+0.004m/s within a depth of 50m as deduced by the Ekman theory; this estimation corresponds to the model-simulated cross-SSH current north of 55.05°N. From the open ocean to 55.05°N, the cross-SSH current of ~-0.005m/s is in the opposite direction, again suggesting a reversed Ekman transport.

Note that in addition to the surface maximum of the vertical diffusivity and viscosity coefficients, there is another maximum at the bottom of the gently sloping shelf with a depth of ~150m in the A2 region (Fig. 3.9e-f).

3.3.5.1 Geostrophic stress-modified upper layer overturning

The upwelling in the A2 region involves geostrophic stress-controlled reversed Ekman overturning similar to that in the A1 region. Fig. 3.10a presents the internal water stress according to Equation (3-2), Fig. 3.10b presents the transport according to Equation (3-3), and Fig. 3.10c-d present the retrieved ageostrophic cross-shelf and vertical velocity according to Equation (3-4).

There is a maximum internal water stress of ~+0.2N/m^2 ~50m at approximately 54.95°N, which is almost ten times the surface wind stress of ~+0.02N/m^2. The internal water stress is considered to be regulated by the geostrophic stress, as we find a geostrophic current shear (Fig. 3.4b) and a large vertical viscosity coefficient of ~0.4m^2/s (Fig. 3.9f). As a result, there is a reversed Ekman transport in Fig. 3.10b, upwelling due to Ekman transport divergence in Fig. 3.10d.

3.3.5.2 Geostrophic stress-modified lower layer overturning

If there was only one maximum internal water stress core located on the upper layer of the front, then we would anticipate only one reversed Ekman overturning that dominates the entire front (e.g., Fig. 3.7b, d). On the other hand, if there is another maximum internal water stress in the lower layer as in the A2 region, then the Ekman overturning would be broken into two. Fig. 3.10a presents another internal water stress maximum of ~+0.2N/m^2 at the bottom of depth 150m. Consequently, there is a transport horizontal divergence (Fig. 3.10b) resulting in a downslope current (the southward current in Fig. 3.10c and the downwelling in Fig. 3.10d). The bottom maximum internal water stress allows the water over the gently sloping shelf to flow towards the deep open ocean. The bottom maximum internal water stress is considered to be modified primarily by an

enhanced bottom vertical viscosity (Fig. 3.9f) via the parameterized tidal simulation scheme.

However, the geostrophic stress is unable to explain the strongest upwelling of ~10m/day (Fig. 3.9c) at approximately 55.05°N in Fig. 3.10d. We hypothesize that this upwelling may come from the three-dimensional effect and the impact of the intricate topography. As we analyzed each term of the density evolution equation, we found that the horizontal density advection is balanced by its vertical counterpart (we do not present the figures here), maintaining the density conservation. Namely, the vertical motion may come from the horizontal velocity divergency due to the cross-SSH stress and the complex topographic features.

3.4 Summary and discussion

Observation reveals the pollock distribution in February and March in the downwelling-dominated northwestern Gulf of Alaska. How the nutrients advected and upwelled to the surface to support the local biological system remains a research interest, and we anticipate a local upwelling.

In this study, we primarily analyzed the OGCM OFES2 output to study whether the geostrophic stress is one of the dynamical reasons for the local upwelling around the northwestern Gulf of Alaska, where the downwelling-favorable wind controls the area year-round. The model results indicate that the geostrophic stress can generate a reversed Ekman overturning, including a seaward upwelling in the study regions. A geostrophic-stress-modified internal water stress that is greater than the surface wind stress is simulated in both regions, resulting in the generation of the reverse Ekman transport. Furthermore, the induced surface transport divergence in the area between

the normal and reverse Ekman overturning contributes to the local upwelling even though there is not a lateral coastline. The Ekman pumping is generated by the relative wind stress, which takes part in generating the local upwelling, even though the magnitude of the generated upwelling is far smaller and cannot explain the total simulated vertical velocity.

We further studied the related overturning. A single overturning is connected to a single maximum internal water stress, as in the A1 region. Furthermore, the overturning will be double if there is one more core of the maximum internal water stress, which may happen when the bottom vertical diffusivity and viscosity are intensified by the tide as is the case in the A2 study region.

To retrieve the cross-shelf overturning structure, a two-dimensional assumption was adopted. Because of the intricate topography of the northwestern GOA, however, the simulated barotropic current and vertical velocity do not present an along-SSH homogeneous structure, even in the pick-up small regions. Therefore, the two-dimensional presumption may be an oversimplification, although the results do not lose their essence and are heuristic. The three-dimensional structure should be a future exploration that will potentially reveal more details regarding the upwelling.

In this study, we focused on investigating the roles of the geostrophic stress in the cross-shelf Ekman overturning, and several unclarified phenomena are mentioned as follows and will be studied continually:

(1) The shift of the ACC in the A1 study region. The shift of ACC axis was also observed, which will change the location of the dominant geostrophic stress.

(2) The relation between the Ekman pumping/suction and the frontal formation. As is shown in Fig. 3.5b, 6a, 7a, and 7c, the Ekman pumping corresponds to the model-

simulated vertical velocity even though it is not sufficiently large to explain the simulated magnitude. These results raise research questions regarding our understanding of the consistency of Ekman pumping and water vertical motion.

(3) The connection between the local upwelling and the primary production. This study provides one possible explanation of the upwelling in a downwelling-favorable along-shore wind domain, while a delicate study that elucidates the further connection between the upwelling and biological production will be important in the future.

Figures

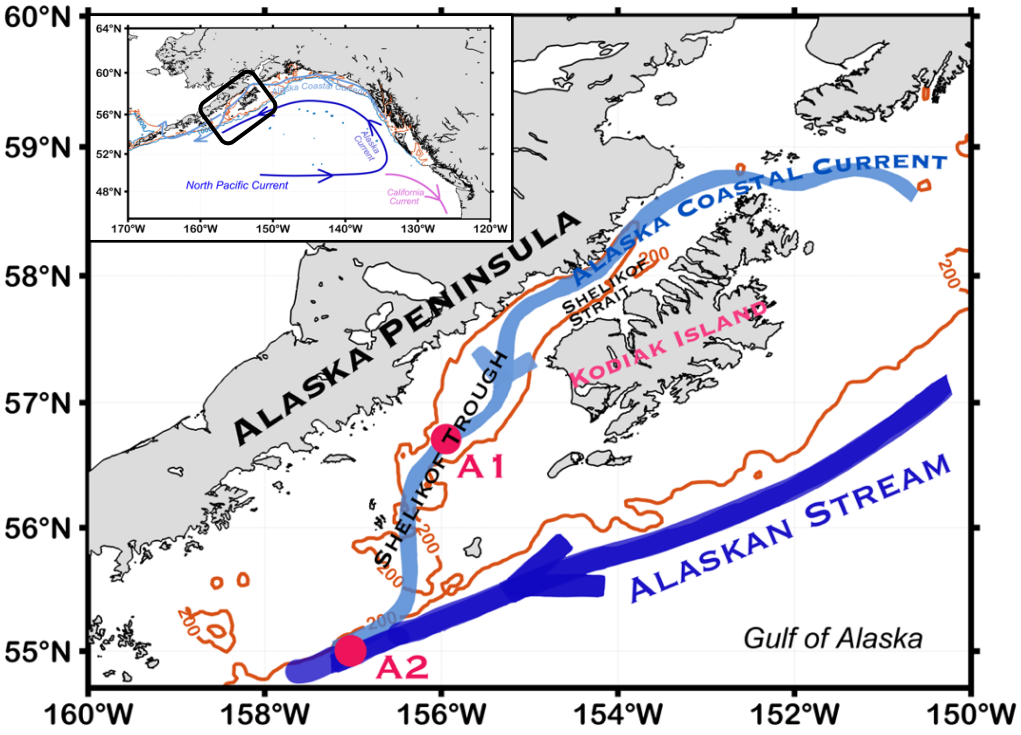

Figure 3.1 Sketch of the study region, northwestern Gulf of Alaska

The analyzed regions A1 and A2, the primary currents, and the mentioned locations in the area are marked in the zoomed-in figure. The figure in the top-left corner depicts the Alaskan Gyre from a zoomed-out perspective, and the region in the bold black box is the zoomed-in area that was the focus of this study. The Alaska Coastal Current in this region is primarily constrained by the Shelikof Trough, and the Alaskan Stream is constrained by the region near the open ocean shelf break. The orange contour represents the 200m isobath.

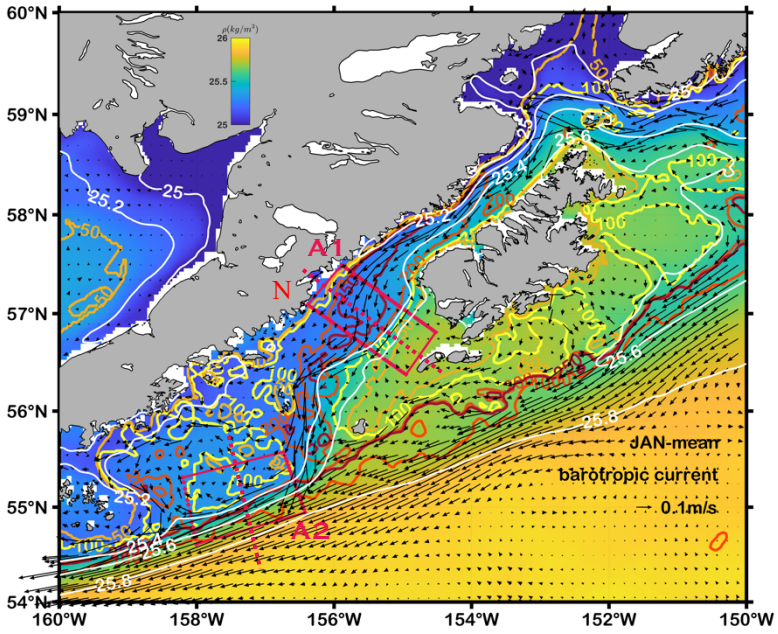

Figure 3.2 OFES2 Climatological January mean (1996-2019) barotropic and baroclinic information around the northwestern Gulf of Alaska

The shading and the thin white contours represent the sea surface isopycnal, where the isopycnal interval is $0.2kg/m^3$. The colored thick contours denote the topography, and the isobath values are 50m, 100m, 200m, and 1000m, which are the same as the information in the maps of the context. The arrows represent the barotropic currents, which are defined as the vertical averaged currents. The two magenta boxes denote the A1 and A2 study regions, where a variable is incorporated into an along-isobath averaged variable in the analysis described in this paper. The dotted lines denote the averaged sections, and 'N' denotes the northward direction.

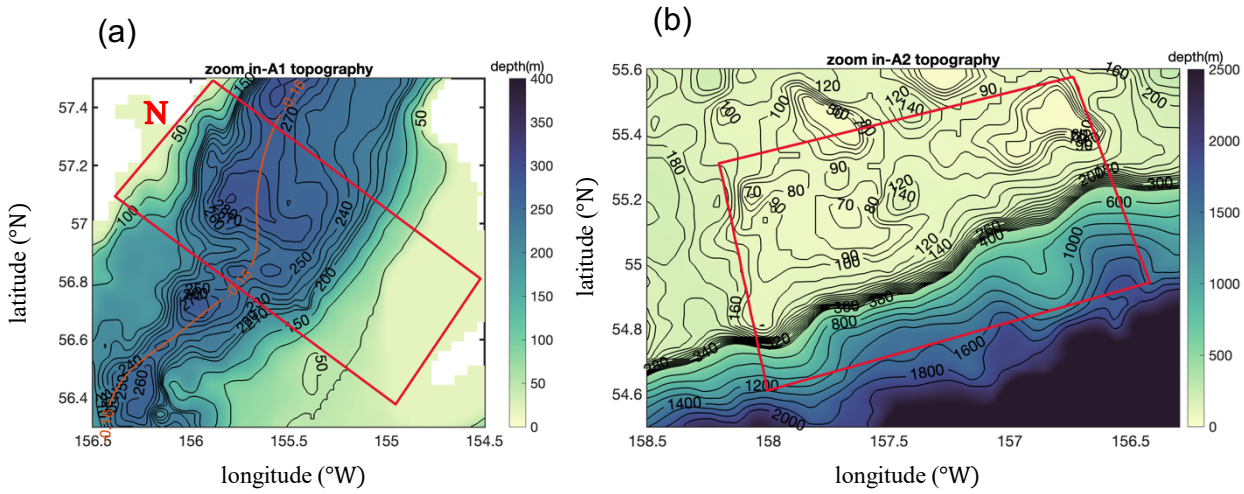

Figure 3.3 Zoomed-in topography in the study regions

a. The red box encloses the A1 study region. The color shading and black contours denote the topography. The orange line is the contour of the sea surface height with the value of -0.16m, which cuts the region into the southern and northern halves (marked by 'N'), and the along-isobath average is calculated in each half region. **b**. The information is the same as that in Figure 3.3**a**, but for the A2 study region.

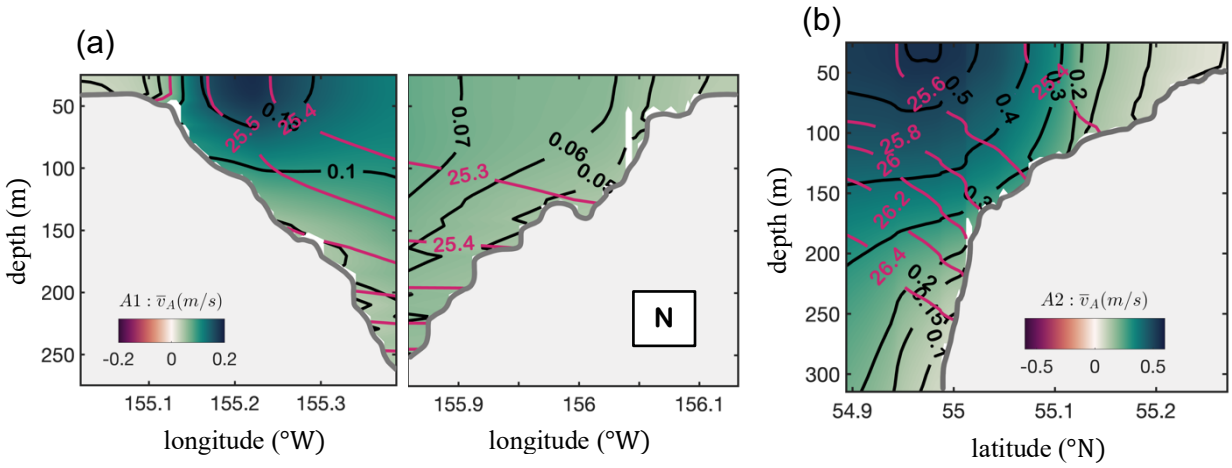

Figure 3.4 Baroclinicity in the study regions

a. The shading and black contours denote the along-isobath averaged along-SSH current inside the A1 area. The magenta contours denote the isopycnal with an interval of 0.1 kg/m^3. The X-axis is the along-isobath averaged longitude, and the northern coast is on the right-hand side. **b.** The variables are the same as in **a** but for the A2 area. In addition, the isopycnal interval is 0.2 kg/m^3, and the X-axis is the along-isobath averaged latitude.

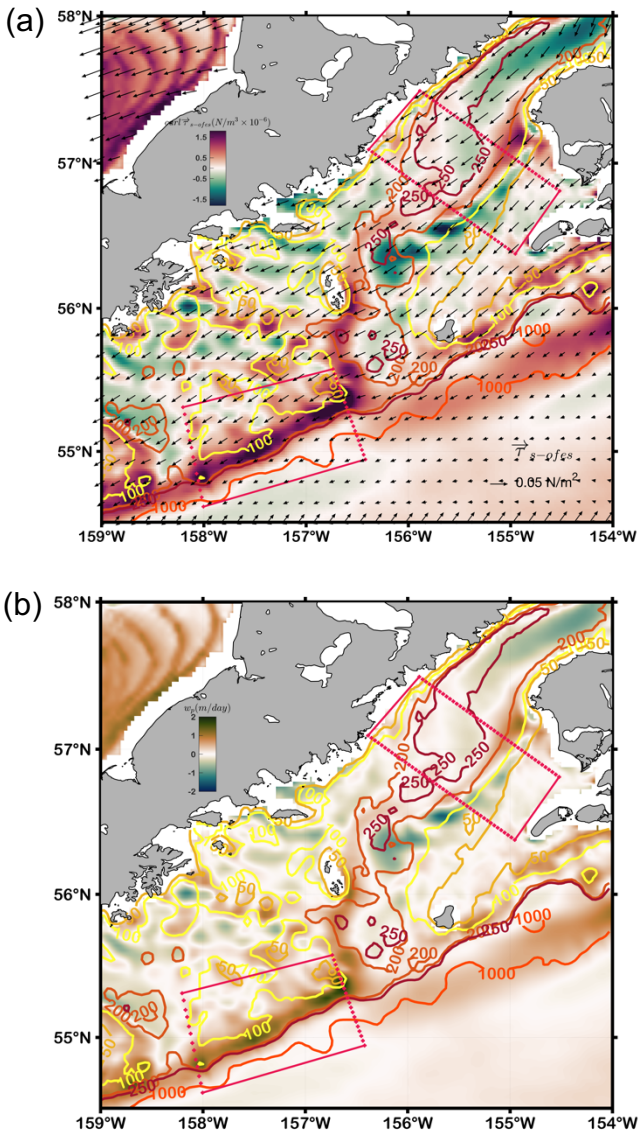

Figure 3.5 Wind field and the corresponding Ekman pumping in the study regions

a. The color shading denotes the relative wind stress curl, and the arrows represent the relative wind stress. **b.** The color shading denotes the Ekman pumping by the relative wind stress.

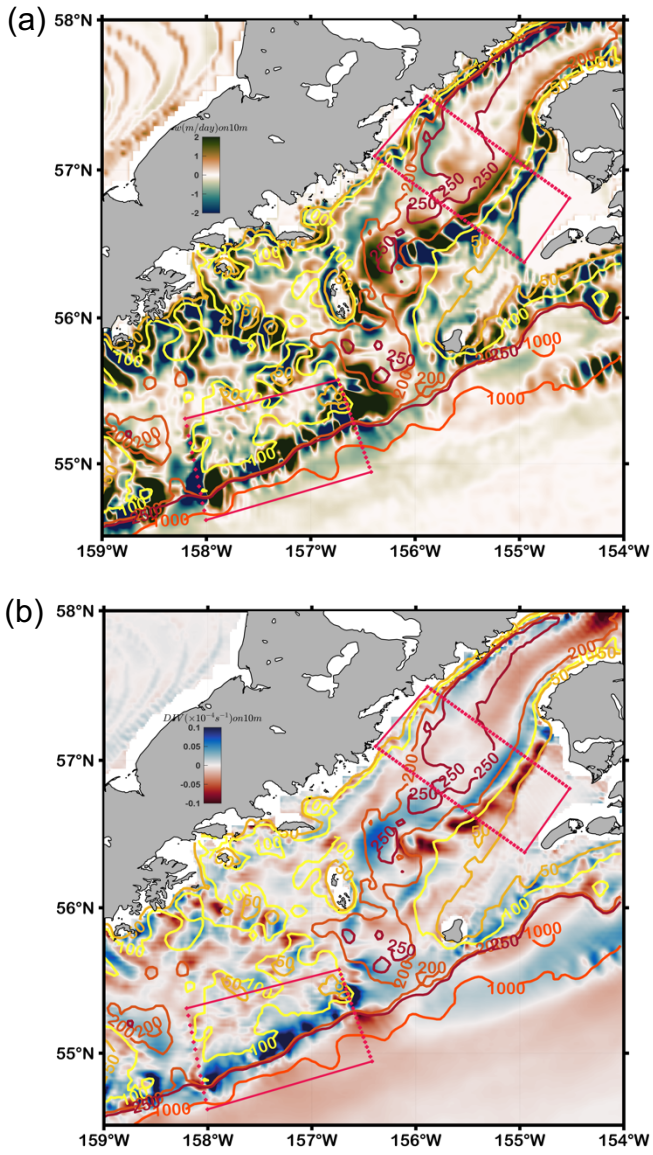

Figure 3.6 Model-simulated current field on the 10m layer

a. The color shading denotes the vertical velocity on the 10m layer. **b**. The color shading denotes the current divergence on the 10m layer. The blue shading denotes the surface current divergence, and the red shading denotes the surface current convergence.

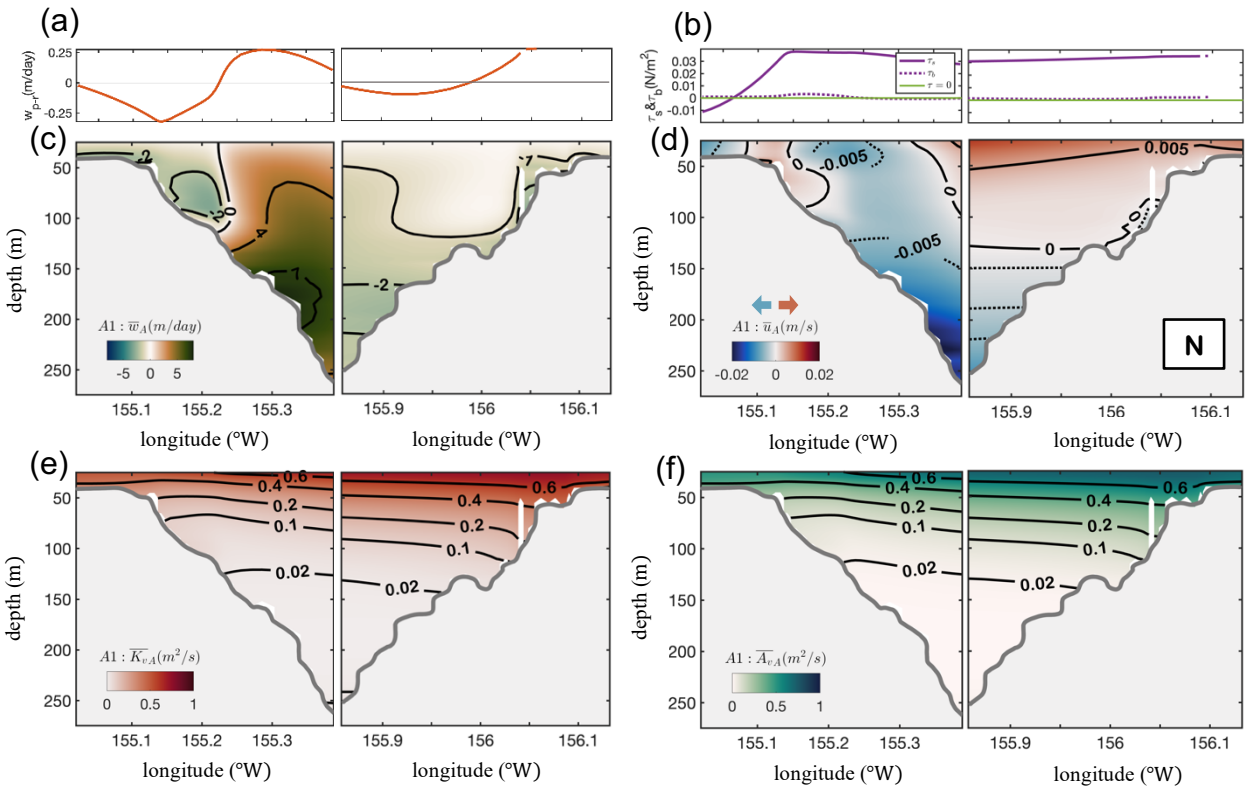

Figure 3.7 Simulated vertical overturning in the A1 region

a. The along-isobath averaged Ekman pumping by the relative wind stress. **b.** The solid purple line denotes the along-isobath averaged surface wind stress, and the dotted purple line denotes the along-isobath averaged bottom friction stress. The green line denotes where the stress is equal to zero. **c**. The color shading and contours denote the along-isobath averaged vertical velocity, and the positive value with the brown shading denotes the upwelling. **d.** The color shading and contours denote the along-isobath averaged cross-SSH current, and the positive value with the red shading denotes the northward cross-SSH current. **e.** The shading and contours denote the vertical diffusivity coefficient. **f.** The shading and contours denote the vertical viscosity coefficient.

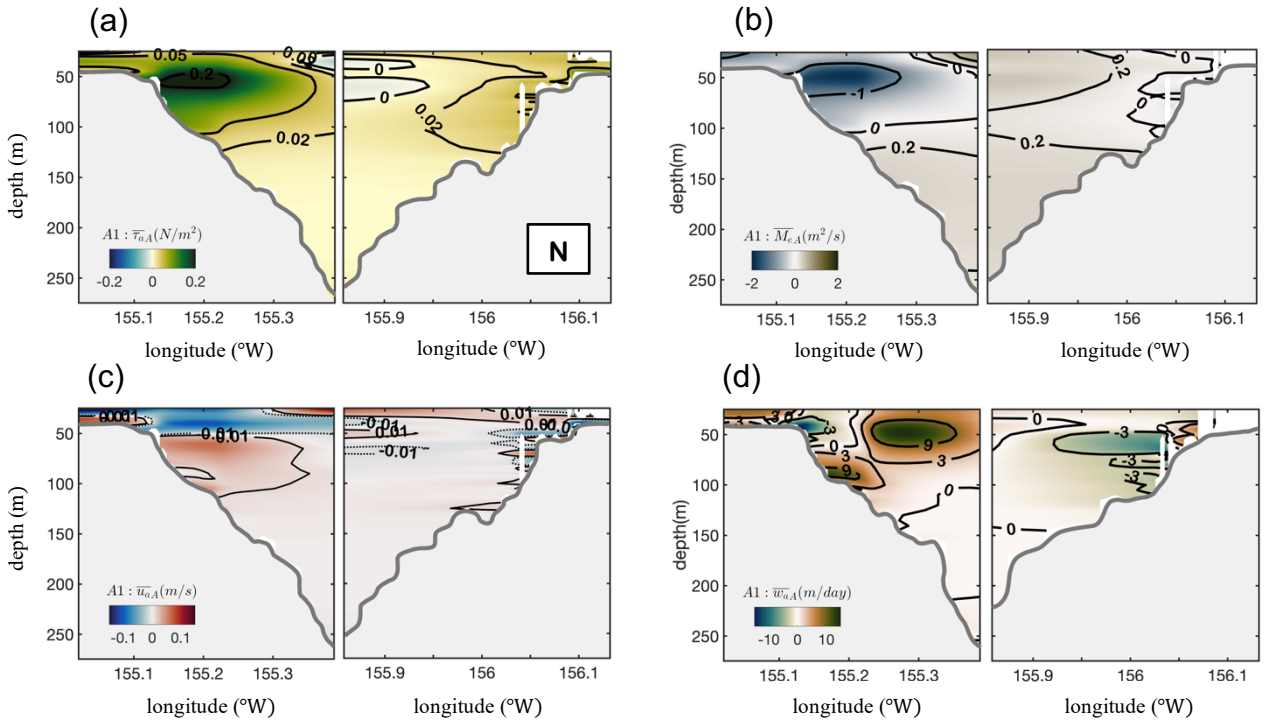

Figure 3.8 Retrieved vertical overturning in the A1 region

a. The color shading and contours denote the along-isobath averaged internal water stress that follows the SSH. The positive value with the greenish shading denotes the westward stress. **b.** The color shading and contours denote the retrieved transport. The positive value with the grayish shading denotes a northward transport. **c.** The color shading and contours denote the retrieved cross-isobath velocity. **d.** The color shading and contours denote the retrieved vertical velocity.

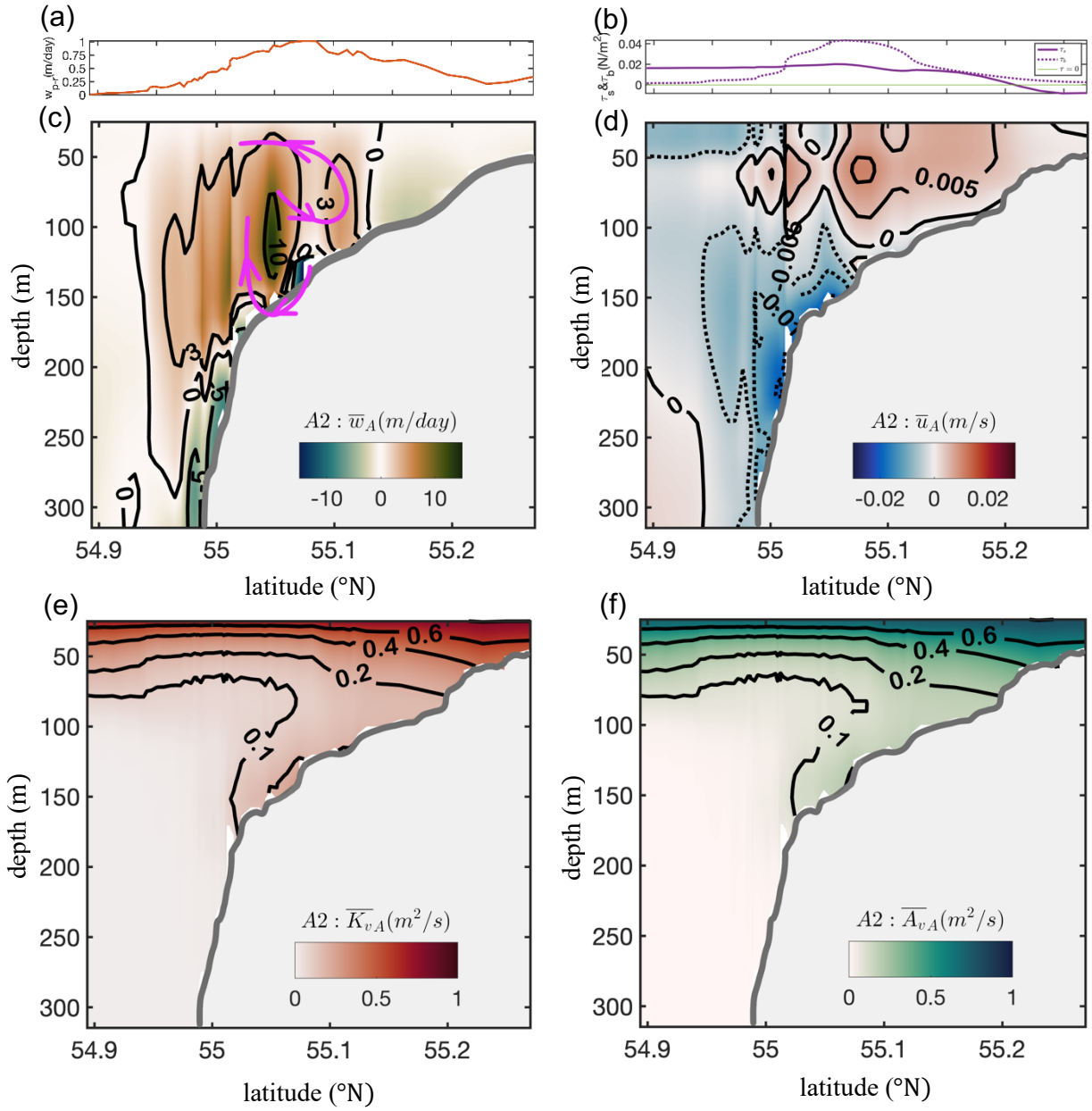

Figure 3.9 Simulated vertical overturning in the A2 region

The variables are the same as those in Figure 3.7 but for the A2 study region.

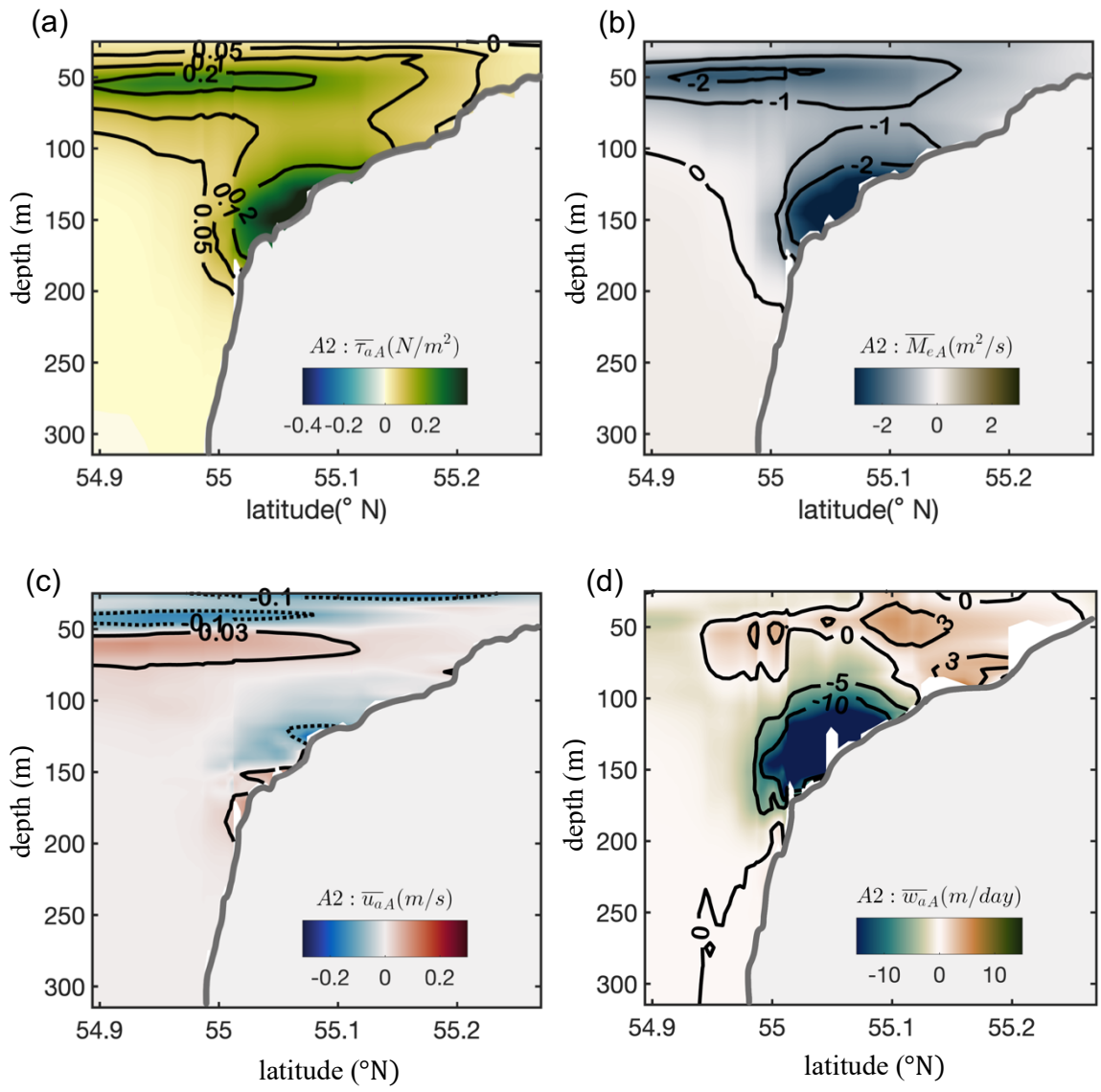

Figure 3.10 Retrieved vertical overturning in the A2 region

The variables are the same as those in Figure 3.8 but for the A2 study region.

Appendix

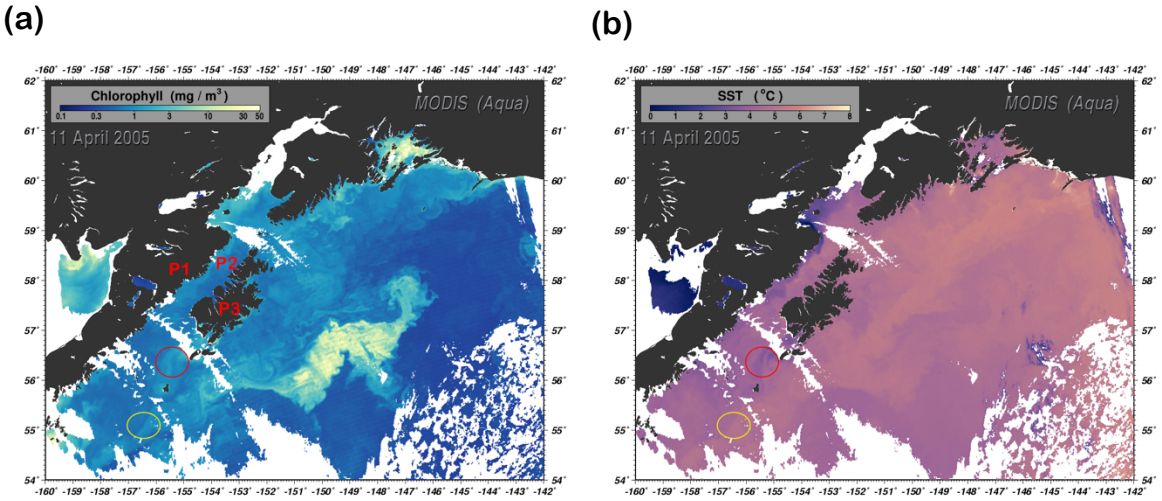

Figure A3.1 observation of chlorophyll-a and the sea surface temperature in Apr. 11 2005 Figure source is https://oceancolor.gsfc.nasa.gov/

a. Shading is the mass concentration of chlorophyll-a in sea water on Apr.11 2005 observed by the Aqua MODIS. The locations marked in the figure with P1~P3, denote P1: Alaska Peninsula; P2: Shelikof Strait; P3: Kodiak Island, respectively. The circles marked in the figure denote the locations we mainly studied in this research; the red circle denotes the valley where the Alaska Coastal Current (ACC) flows out from the Shelikof Strait; the yellow circle denotes the confluent of the ACC and Alaska Stream (AS). The studied regions are denoted in **b** as well. **b.** Shading is the observed sea surface temperature.

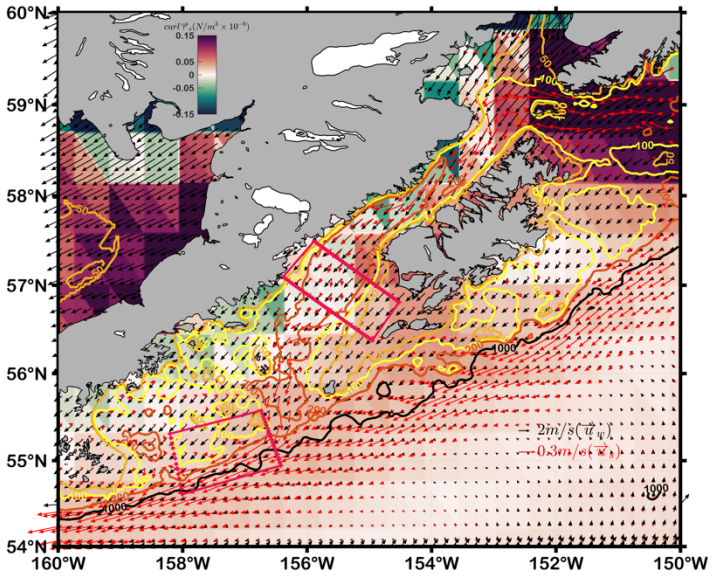

Figure A3.2. The absolute wind fields

Shading denotes the curl of the climatological January mean wind stress ($\vec{\tau}_s$), with the data from the JRA55-do (see subsection 3.2.3 for details). The black arrows denote the wind vector, and the red arrows denote the surface current vector.

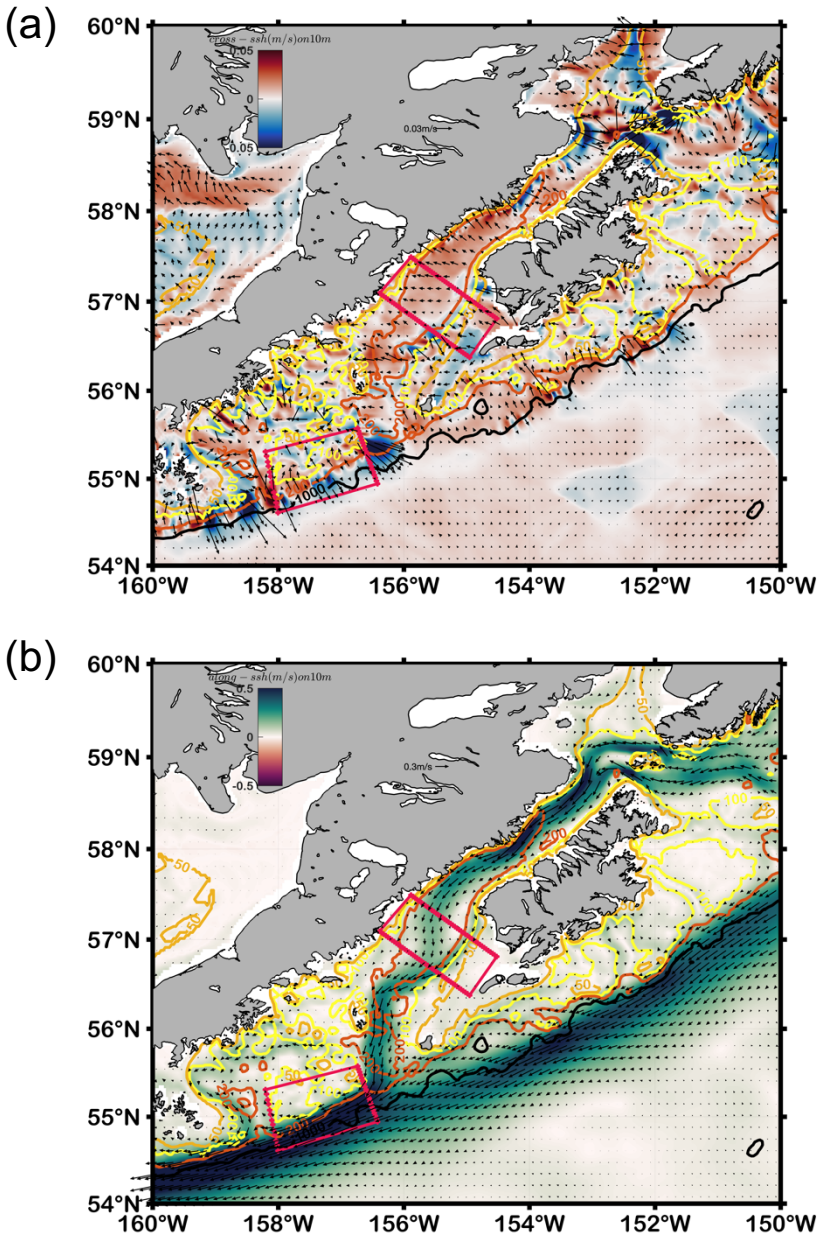

Figure A3.3. Cross- and along-SSH current on the layer of 10m

a. Shading and arrows denote the cross-SSH current on the layer of 10m. **b.** Shading and arrow denote the along-SSH current on the layer of 10m.

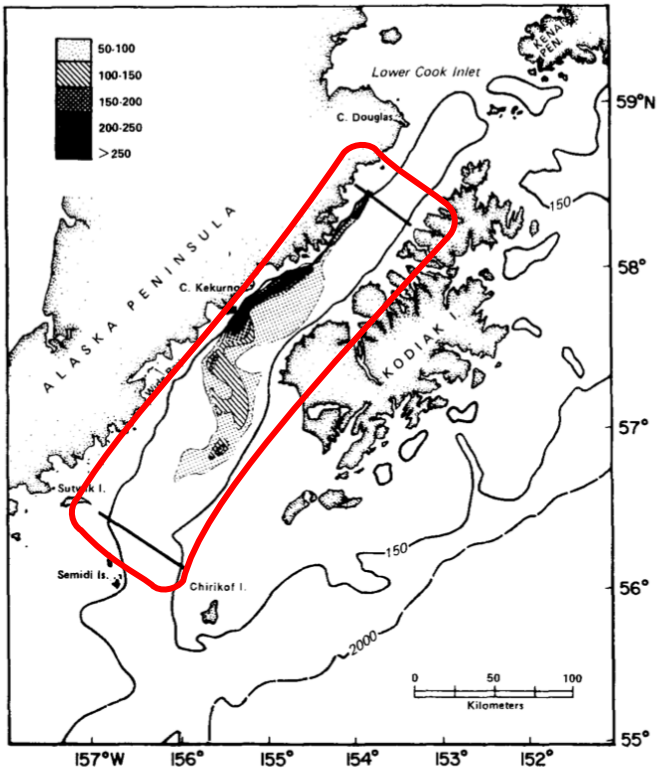

Fig. 2. Areal distribution of pollock age 2 and older during a hydroacoustic survey from 21 to 28 March 1985. Heavy lines delineate survey area in the sea valley. Shading denotes kg live weight of pollock per 1000 m^2.

Figure. A3.4 Figure source: Incze et al., 1989

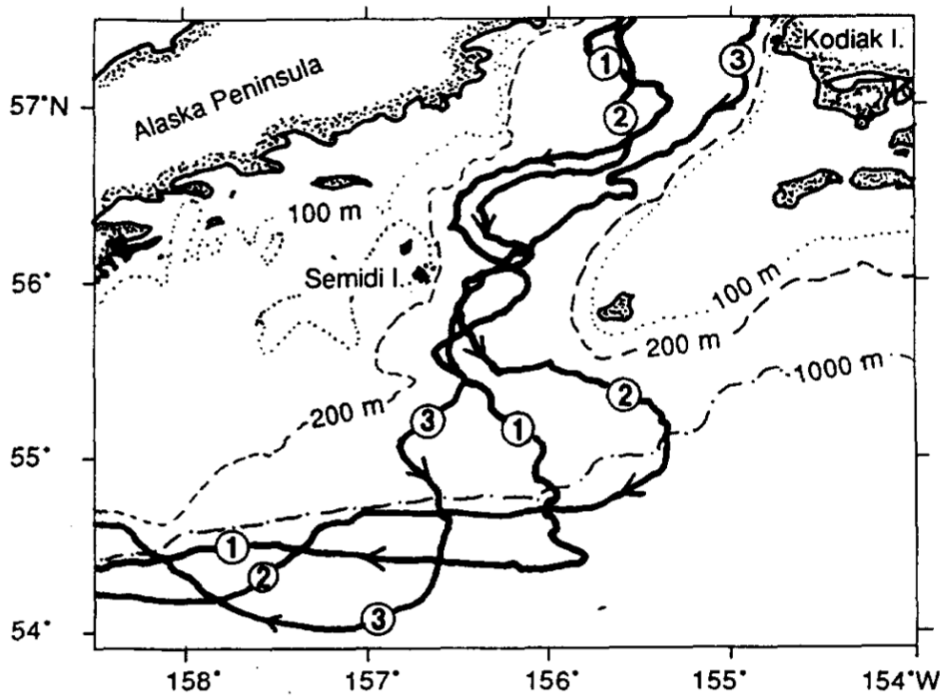

Fig. 10. Three typical paths of satellite-tracked drifting buoys, drogued at 40 m, during May–June 1986 and 1987 (adapted from REED and STABENO, 1989). Note that, upstream (northwest of Kodiak Island), the flow is parallel to the coast. Once it encounters the "step" (the 200 m isobath), it turns offshore as predicated by the qualitative theoretical analysis (Fig. 5) and the laboratory experiment (Fig. 8).

Figure. A3.5 Figure source: Spitz and Nof 1991

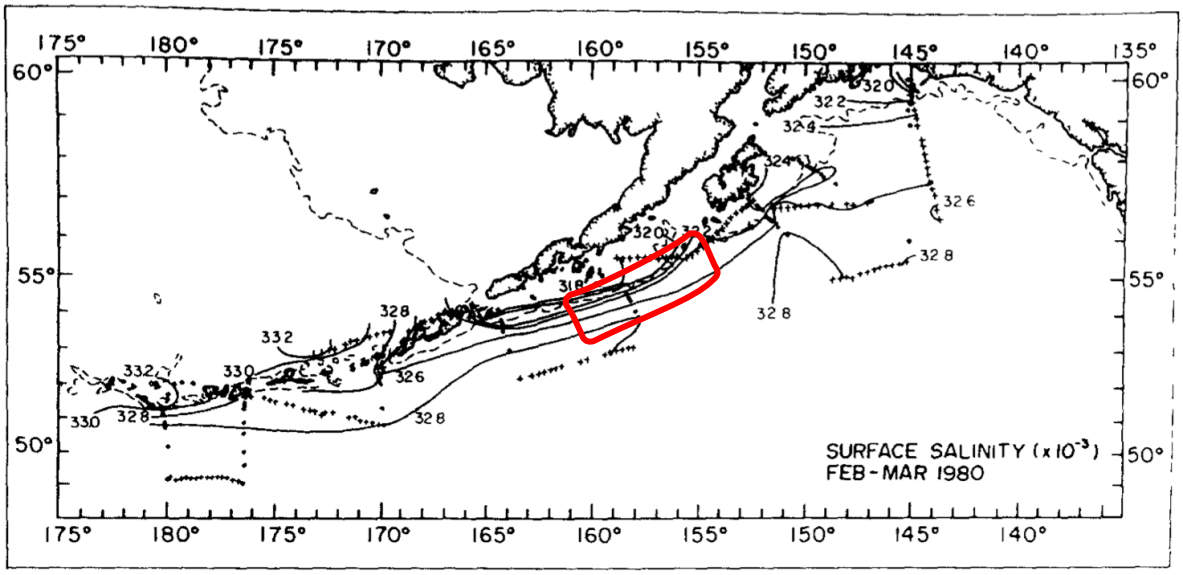

Figure. A3.6 Figure source: Reed 1984

the observed surface salinity in the northwest of the Gulf of Alaska in winter, and a strong cross shelf salinity gradient features the confluence region of the Alaska Coastal Current and the Alaska Stream.

Chapter 4

General discussions

In general, the above analyses indicate that the geostrophic stress modified Ekman layer within a depth of around 100m is capable of facilitating an unusual upwelling under a downwelling-favorable wind both in the cases 'Sea of Okhotsk' and 'northwest of the Gulf of Alaska'. Furthermore, in the case of 'Sea of Okhotsk', a deep mixed layer ~150m simulated and is explained as the convergence of the reversed and normal Ekman transport which is analogues with a deep mixed layer observed in winter in the shelf break of the East Sakhalin but lacking the understanding.

The estimated regions are enriched with riverine freshwater discharge and controlled by the downwelling-favorable wind which implies potential frontogenesis in these areas. The existence of the front implies a geostrophic current shear via the thermal wind relation. A downwelling-favorable wind may be a necessity of a modified Ekman layer for it possibly enhances the vertical mixing. The strong vertical mixing is denoted by a large vertical viscosity coefficient and vertical diffusive coefficient. These conditions make a great geostrophic stress and a further reversed Ekman overturning possible inside the front.

For the both cases, the vertical motions happen away from the lateral boundaries. This indicates that the reverse overturning in the front may act as a '*virtual wall*' that responses to the wind and generates a downwelling and upwelling in its two sides, namely a two-dimensional overturning (the reverse Ekman layer performs like a 'virtual wall' is illustrated in the schematic Fig. 4.1).

The modified Ekman layer (or an equivalent explanation of a 'virtual wall') may have broader applications in coastal areas. Coastal areas in the high latitude discussed in

subsection 2.3.6 are also candidates for the modified Ekman overturning, although each coastal area should have its own characteristics. Combining with the bottom boundary layer the situation will be more complex and a close investigation is needed. In the meantime, the cross-shelf exchange of heat and salinity, as well as nutrient materials, should be strongly affected by the (modified) Ekman overturning. In what follows, further extensions of the present study and the unsolved questions are discussed.

4.1 Extension of the Case1

According to the Chapter 2, we have learnt that it is the river discharge from the Far East Eurasia Continent facilitates the frontogenesis in the gently sloping shelf of the western coast of the Sea of Okhotsk, via analyzing the several sensitive experiments, named CTRL, no-Amur, only-Amur and no-river case. However, the more insights have not been got yet into:

1). Which river and what is its location in the model setting to facilitate the front? Is it possible to identify the river or is it already an entangling information after the freshwater is entrained to the studied region? Confirm the location of the river may not scientific meaningful, while to track how the freshwater is drifted to the region and attend the local mixing may be an interesting question.

2). Which factor determines the scale and offshore location of the front? This is not an easy question to answer, and the previous studies simulated a common shelf break front under a bottom Ekman transport due to the density evolution. Does it mean a volume a fresh water input or the shape (slope) of the topography is decisive for the scale and the offshore location of the front? The original question may be a difficult one but it does not hinder a further conditions(sensitivity) examinations with an idealized model. This also should be an interesting exploration.

3). Frontogenesis, a strong horizontal stratification, is inevitable for a great geostrophic stress, if the fresh water is one of necessary conditions to the frontogenesis, then, what kind of the process is it to shape the front finally? The scheme I adopted till now to simulate the mixing process is the 'turbulence closure model' with a hydrostatic assumption, what is the difference to simulate the process with a non-hydrostatic model? Does the downwelling-

favorable wind attend the process to shape the front as well? If each coastal front has its feature, then, do they have any commons? What is the reason for the Sea of Okhotsk one?'

To answer the question (3), one of clues may be found in Chapman and Lentz (1993), who studied the development of a front using an idealized simulation including a lateral buoyancy flux without wind adjustment. According to their study, the front location may be determined by buoyancy shutdown in which the offshore bottom Ekman transport becomes zero because of the thermal wind relation in the front. Farther offshore, the frontal scale is determined when the onshore buoyancy flux (or convergence of the bottom Ekman transport due to the transport retarding by the buoyancy shutdown according to the thermal wind relation) nearly balances the vertical buoyancy diffusion in the bottom boundary layer on a slope, such that

$$u\frac{\partial \rho}{\partial x} + w\frac{\partial \rho}{\partial z} = \frac{\partial}{\partial z}(\kappa_v \frac{\partial \rho}{\partial z}) \qquad (4-1)$$

where u is cross-shelf velocity, w is vertical velocity, ρ is density, κ_v is vertical eddy diffusivity, x is cross-shelf coordinate, and z is vertical coordinate. The thermodynamic relation is mainly used to depict a stable front, and the turbulence effect is parameterized by κ_v; the magnitude of κ_v determines the strength of the cross-shelf velocity u.

The relation (4-1) may explain the on-shore motion in the density front over the gently sloping shelf in Fig. 2.5. Particle should follow the density evolution equation to redistribute the density property. The relation (4-1) may be used as an approximation to the theoretical model of the case1, as we can found from the Fig. 2.5 that there are rare vertical motions inside the front while a quite large vertical diffusivity and the cross-shelf current are presented. The balance between the horizontal density advection and the

vertical density diffusion is then considered helpful for the front formation and cross-shelf overturning of the case1.

The front evolution may occur via baroclinic instability as well. If we use anomalous variables to denote the turbulence and (temporal or spatial) mean variables to denote the basic state, after the quasi-geostrophic approximation and zonal mean (or two-dimensional assumption) we can obtain a combined dynamic and thermodynamic relation to represent the front as the relation (4-2);

$$(f^2\frac{\partial^2}{\partial z^2}+N^2\frac{\partial^2}{\partial y^2})\psi^* = \underbrace{f\frac{\partial}{\partial z}(\overline{v'q'})}_{term\ Q} + f\frac{\partial \bar{F}}{\partial z}+\frac{\partial \bar{S}}{\partial y} \qquad (4-2)$$

which is known as the Transformed Eulerian Mean (Andrew & Mclntyre, 1976,1978), where ψ^* is the streamfunction representing the residual overturning circulation, f is Coriolis parameter, and N is the buoyancy frequency. The $\overline{v'q'}$ denotes the meridional eddy potential vorticity flux due to, e.g., baroclinic instability waves, $\bar{F}$ denotes forcing such as those caused by the water stress divergence $\frac{\partial \tau}{\partial z}$ (which includes the geostrophic stress), and $\bar{S}$ denotes buoyancy production such as those due to diffusion as discussed in (4-1).

The balance in (4-2) considers the impact of baroclinic instability (term Q) as well as the dynamic and thermo-dynamic impacts on the particle motion and the current pattern. These effects determine the ageostrophic overturning, and the ageostrophic overturning shapes the front. To evaluate which components balance dynamically determines the ageostrophic overturning and the further frontogenesis in the case1 is practicable, although it is also noted that (4-2) is derived based on a quasi-geostrophic approximation

and a two-dimensional assumption. Actually, not for a specific case, a more general consideration is needed to quantify the buoyancy impacts and physical dynamical impacts, and illustrate processes of frontogenesis which happens after the lateral buoyancy input.

A large vertical eddy viscosity is recognized inside the front over the gently sloping shelf of the Sea of Okhotsk, which is significant for producing a great geostrophic stress and buoyancy diffusion. Strong convection is considered contributed to a large vertical eddy viscosity. But it have not been clarified on how to generate a such large vertical viscosity with an order of hundreds of centimeter^2 per second if this magnitude is reasonable. A non-hydrostatic model would be helpful to represent the convection process and sort out if the process is conducive to the eddy generation. Then we may understand the reason of the large vertical eddy viscosity from the physical process not only from a parameterized number. One of candidates which may facilitate the convection is Ageostrophic Secondary Circulations (Thomas and Lee, 2005)).

If these extensions are realized, it would be possible to provide a full pattern of the deep mixed layer formation (from convection process, then to the frontogenesis, finally to the deep mixed layer formation) around the shelf break of the Sea of Okhotsk eventually. (a simple schematic is depicted as Fig. 4.2)

4.2 Extension of the Case2

According to the Chapter 3, the 'geostrophic stress' may be the dynamical reason of the upwelling in the upper layer of the downstream of the Alaska Coastal Current. While based on the analysis of the Climatological January mean OFES2 data, the upwelling is also strong in the lower layer which cannot be explained by the geostrophic stress dynamics.

As a future exploration, the illustration of the Figure 4.3 provides a hypothesis of the lower layer upwelling. A topography, specifically a sill, guided barotropic current is considered as the reason to induce a cyclonic gyre inside the Shelikof Strait and further contributes to a bottom upwelling. The verification with idealized simulations is in process. Another candidate to explain the lower layer upwelling is which responds to the balance between the upslope density advection and the vertical density diffusion as the relation (4-1). The verification is also ongoing.

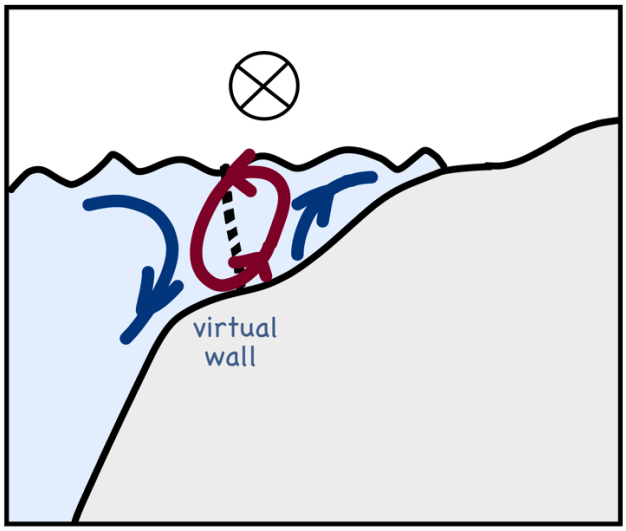

Figure 4.1 the reversed Ekman overturning performs as a 'virtual wall'

Downwelling-favorable wind responses to a 'virtual wall' acted by a front. As a result, an overturning is generated. In the onshore side of the virtual wall, the wind performs like an upwelling-favorable wind. In the offshore side of the virtual wall, the wind performs like a downwelling-favorable wind.

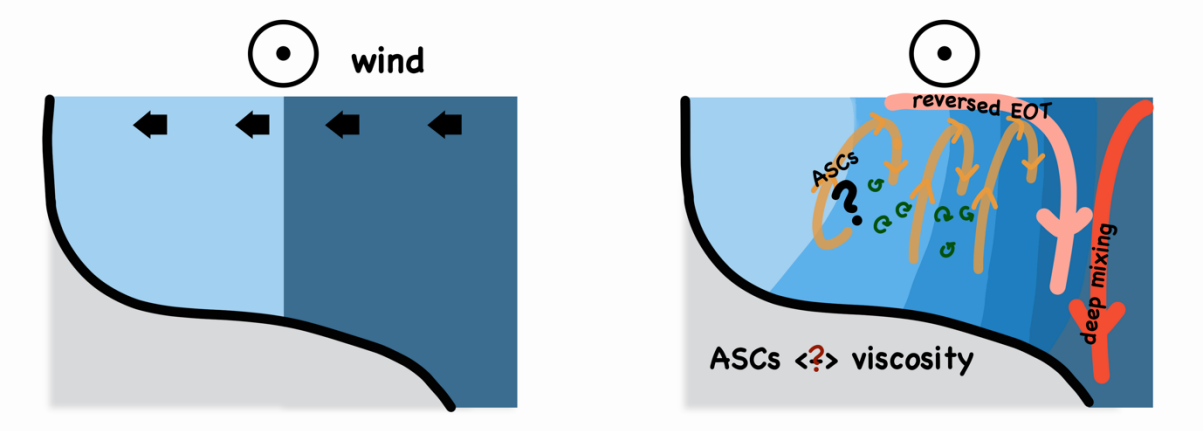

Figure 4.2 the extension of the case 1

The illustration for a frontogenesis where the geostrophic stress dominates. According to the sample studies I already elucidated the importance of the modified Ekman overturning on the coastal convection including the deep mixed layer formation and the upwelling by the water column divergence, while one necessity of the reversed EOT, frontogenesis, is still an open question. Ageostrophic secondary circulations via the downwelling-favorable wind is considered one of the possible reasons which is waiting for the further verification.

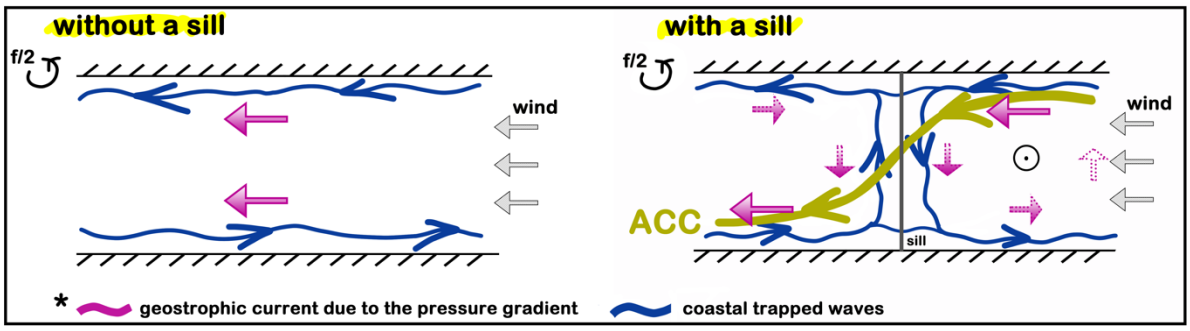

Figure 4.3 the extension of the case 2

The illustration of the upwelling formation at the bottom of the Shelikof Strait. A sill regulates barotropic current is consider the reason to generate a cyclonic gyre at the bottom of the strait, which is waiting for the future verification with the idealized simulations.

This page intentionally left blank

References

For Chapter 1

Chen, S. Y., & Chen, S. N. (2017) Generation of upwelling circulation under downwelling-favorable wind within bottom-attached, buoyant coastal currents[J]. Journal of Physical Oceanography, 47(10): 2499-2519.

Cronin, M. F., & Kessler, S. W. (2009) Near-surface shear flow in the tropical Pacific cold tongue front[J]. Journal of Physical Oceanography, 39(5): 1200-1215.

Ekman, V. W. (1905). On the influence of the earth's rotation on ocean-currents.

Fleming, Fergus (2002). Ninety Degrees North. London: Granta Publications.

Moffat, C., & Lentz, S. J. (2012) On the response of a buoyant plume to downwelling-favorable wind stress[J]. Journal of physical oceanography, 42(7): 1083-1098.

Spall, M. A., & Leif, N. T. (2016) Downfront winds over buoyant coastal plumes[J]. Journal of Physical Oceanography, 46(10): 3139-3154.

Thomas, L. N., & Lee, C. M. (2005). Intensification of ocean fronts by down-front winds. Journal of Physical Oceanography, 35(6), 1086-1102.

For Chapter 2

Allen, J. S., & Newberger, P. A. (1996) Downwelling circulation on the Oregon continental shelf. Part I: Response to idealized forcing[J]. Journal of Physical Oceanography, 26(10): 2011-2035.

Austin, J. A., & Lentz, S. J. (2002) The inner shelf response to wind-driven upwelling and downwelling[J]. Journal of Physical Oceanography, 32(7): 2171-2193.

Brink, K. H. (2016) Cross-shelf exchange[J]. Annual review of marine science, 8: 59-78.

Chen, S. Y., & Chen, S. N. (2017) Generation of upwelling circulation under downwelling-favorable wind within bottom-attached, buoyant coastal currents[J]. Journal of Physical Oceanography, 47(10): 2499-2519.

Cronin, M. F., & Kessler, S. W. (2009) Near-surface shear flow in the tropical Pacific cold tongue front[J]. Journal of Physical Oceanography, 39(5): 1200-1215.

Cronin, M. F., & Tomoki, T. (2016) Steady state ocean response to wind forcing in extratropical frontal regions[J]. Scientific reports, 6(1): 1-8.

Csanady, G. T. (1978) The arrested topographic wave[J]. Journal of Physical Oceanography, 8(1): 47-62.

Dai, A., & Trenberth, K. E. (2002) Estimates of freshwater discharge from continents: Latitudinal and seasonal variations[J]. Journal of hydrometeorology, 3(6): 660-687.

Dai, A., Qian, T., Trenberth, K. E., & Milliman, J. D. (2009). Changes in continental freshwater discharge from 1948 to 2004[J]. Journal of climate, 22(10), 2773-2792.

Dee, D. P., Uppala, S. M, Simmons, A. J., et al. (2011) The ERA-Interim reanalysis: Configuration and performance of the data assimilation system[J]. Quarterly Journal of the royal meteorological society, 137(656): 553-597.

Federiuk, J., & Allen, J. S. (1995) Upwelling circulation on the Oregon continental shelf. Part II: Simulations and comparisons with observations[J]. Journal of physical oceanography, 25(8): 1867-1889.

General Bathymetric Chart of the Oceans: https://www.gebco.net/data_and_products/gridded_bathymetry_data/

Global Ocean Physics Reanalysis: https://resources.marine.copernicus.eu/product-detail/GLOBAL_MULTIYEAR_PHY_001_030/INFORMATION

Griffies, S. M., & Hallberg, R. W. (2000). Biharmonic friction with a Smagorinsky-like viscosity for use in large-scale eddy-permitting ocean models[J]. Monthly Weather Review, 128(8), 2935-2946.

Hasumi, H. (2000) CCSR ocean component model (COCO)[J]. CCSR Rep, 13: 68.

Haversine formula: https://en.wikipedia.org/wiki/Haversine_formula

Ito, M., Ohshima, K. I., Fukamachi, Y., Mizuta, G., Kusumoto, Y., & Nishioka, J. (2017). Observations of frazil ice formation and upward sediment transport in the Sea of Okhotsk: A possible mechanism of iron supply to sea ice[J]. Journal of Geophysical Research: Oceans, 122(2), 788-802.

Kanna, N, Takenobu T, & Jun N. (2014) Iron and macro-nutrient concentrations in sea ice and their impact on the nutritional staus of surface waters in the southern Okhotsk Sea[J]. Progress in Oceanography 126: 44-57.

Kanna, N., Sibano, Y., Toyota, T., & Nishioka, J. (2018). Winter iron supply processes fueling spring phytoplankton growth in a sub-polar marginal sea, the Sea of Okhotsk: Importance of sea ice and the East Sakhalin Current[J]. Marine Chemistry, 206, 109-120.

Kondo, J., O. Kanechika, & N. Yasuda. (1978) Heat and momentum transfers under strong stability in the atmospheric surface layer[J]. Journal of Atmospheric Sciences, 35(6): 1012-1021.

Kuroda, H., Toya, Y., Watanabe, T., Nishioka, J., Hasegawa, D., Taniuchi, Y., & Kuwata, A. (2019). Influence of Coastal Oyashio water on massive spring diatom blooms in the Oyashio area of the North Pacific Ocean[J]. Progress in Oceanography, 175, 328-344.

Levitus, S. (1982) Climatological atlas of the world ocean. NOAA Prof. Paper 13. Washington, DC US Gov. Print. Off .

Lentz, S. J. (1995) Sensitivity of the inner-shelf circulation to the form of the eddy viscosity profile[J]. Journal of Physical Oceanography, 25(1): 19-28.

Lv R, Cheng P, & Gan J. (2020) Adjustment of river plume fronts during downwelling-favorable wind events[J]. Continental Shelf Research 104143.

Mamontova, N. (2021) “The ice has gone”: Vernacular meteorology, fisheries and human–ice relationships on Sakhalin Island. Polar Record 57.

Matsuda, J., Mitsudera, H., Nakamura, T., Sasajima, Y., Hasumi, H., & Wakatsuchi, M. (2015). Overturning circulation that ventilates the intermediate layer of the S ea of O khotsk and the N orth P acific: The role of salinity advection[J]. Journal of Geophysical Research: Oceans, 120(3), 1462-1489.

Mitchum, G T., & Allan. J, C. (1986) The frictional nearshore response to forcing by synoptic scale winds[J]. Journal of Physical Oceanography, 16(5): 934-946.

Mizuta, G., Fukamachi, Y., Ohshima, K. I., & Wakatsuchi, M. (2003). Structure and seasonal variability of the East Sakhalin Current[J]. Journal of Physical Oceanography, 33(11), 2430-2445.

Mizuta, G., Ohshima, K. I., Fukamachi, Y., Itoh, M., & Wakatsuchi, M. (2004). Winter mixed layer and its yearly variability under sea ice in the southwestern part of the Sea of Okhotsk[J]. Continental shelf research, 24(6), 643-657.

Moffat, C., & Lentz, S. J. (2012) On the response of a buoyant plume to downwelling-favorable wind stress[J]. Journal of physical oceanography, 42(7): 1083-1098.

Mustapha, M. A., & Saitoh, S. I. (2008) Observations of sea ice interannual variations and spring bloom occurrences at the Japanese scallop farming area in the Okhotsk Sea using satellite imageries[J]. Estuarine, Coastal and Shelf Science, 77(4): 577-588.

Nakanowatari, T, & Ohshima, K. I. (2014) Coherent Sea level variation in and around the Sea of Okhotsk[J]. Progress in Oceanography, 126: 58-70.

Nishioka J, Nakatsuka T, & Ono K, (2014) Quantitative evaluation of iron transport processes in the Sea of Okhotsk[J]. Progress in Oceanography, 126: 180-193.

Noh Y, & Jin Kim H. (1999) Simulations of temperature and turbulence structure of the oceanic boundary layer with the improved near-surface process[J]. Journal of Geophysical Research: Oceans, 104(C7): 15621-15634.

Ohshima, K. I., Simizu, D., Itoh, M., Mizuta, G., Fukamachi, Y., Riser, S. C., & Wakatsuchi, M. (2004). Sverdrup balance and the cyclonic gyre in the Sea of Okhotsk[J]. Journal of physical oceanography, 34(2), 513-525.

Ohshima, K. I, Riser, S. C., & Wakatsuchi, M. (2005) Mixed layer evolution in the Sea of Okhotsk observed with profiling floats and its relation to sea ice formation[J]. Geophysical research letters, 32(6).

Ohshima, K. I., Wakatsuchi, M., Fukamachi, Y., & Mizuta, G. (2002). Near-surface circulation and tidal currents of the Okhotsk Sea observed with satellite-tracked drifters[J]. Journal of Geophysical Research: Oceans, 107(C11), 16-1

Ohshima, K. I., Mizuta, G., Itoh, M. et al. (2001) Winter oceanographic conditions in the southwestern part of the Okhotsk Sea and their relation to sea ice[J]. Journal of oceanography, 57(4): 451-460.

Ono, J., Ohshima, K. I., Mizuta, G., Fukamachi, Y., & Wakatsuchi, M. (2006). Amplification of diurnal tides over Kashevarov Bank in the Sea of Okhotsk and its impact on water mixing and sea ice[J]. Deep Sea Research Part I: Oceanographic Research Papers, 53(3), 409-424.

Pickart, R. S. (2000) Bottom boundary layer structure and detachment in the shelf break jet of the Middle Atlantic Bight[J]. Journal of Physical Oceanography, 30(11): 2668-2686.

Product user manual from Copernicus Marine Environment Monitoring Service (CMEMS). https://catalogue.marine.copernicus.eu/documents/PUM/CMEMS-GLO-PUM-001-030.pdf

Quality Information Document from Copernicus Marine Environment Monitoring Service (CMEMS). https://catalogue.marine.copernicus.eu/documents/QUID/CMEMS-GLO-QUID-001-030.pdf

Shcherbina, A. Y., & Glen, G. G. (2008) A coastal current in winter: 2. Wind forcing and cooling of a coastal current east of Cape Cod[J]. Journal of Geophysical Research: Oceans 113.C10.

Shu, H. W., Mitsudera, H., Yamazaki, K., Nakamura, T., Kawasaki, T., Nakanowatari, T., & Sasaki, H. (2021). Tidally modified western boundary current drives interbasin exchange between the Sea of Okhotsk and the North Pacific[J]. Scientific reports, 11(1), 1-16.

Signell, R. P., Beardsley, R. C., Graber, H. C., & Capotondi, A. (1990). Effect of wave-current interaction on wind-driven circulation in narrow, shallow embayments[J]. Journal of Geophysical Research: Oceans, 95(C6), 9671-9678.

Smagorinsky, J. (1963). General circulation experiments with the primitive equations: I. The basic experiment[J]. Monthly weather review, 91(3), 99-164.

Simizu, D., & Ohshima, K. I. (2002). Barotropic response of the Sea of Okhotsk to wind forcing[J]. Journal of oceanography, 58(6), 851-860.

Spall, M. A., & Leif, N. T. (2016) Downfront winds over buoyant coastal plumes[J]. Journal of Physical Oceanography, 46(10): 3139-3154.

Stabeno, P. J., Bond, N. A., Hermann, A. J., Kachel, N. B., Mordy, C. W., & Overland, J. E. (2004). Meteorology and oceanography of the Northern Gulf of Alaska[J]. Continental Shelf Research, 24(7-8), 859-897.

Stewart, Andrew L., Andreas Klocker, & Dimitris Menemenlis. (2019) Acceleration and overturning of the Antarctic Slope Current by winds, eddies, and tides[J]. Journal of Physical Oceanography, 49(8): 2043-2074.

Suga, T., Motoki, K., Aoki, Y., & Macdonald, A. M. (2004). The North Pacific climatology of winter mixed layer and mode waters[J]. Journal of Physical Oceanography, 34(1), 3-22.

Uehara, H., Kruts, A. A., Volkov, Y. N., Nakamura, T., Ono, T., & Mitsudera, H. (2012). A new climatology of the Okhotsk Sea derived from the FERHRI database[J]. Journal of oceanography, 68(6), 869-886.

For Chapter 3

Chen, S. Y., & Chen, S. N. (2017) Generation of upwelling circulation under downwelling-favorable wind within bottom-attached, buoyant coastal currents[J]. Journal of Physical Oceanography, 47(10): 2499-2519.

Cronin, M. F., & Kessler, S. W. (2009) Near-surface shear flow in the tropical Pacific cold tongue front[J]. Journal of Physical Oceanography, 39(5): 1200-1215.

Ekman, V. W. (1905). On the influence of the earth's rotation on ocean-currents.

Fiechter, J., & Moore, A. M. (2009). Interannual spring bloom variability and Ekman pumping in the coastal Gulf of Alaska. Journal of Geophysical Research: Oceans, 114(C6).

Incze, L. S., Kendall Jr, A. W., Schumacher, J. D., & Reed, R. K. (1989). Interactions of a mesoscale patch of larval fish (Theragra chalcogramma) with the Alaska Coastal Current. Continental Shelf Research, 9(3), 269-284.

Kämpf, J., & Chapman, P. (2016). Upwelling systems of the world (pp. 31-42). Springer International Publishing Switzerland.

Ladd, C., Stabeno, P., & Cokelet, E. D. (2005). A note on cross-shelf exchange in the northern Gulf of Alaska. Deep Sea Research Part II: Topical Studies in Oceanography, 52(5-6), 667-679.

Large, W. G., & Yeager, S. G. (2004). Diurnal to decadal global forcing for ocean and sea-ice models: The data sets and flux climatologies.

Large, W., & Yeager, S. G. (2009). The global climatology of an interannually varying air–sea flux data set. Climate dynamics, 33(2), 341-364.

Loescher, K. A., Young, G. S., Colle, B. A., & Winstead, N. S. (2006). Climatology of barrier jets along the Alaskan coast. Part I: Spatial and temporal distributions. Monthly weather review, 134(2), 437-453.

Masumoto, Y., Sasaki, H., Kagimoto, T., Komori, N., Ishida, A., Sasai, Y., ... & Yamagata, T. (2004). A fifty-year eddy-resolving simulation of the world ocean: Preliminary outcomes of OFES (OGCM for the Earth Simulator). J. Earth Simulator, 1, 35-56.

Masumoto, Y. (2010). Sharing the results of a high-resolution ocean general circulation model under a multi-discipline framework—A review of OFES activities. Ocean Dynamics, 60(3), 633-652.

McDougall, T.J. and P.M. Barker (2011): Getting started with TEOS-10 and the Gibbs Seawater (GSW) Oceanographic Toolbox, 28pp., SCOR/IAPSO WG127, ISBN 978-0-646-55621-5.

Munday, D. R., & Zhai, X. (2015). Sensitivity of Southern Ocean circulation to wind stress changes: Role of relative wind stress. Ocean Modelling, 95, 15-24.

Noh Y, Kim H J. 1999. Simulations of temperature and turbulence structure of the oceanic boundary layer with the improved near-surface process. Journal of Geophysical Research: Oceans, 104: 15621-15634

Okkonen, S. R., Weingartner, T. J., Danielson, S. L., Musgrave, D. L., & Schmidt, G. M. (2003). Satellite and hydrographic observations of eddy-induced shelf-slope exchange in the northwestern Gulf of Alaska. Journal of Geophysical Research: Oceans, 108(C2).

Parish, T. R. (1982). Barrier winds along the Sierra Nevada mountains. Journal of Applied Meteorology (1962-1982), 925-930.

Pawlowicz, R. (2020). "M_Map: A mapping package for MATLAB", version 1.4m, [Computer software], available online at www.eoas.ubc.ca/~rich/map.html

Reed, R. K. (1984). Flow of the Alaskan Stream and its variations. Deep Sea Research Part A. Oceanographic Research Papers, 31(4), 369-386.

Royer, T. C. (1979). On the effect of precipitation and runoff on coastal circulation in the Gulf of Alaska. Journal of Physical Oceanography, 9(3), 555-563.

Sasaki, H., Kida, S., Furue, R., Aiki, H., Komori, N., Masumoto, Y., ... & Taguchi, B. (2020). A global eddying hindcast ocean simulation with OFES2. Geoscientific model development, 13(7), 3319-3336.

Sasaki, H., Qiu, B., Klein, P., Nonaka, M., & Sasai, Y. (2022). Interannual Variations of Submesoscale Circulations in the Subtropical Northeastern Pacific. Geophysical Research Letters, 49(7), e2021GL097664.

Schumacher, J. D., & Reed, R. K. (1980). Coastal flow in the northwest Gulf of Alaska: the Kenai Current. Journal of Geophysical Research: Oceans, 85(C11), 6680-6688.

Spitz, Y. H., & Nof, D. (1991). Separation of boundary currents due to bottom topography. Deep Sea Research Part A. Oceanographic Research Papers, 38(1), 1-20.

St. Laurent, L. C., Simmons, H. L., & Jayne, S. R. (2002). Estimating tidally driven mixing in the deep ocean. Geophysical research letters, 29(23), 21-1.

Stabeno, P. J., & Reed, R. K. (1991). Recent lagrangian measurements along the Alaskan Stream. Deep Sea Research Part A. Oceanographic Research Papers, 38(3), 289-296.

Stabeno, P. J., Reed, R. K., & Schumacher, J. D. (1995). The Alaska Coastal Current: continuity of transport and forcing. Journal of Geophysical Research: Oceans, 100(C2), 2477-2485.

Stabeno, P. J., & Hermann, A. J. (1996). An eddy-resolving model of circulation on the western Gulf of Alaska shelf: 2. Comparison of results to oceanographic observations. Journal of Geophysical Research: Oceans, 101(C1), 1151-1161.

Stabeno, P. J., Bond, N. A., Hermann, A. J., Kachel, N. B., Mordy, C. W., & Overland, J. E. (2004). Meteorology and oceanography of the Northern Gulf of Alaska. Continental Shelf Research, 24(7-8), 859-897.

Stabeno, P. J., Bell, S., Cheng, W., Danielson, S., Kachel, N. B., & Mordy, C. W. (2016). Long-term observations of Alaska Coastal Current in the northern Gulf of Alaska. Deep Sea Research Part II: Topical Studies in Oceanography, 132, 24-40.

Tsujino, H., Urakawa, S., Nakano, H., Small, R. J., Kim, W. M., Yeager, S. G., ... & Yamazaki, D. (2018). JRA-55 based surface dataset for driving ocean–sea-ice models (JRA55-do). Ocean Modelling, 130, 79-139.

Ware, D. M., & Thomson, R. E. (2005). Bottom-up ecosystem trophic dynamics determine fish production in the Northeast Pacific. science, 308(5726), 1280-1284.

Weingartner, T. J., Danielson, S. L., & Royer, T. C. (2005). Freshwater variability and predictability in the Alaska Coastal Current. Deep Sea Research Part II: Topical Studies in Oceanography, 52(1-2), 169-191.

Yuan, N., & Mitsudera, H. (2022). Cross-shelf overturning in geostrophic-stress-dominant coastal fronts. Journal of Oceanography, 1-22.

Zimmermann, M., Prescott, M. M., & Haeussler, P. J. (2019). Bathymetry and geomorphology of Shelikof Strait and the Western Gulf of Alaska. Geosciences, 9(10), 409.

For Chapter 4

Andrews, D. G., & Mcintyre, M. E. (1976). Planetary waves in horizontal and vertical shear: The generalized Eliassen-Palm relation and the mean zonal acceleration. Journal of the Atmospheric Sciences, 33(11), 2031-2048.

Andrews, D. G., & McIntyre, M. E. (1978). Generalized Eliassen-Palm and Charney-Drazin theorems for waves on axismmetric mean flows in compressible atmospheres. Journal of Atmospheric Sciences, 35(2), 175-185.

Chapman, D. C., & Lentz, S. J. (1994). Trapping of a coastal density front by the bottom boundary layer. Journal of Physical Oceanography, 24(7), 1464-1479.

Mizuta, G., Ohshima, K. I., Fukamachi, Y., Itoh, M., & Wakatsuchi, M. (2004). Winter mixed layer and its yearly variability under sea ice in the southwestern part of the Sea of Okhotsk[J]. Continental shelf research, 24(6), 643-657.

Ohshima, K. I, Riser, S. C., & Wakatsuchi, M. (2005) Mixed layer evolution in the Sea of Okhotsk observed with profiling floats and its relation to sea ice formation[J]. Geophysical research letters, 32(6).

Ohshima, K. I., Mizuta, G., Itoh, M. et al. (2001) Winter oceanographic conditions in the southwestern part of the Okhotsk Sea and their relation to sea ice[J]. Journal of oceanography, 57(4): 451-460.

Thomas, L. N., & Lee, C. M. (2005). Intensification of ocean fronts by down-front winds. Journal of Physical Oceanography, 35(6), 1086-1102.

This page intentionally left blank

Acknowledgements

The author would like to thank the Prof. Mitsudera, for giving her a chance to immerse in the coastal dynamic research during these four years, to work together with and to learn from him. Prof. Mitsudera is an intellectual and respectable researcher. The way he comprehends the oceanic dynamic is instructive for the author and enlightens the author's understanding on a picturesque oceanic dynamic world.

The author also would like to give credits on the book 'Geophysical Fluid Dynamics' reading held with Prof. Mitsudera, Dr. Hungwei Shu, and Dr. Yamazaki, the lecture from Prof. Kubokawa, and the mail exchange with Prof. Yoshikawa. They showed author the beauty of fluid dynamic with a deep thinking.

The author thanks Dr. Nakamura, Dr. Furue, Dr. Kida and Dr. Sasaki for their constructive discussions and comments on coastal dynamics, greatly appreciate Dr. Nishioka for his discussions on material circulations and Dr. Nakanowatari for his instruction on the initial model configuration.

The author would like to personally thank the selfless supporting from her family, and thank Dr. Hungwei Shu, Dr. Saiki, Dr. Na Li, Ms. Shinohara, Ms. Murayama and all of colleagues in the ILTS Mitsudera-Lab and in the Pan-Okhotsk Research Center for their sincere care on the author's normal daily life and made it more colorful and enjoyable.

The study was supported by the Special Grant Program for international students, Graduate School of Environmental Science, Hokkaido University, Japan, KAKENHI (17H01156, 19H05701, 21H01154, 21H05056) and the Environment Research and Technology Development Fund (JPMEERF20214002).

The author would like to bring these treasure troves to her next station, and the author wishes the pleasure she gained from the grove of natural science these years can always with her.